DISSERTATION

IMPROVEMENT OF OXIDE CERAMIC MATERIALS VIA CATION SUBSTITUTION FOR THERMIONIC EMISSION APPLICATIONS: CONNECTING CATION CHARACTERISTICS TO CHANGES IN ATOMISTIC STRUCTURE AND PROPERTIES

Submitted by

Liam Eugene Fisher

Department of Mechanical Engineering

In partial fulfillment of the requirements

For the Degree of Doctor of Philosophy

Colorado State University

Fort Collins, Colorado

Spring 2025

Doctoral Committee:

Advisor: Kaka Ma

Chris Weinberger
Jamie Neilson
Todd Bandhauer

ABSTRACT

IMPROVEMENT OF OXIDE CERAMIC MATERIALS VIA CATION SUBSTITUTION FOR THERMIONIC EMISSION APPLICATIONS: CONNECTING CATION CHARACTERISTICS TO CHANGES IN ATOMISTIC STRUCTURE AND PROPERTIES

My research aimed to improve oxide ceramic materials for thermionic emission applications through strategic cation substitution, focusing on enhancing material properties like thermal stability and electrical conductivity. In thermionic emission applications, low work functions and high thermal resilience are essential material properties for efficient electron emission under high temperatures. Two oxide-based material systems, mayenite electride and strontium vanadate, were selected in the present work, because of their promising low work function, reasonable thermal stability, and economical costs of precursors. But both materials require improvements to realize or increase their applicability in thermionic emission technologies. Moreover, these two material systems possess distinguishing lattice structures from each other and utilize different mechanisms for low work function. Thus, in-parallel investigation into and comparison of the results from these two types of oxide ceramics provide fundamental insights into the interplay between the atomistic structure and cationic substitution.

A critical objective of this research is to discover how various cation substitutions affect the lattice structure and how these structural changes subsequently modify key material properties for the thermionic emission application. Different cations were substituted at select sites in mayenite electride and strontium vanadate structures, individually and in dual

combinations, to assess their effects on thermal stability and electrical conductivity. The hypothesis was that substituting smaller cations at particular atomic sites might increase thermal stability by altering the lattice parameters, bonding environment, and electron density. The study also investigated how dual substitutions might synergize beneficial effects from individual cations, with a focus on combinations that can potentially balance thermal stability and electrical conductivity.

To characterize structural modifications, this research employs Rietveld refinement of X-ray diffraction data to conduct detailed analysis of lattice parameter adjustments and cation disorder, providing insight into the structural intricacies induced by specific substitutions. Additionally, thermogravimetric and electrical conductivity analyses reveal trends in the change of oxidation resistance and conductivity that align with anticipated impacts of certain cations. Results suggest that substituting smaller cations into mayenite lattice significantly increases oxidation onset temperature. In strontium vanadate, substitutions at the A- and B-sites have limits to stability as the material drifts further from the ideal tolerance factor of one, with critical implications for phase stability and oxidation behavior. The calcium substitute for strontium led to a vast improvement in both thermal stability (onset of rapid oxidation increased to a temperature > 1050°C) and electrical conductivity (σ > 3000S/cm). The key findings from this work demonstrate that tailored cation substitutions can substantially improve the key properties of oxide ceramics, offering pathways for material optimization for thermionic applications in harsh environments.

ACKNOWLEDGEMENTS

The list of people and institutions who supported me on this journey could fill an entire chapter, but I'll strive to keep it brief. First, I extend my gratitude to Colorado State University for their support, including funding for my advisor's lab and providing me with teaching opportunities that helped sustain my academic endeavors. I am also deeply thankful to Lockheed Martin for their financial support during my Ph.D., and to Dr. Tom McGuire, the project manager, for offering invaluable technical expertise as I began steering this research in new directions.

I owe an immeasurable debt of gratitude to my advisor, Dr. Kaka Ma. Her unwavering belief in me, even during my moments of struggle, instilled the confidence I needed to persevere and complete this degree. Her profound knowledge and guidance have not only shaped me into a better scientist but have also enriched me as a person.

I would also like to thank my committee members, Dr. Chris Weinberger, Dr. Todd Bandhauer, and Dr. Jamie Neilson, for their support, insightful questions, and constructive feedback. Their time spent reviewing my work and offering advice has significantly enhanced my research and contributed to my professional growth. I am particularly grateful to Dr. Weinberger, whose instruction in a wide array of graduate courses greatly expanded my understanding and deepened my passion for materials science and engineering.

I am equally indebted to the faculty and students who have supported me along the way. To my lab mates—Alex Preston, Alex Sutherland, Janelle Hobbs, Yuchen Lin, Brody DeBoer,

and Adam Khuester—thank you for everything, from lab training to deep friendships. I am especially grateful to Dr. Ben Grier for his mentorship in teaching and personal development, and to Dr. Donald Radford and Jaren Fleischman for maintaining the Factory facilities and assisting me whenever equipment malfunctions arose. Additionally, I extend my appreciation to the Analytical Resources Core at CSU (RRID:SCR_021758) and, in particular, Dr. Brian Newell, for their support in materials characterization throughout my Ph.D.

Finally, I must thank my parents, brother, and friends. Your unwavering love and encouragement over the past five and a half years have been my anchor, driving me forward. I would not be here today without your constant support.

DEDICATION

To my family and friends, whose belief in me fueled this research from start to finish.

TABLE OF CONTENTS

LIST OF TABLES

LIST OF FIGURES

Chapter 1 Literature Review and Research Objectives

1.1 Introduction

Thermionic emission has increasingly gained interest within the scientific community as new technologies are developed to harness its power. In order to fully enable these new technologies, there is a need for more robust materials with low work function. There are several materials in current use which have different drawbacks in the form of either limitations to material properties or prohibitive cost. However, there are two materials which are drawing increased interest as promising candidates for the application of thermionic emission: mayenite electride and strontium vanadate. This chapter serves as a review of the concept of thermionic emission as well as these two material systems and the recent work in attempting to bolster their material properties. The review informs the motivation for this work as well as the specific goals of this research which are set forth after the review. All of these components contribute to the overall focus of the research which is developing greater understanding of two prominent candidate materials for thermionic emission.

1.2 Thermionic Emission

The working principle of thermionic emission is illustrated in Figure 1.01 below. Energy input excites an electron from the material surface to the vacuum to create an emission current, and this is governed by the property known as the work function.

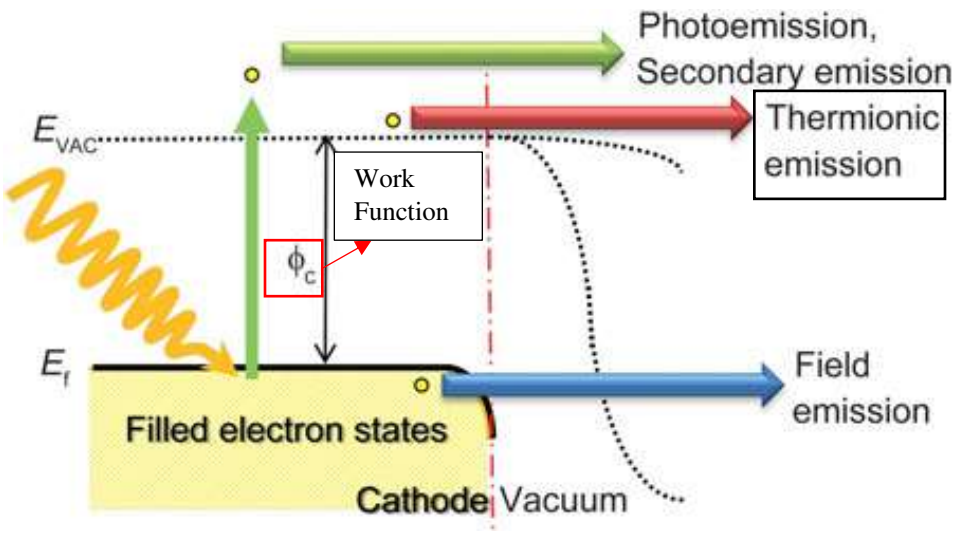

Figure 1.01 Schematic of thermionic emission [1]

The work function of a material is the minimum energy that is required to excite an electron from the Fermi level to vacuum. This can be understood through the photoelectric effect in which incident light strikes a material surface and an electron is emitted with equal kinetic energy which yields the equation for work function

$$\Phi = hv_0 \qquad \text{EQ(1)}$$

where Φ is the work function, h is Planck's constant, and v_0 is the light frequency. Thermionic emission utilizes a similar mechanism but excites electron emission through the application of thermal energy to the material. Continuous application of heat leads to an emission current which is defined by the Richardson-Laue-Dushman equation

$$J = AA_0{T_e}^2 \exp\left(-\frac{\phi}{k_B T_e}\right) \exp\left(\frac{\Delta W}{k_B T_e}\right) \qquad \text{EQ(2)}$$

where J is the emission current density, A_0 is the Richardson constant for metals $\left(120.2 \frac{A}{cm^2 K}\right)$, A is an adjustment factor for the specific emission material, T_e is the material temperature, k_B is Boltzmann's constant, and $\exp\left(\frac{\Delta W}{k_B T_e}\right)$ represents the field (Schottky) effect [2]. Based on EQ(2),

it is apparent that a lower work function is desirable to achieve higher emission currents for a given temperature.

The thermionic emission principle has enabled several technologies and applications in the engineering world. Thermionic energy conversion devices were proposed as early 1915 by Schlicter [3], but substantial power generation (150W) from this technology was not realized until the 1950s [4]. Many high- resolution analytic instruments, such as electron microscopes, rely on an ion beam provided by thermionic emitters. Satellite propulsion technologies such as ion thrusters, Hall thrusters, and magnetoplasmadynamic thrusters rely on hollow cathodes to ionize propellant gases and the inserts for these cathodes are made of thermionic emission materials. My interest in the thermionic emission field was invoked through research funded by Lockheed Martin to develop thermionic emission materials for effectively cooling leading edges of hypersonic vehicles via a mechanism named electron transpiration cooling (ETC) [5], [6], [7]. ETC, or thermionic cooling, is a novel concept yet to be fully realized, which requires well designed thermionic emission materials with low work function in order to achieve cooling on par with mechanisms like radiative cooling. As seen in Figure 1.02, a material with high work function (4eV) would need to operate at close to 3000K to compete with radiation compared to 1300K for a low work function material (2eV).

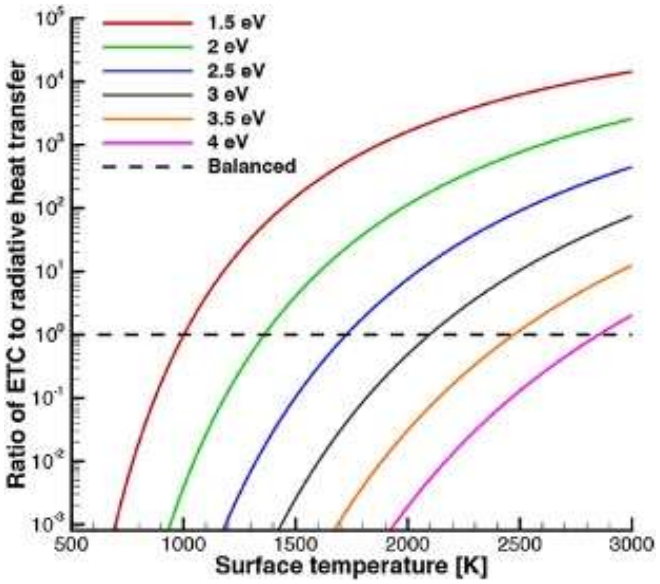

Figure 1.02 ETC versus radiative cooling for different work functions [7]

Several materials are already utilized for thermionic emission purposes such as tungsten. While W has a relatively high work function (4eV) its high melting temperature means a huge amount of thermal energy can be applied to yield high emission currents. The work function of tungsten has also been lowered to 2.1eV with the inclusion of a surface layer of barium oxide, but this layer is susceptible to oxidation as well as melting at high temperatures [8], [9]. In addition, some boride materials, such as LaB_6 (2.7eV) and CeB_6 (2.5eV), have performed well in this capacity but they are much more expensive to extract and still have issues with oxidation [9]. All these materials still face challenges for thermionic emission applications. Space charging near the surface of emitting materials remains an issue as the emitting electrons begin to build their own barrier once emission begins. Machinability of low work function ceramics such as the previously mentioned borides is quite difficult. In addition, a primary challenge facing the field of thermionic emission devices is the development of low-cost materials with stable properties that would not radically degrade by operation at high temperature nor short lived due to issues with oxidation.

Compared to the aforementioned materials, mayenite electride is attractive in that it is made of low-cost constituents, has a relatively high melting temperature (1400°C), and an extremely low work function (≤2.4eV) [10], [11], [12], [13], [14]. Soon after the first synthesis of C12A7:e^-, Toda et al. examined its capabilities as an electron emitter by studying I-V characteristics of Ca vapor reduced electride during field emission spectroscopy. They observed field effects at room temperature using high acceleration voltages (>1600V) and emission current was collected reaching a maximum of 22μA/cm^2 [10]. The relationship between current and accelerating voltage was consistent with the Fowler-Nordheim (F-N) model as seen in Figure 1.03b

$$I = \frac{\alpha(BV^2)}{A\Phi}\exp\left(-\frac{\beta\Phi^{\frac{3}{2}}}{BV}\right) \qquad \text{EQ(3)}$$

where $\alpha = 1.514 * \frac{10^{-6}AeV}{V^2}$, $\beta = 6.831 * \frac{10^{-7}V}{eV^{\frac{3}{2}}cm}$, A is the emission surface area, and B is a structure factor dependent on surface roughness. The work function was determined to be 0.3eV based on EQ(3), assuming that the surface was ideally flat and $B = \frac{1}{d}$ where d is the distance between the cathode and anode [10]. Toda et al. also probed thermionic emission by increasing the temperature up to 513K and observed that thermionic emission dominated the field effects at low accelerating voltages as seen on the inset of Figure 1.03a. This emission current density followed the Richardson-Dushman model and revealed that the work function is 0.6eV. This value, when viewed through the lens of the F-N model, showed that, rather than being ideally flat, the surface had a roughness of radius 7.5μm which was reasonable given the small grain size of the polishing media (1μm). The discrepancy between the two work function values demonstrates the concentrated electric field occurring near the sample surface as the result of increased emission. Work function was also measured by ultraviolet photoelectron spectroscopy

(UPS), however, the value obtained from this method was much higher (3.7eV) compared to that observed from emission testing [10]. This is explained by changes to the surface electronic structure under the influence of the applied electric field. Specifically, the unavoidable partial oxidation of the surface layer of C12A7:e^- would lead to a surface band bending effect during the field emission spectroscopy.

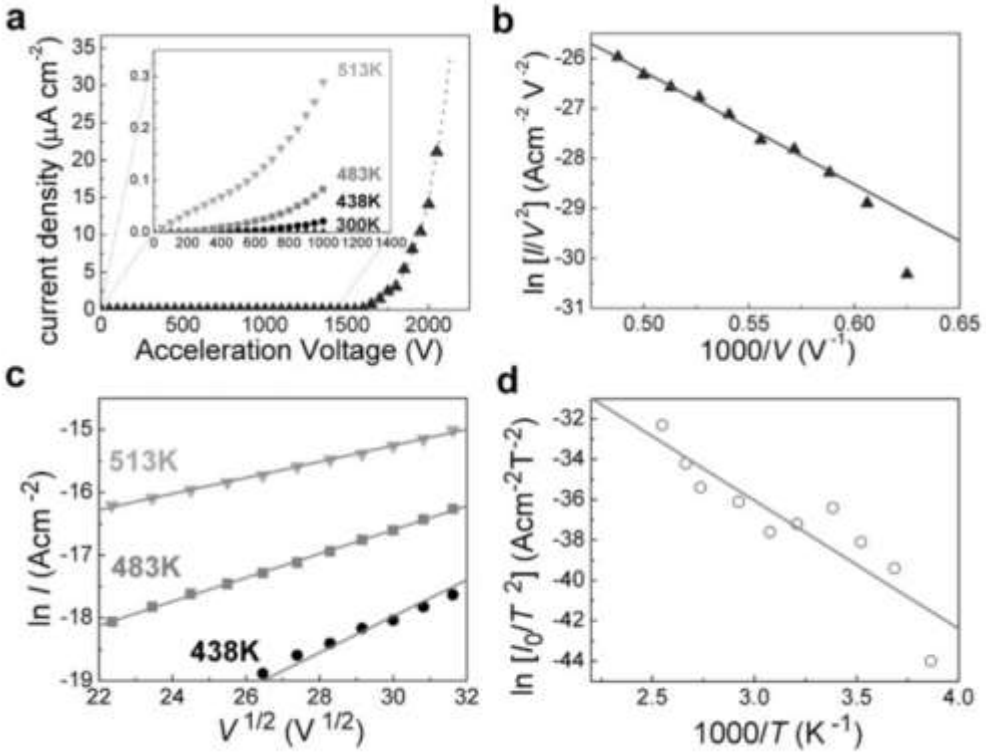

Figure 1.03 Field emission spectroscopy of mayenite electride (a) Electron emission I-V characteristics (b) Fowler-Nordheim plot at room temperature (c) ln I-$V^{1/2}$ at 438K, 483K, and 513K (d) Temperature dependence of the prefactor I_0 for thermionic emission [10]

Subsequently, Toda et al. studied two samples more rapidly prepared using titanium vapor reduction. Sample A exhibited high conductivity (1500S/cm) and electron concentration ($2*10^{21}cm^{-3}$) compared to Sample B which had values of 0.1S/cm and 10^{-19} cm^{-3} respectively. The group employed further spectroscopy techniques including hard X-ray photoelectron spectroscopy (HAXPES), inverse photoelectron spectroscopy (IPES), and photoelectron yield spectroscopy (PSY) to characterize the electronic structure more rigorously. Using the PSY

measurements at increasing bias voltages, a work function of 2.4eV was calculated with the relation to photoelectron current

$$\ln(I_{PE}T^{-2}) = \ln\left(F\frac{(h\nu-\Phi)}{kT}\right) + Z \qquad \text{EQ(4)}$$

where $F(x) = \int_0^\infty \frac{y}{1+\exp(y-x)}dy$ and Z is constant [11]. As seen in Figure 1.04b the line of best fit for EQ(4) for data sets from both samples settle on this intrinsic value independent of the bias voltage. Work function results from UPS data on the other hand showed a great dependence on both the bias voltage and the energy level of the UV source (He lamp). Specifically observed was a changing energy of the vacuum which increased with increasing bias voltage. This can be ascribed to band bending near the surface, as the effect was more pronounced for the more insulative electride sample. In order to find an intrinsic value, the UPS data was extrapolated to zero bias voltage and zero I_{PE} which then confirmed the PSY results.

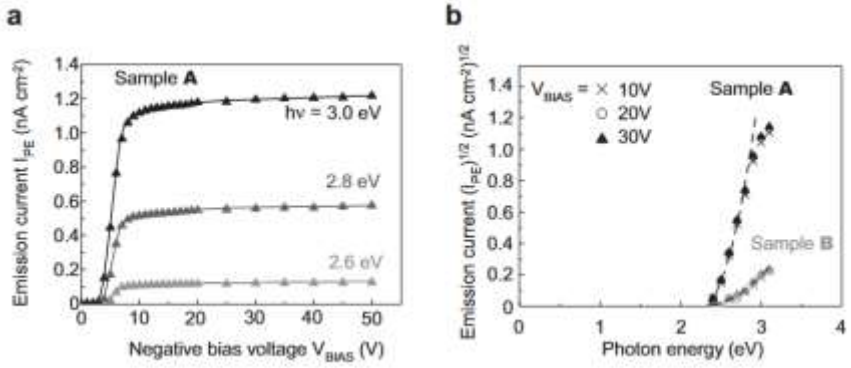

Figure 1.04 (a) Photoemission current as a function of V_{BIAS} of sample A for excited photon energies of 2.6eV, 2.8eV, and 3.0 eV (b) $IPE^{1/2}$ – hν plots for samples A and B. The dashed lines are best-fit curves to EQ(4) [11]

1.3 Mayenite Electride

Mayenite is a secondary phase in the CaO-Al_2O_3 system shown on the phase diagram below in Figure 1.05. It is composed of calcium oxide and alumina mixed in a ratio of 12:7 (C12A7) with stoichiometry $Ca_{12}Al_{14}O_{33}$. As seen in the phase diagram in Figure 1.05 slight

deviations from the stoichiometric ratio often leads to other insulative cement phases such as calcium rich C3A or alumina rich CA so precise processing is desired. The unit cell has a cubic structure made of a positively charged framework consisting of twelve cages as seen in Figure 1.06. Each cage is connected to eight neighboring cages via “windows,” or rings structured as Ca-O-Al-O-Al-O, which allow for mass transport.

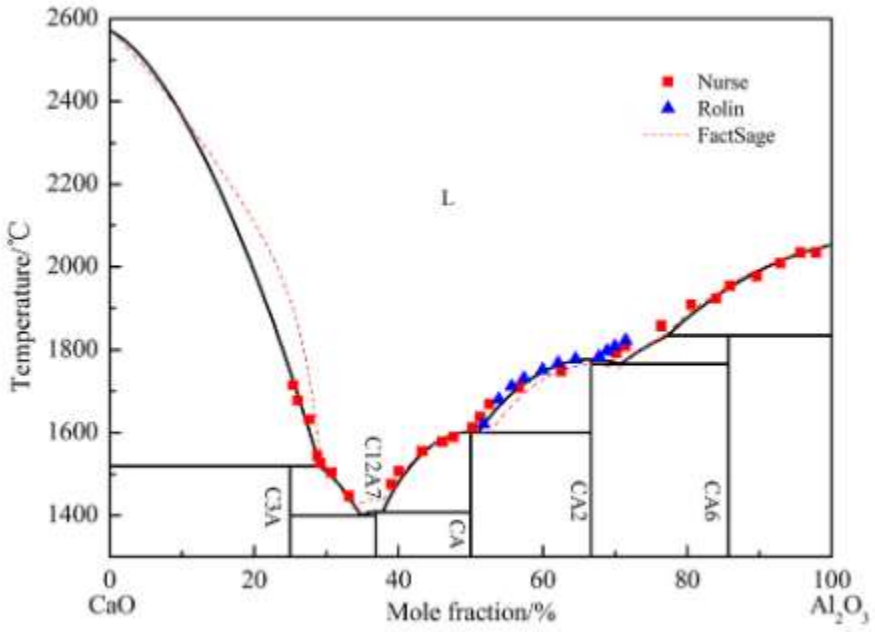

Figure 1.05 CaO-Al_2O_3 Phase Diagram [15]

The 4+ charge on the framework is neutralized by two oxygen anions which are randomly distributed into two of the cages and thus the compound is often written as $[Ca_{24}Al_{28}O_{64}]^{4+}(O^{2-})_2$. These oxygen anions are loosely bound by the six calcium ions in each cage but are considered “free” because the cage is greater than 50% larger than the diameter of the oxygen [12], [16].

Single crystal growth of mayenite has been achieved in a variety of methods. Traditional floating zone or Czochralski growth has been employed with a consistent issue of oxygen bubbles which were eventually overcome with higher melt temperatures allowing the bubbles to move out of the crystal [13]. Single crystals have also been processed using chemical methods

such as sol-gel and hydrothermal synthesis, but like FZ and CZ they take a relatively long time [13], [17], [18], [19]. The most expedient method for mayenite synthesis is making polycrystalline material using a standard powder solid state reaction which is on a time scale of hours compared to days.

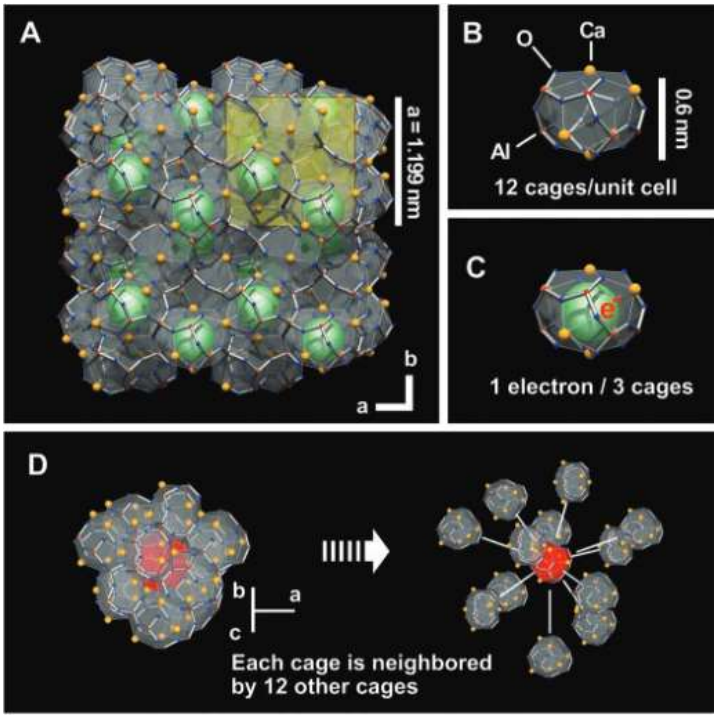

Figure 1.06 Cage structure of mayenite electride [12]

It had previously been observed that the free oxygen anion could be replaced by other monovalent ions such as hydroxide ions (OH^-) or halogen anions (F^-, Cl^-) and theoretical work on the advantage of using electrons as anions had been proposed by Dye in the 1990s [20]. Replacement of the free oxygen with an electron to synthesize the electride form of this material was first demonstrated by Hosono et al. when they replaced the free oxygen anions with hydride (H^-) ions and then subsequently irradiated the material with ultraviolet light [21]. The electrons were emitted from the encaged hydrogens and subsequently moved to an empty cage while the deionized hydrogens recombined to form H_2 molecules in a cage. This process led to a low

conductivity (0.3S/cm) high transparency (<1% transmission loss of visible light) mayenite electride. Reduction of insulative mayenite into its electride form progressed from this initial breakthrough through the use of calcium metal vapor as a reducing agent as seen in Figure 1.07. However, this led to the formation of a CaO layer which impeded the diffusion of the free oxygen ions out of the cages thus requiring extremely long heat treatments (>240hrs) in order to produce high electron density electride [12], [13], [22]. More recently titanium metal has been adopted as the main reducing agent as it instead forms non-stoichiometric oxides that improve diffusion. This improvement to processing has been accompanied by improvements to the electronic properties of the material as conduction has soared as high as 1500S/cm and electron density has approached the theoretical maximum ($2.33*10^{21}cm^{-3}$) for single crystals [12], [13], [14]. The reduction is accompanied by a color change from white (insulative mayenite) to green (partially reduced) to black (complete reduction) as seen in the image below. This technique has been deployed using spark plasma sintering (SPS) in order to rapidly synthesize mayenite electride. The SPS environment offers the advantage of a carbothermal reducing environment due to the graphite tooling, and the high heating rates allow for rapid sintering of bulk mayenite electride [23].

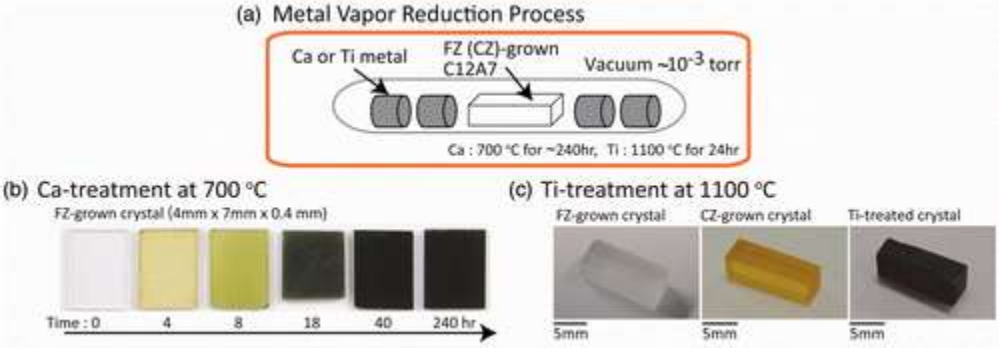

Figure 1.07 Metal vapor reduction of C12A7 to electride form [13]

In addition to improved synthesis of pure electride there has been work in both alloying and cation substitution in the mayenite electride system to improve the thermionic emission capabilities. Yoshizumi et al. prepared a 70:30 mayenite electride:titanium composite after reducing mayenite with titanium vapor treatment over the course of two weeks. The resulting composite was machined into a sharp tip (140μm radius) and inserted into the emission cathode as seen in Figure 1.08.

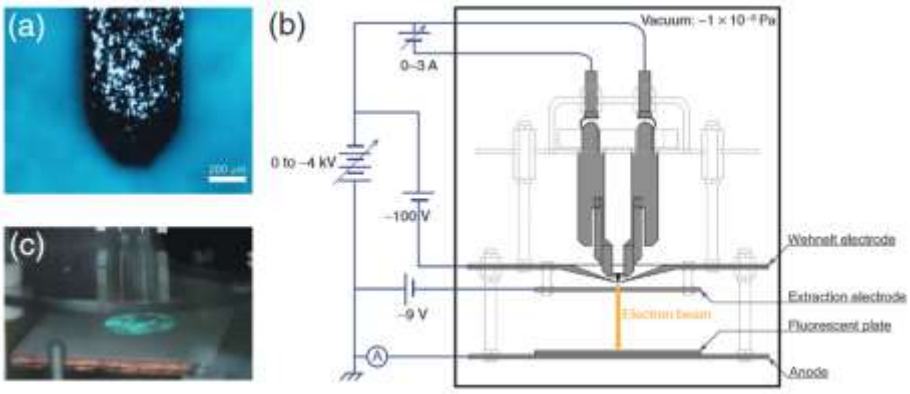

Figure 1.08 Thermionic emission of C12A7:e^--Ti composite (a) Machined sample (b) Cathode schematic (c) Fluorescence from beam irradiation [24]

Measuring emission current over several temperatures and varying accelerating voltages up to 40,000 V/cm the composite preformed well reaching a peak current current density of 1.4mA/cm^2 at 700℃ [24]. At lower applied fields there is a space charge effect as the electrons emit from the surface and create their own electric field which limits the emission current as seen in Figure 1.09. The data gathered over the range from 600-700℃ allows for the calculation of work function by using the thermionic emission model including the Schottky effect as seen below

$$J = J_0 \exp\left(\frac{e}{kT}\sqrt{\frac{eF}{4\pi\varepsilon_0}}\right) \qquad \text{EQ(5)}$$

where J_0 is the zero field current density, F is the field, and ε_0 is the vacuum dielectric constant. The linear regions of the emission current data collected (Figure 1.09) are extrapolated to $F = 0$ in order to get the zero field current density, and then these are plotted against temperature to get work function from EQ(2). Meanwhile, cation substitution improved thermionic emission was demonstrated by Zhang et al. when they synthesized single crystal Sr-substituted mayenite electride in a FZ method. The substituted electride lowered the work function to 1.80eV from 1.89eV and achieved an emission current of 1.87A/cm^2 which was a 50% increase from their single crystal pure electride [25].

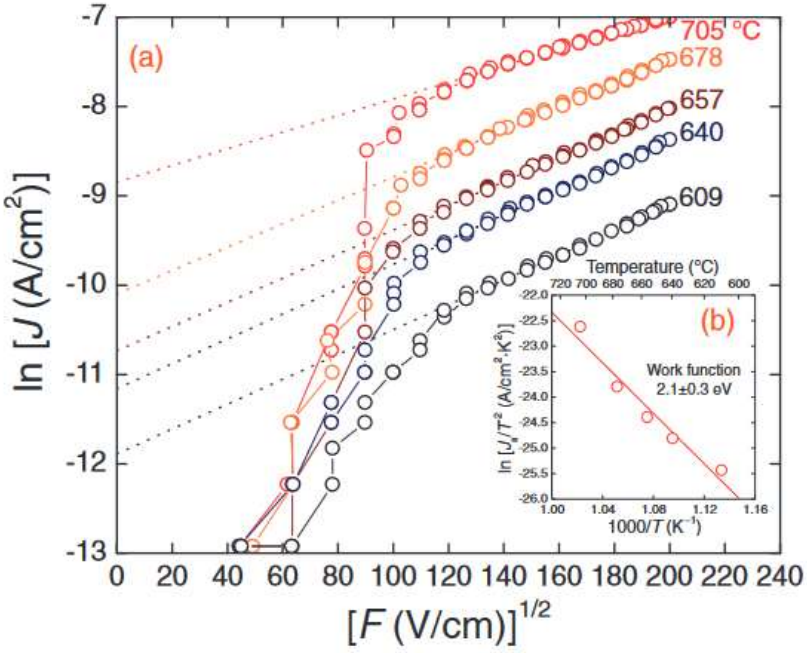

Figure 1.09 Thermionic emission of C12A7:e$^-$-Ti composite. Inset is Richardson-Dushman plot [24]

Obviously, mayenite electride shows promise as a thermionic emitter, however, the origins of such properties are still being discovered. Sushko et al. used an embedded cluster model to calculate the band structure of insulative and reduced mayenite and explain the change in electronic structure and absorption behavior. The insulative mayenite has a wide band gap (7eV) which is split by a cage conduction band (CCB) that sits 5.4eV above the valence band

(VB) and 2eV below the framework conduction band (FCB). This CCB arises from the empty cages and the connection of the s-like ground states of the framework cations which is contrasted to the free oxygen occupied cages which have no CCB and for which the O^{2-} radicals' 2p energy sits 2eV above the VB. When the electron then fills an empty cage the CCB minimum is lowered by 1eV as the cage is relaxed inward and electron is thus localized similar to F-centers and F^+-centers which is why they are referred to as "F^+-like centers" [26]. Toda et al. compared the energy structure of an F^+ center in CaO to the CCB of mayenite electride which arises from the encaged electron which is octahedrally coordinated with 6 Ca^{2+}atoms (Figure 1.10). The difference between these is that the encaged electron has much more separation from the Ca atoms compared to the F^+ center and the charge compensation from the Al^{3+} atoms which combined result in a much lower Madelung potential leaving the cage conduction band much closer to the vacuum as seen in the representative band structure image in Figure 1.10 [11]. However, this inward relaxation of a single cage does not propagate over the network of cages as further replacements are induced and in fact expansion of the lattice for high electron substituted mayenite is further reflected by X-ray diffraction (XRD) data which shows a slight shift to the left from insulative mayenite indicating a decrease in the lattice parameter from 11.99Å to 12.01Å. While the electron density remains relatively low ($N_e<10^{21}cm^{-3}$) these F^+-like centers can hop between cages under the influence of an electric field to induce current flow [12]. Beyond this concentration the electrons become delocalized and behave like a metal.

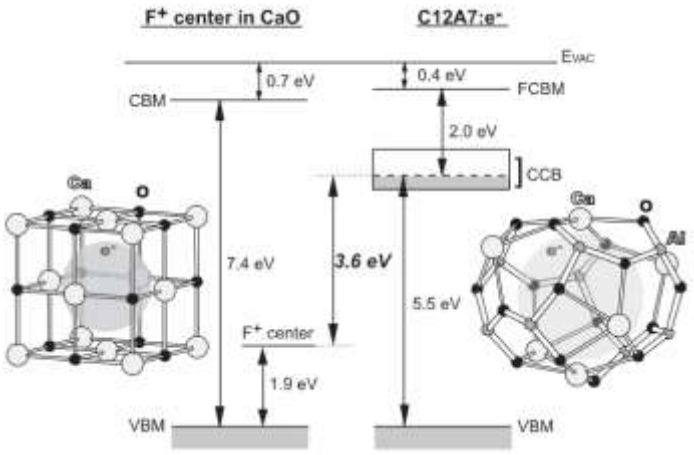

Figure 1.10 Band structure of mayenite electride cage compared to F+ center in CaO [11]

Mayenite electride has many desirable properties which lend the material to many different engineering applications, but there remains room for improvement which has yet to be fully realized. For decades there has been work done in introducing impurities into semiconductors to alter the electronic structure and the same type of work has started to gain traction in regard to mayenite electride. As early as 1990, work had begun to make cation substitutions in insulative mayenite to increase its conductivity for use as a solid electrolyte [27]. In the early 21st century further work on insulative mayenite was conducted with several cation substitutes including Mg [28], Si [29], Ga [30] and Fe [31]. The results of these experimental works were not homogenous over the span of different cation substitutes or even the dosage profiles which they investigated. Magnesium substituted mayenite showed a decreased ionic conductivity whereas the silicon substituted counterpart instead showed an increase from 0.15 to 0.61S/cm for $Ca_{12}Al_{10}Si_4O_{35}$ [28], [29]. The Si^{4+}substitutions for the Al^{3+} atoms help to accommodate extra free oxygens which allows for more release of electrons upon irradiation with hydrogen. This compound was less thermally stable than pure mayenite as it began to decompose at a low temperature of 600℃. According to Palacios et al., the mayenite structure

was much less accommodating to larger gallium ions when substituted for aluminum as it was observed any replacement level higher than a single atom resulted in decomposition of pure C12A7 into other secondary phases including $Ca_5Ga_6O_{14}$. For the successful gallium substituted sample $Ca_{12}Al_{13}GaO_{33}$ there was a marked expansion of the lattice as indicated by the growth of the parameter from $a = 11.98681Å$ to $a = 11.99734Å$ [30]. There were also attempts to reduce the gallium substituted samples by both carbothermal reduction as well as a metal vapor treatment (vanadium foil) both resulting in materials with a partial grey coloration. The former reduction route resulted in a partial decomposition of mayenite and a reduction in the lattice size which is the opposite effect observed when the electrons replace the free oxygens in large quantity. Moreover, the Rietveld analysis of the XRD data showed that the gallium occupation factor had converged to zero most likely due to the gallium's reduction to a metal state [30]. Fe-substitution was investigated by Ebbinghaus et al. at a level of 1mol% $Ca_{12}Al_{13.86}Fe_{0.14}O_{33}$ for its capacity to improve ionic conductivity by reducing the presence of hydroxyl groups in the cages as well as acting as a reducing agent to possibly incorporate electrons into the cages [31]. The iron substitution resulted in a small 0.17% increase to the lattice size which is expected given that iron has a comparable ionic radius to aluminum. The new single crystal compound also had its color change from transparent to a tinted yellow color which was reflected in absorption data showing a shifted peak. Conductivity measurements of the substituted sample showed a slightly reduced conductivity over a range of temperatures and oxygen pressures which is thought to be the result of a tighter binding of free oxygens to the iron [31].

While there has been more experimental work in applying cationic substitutions in the insulative mayenite system this material engineering approach has only begun to gain attention for the electride counterpart in the last decade. In 2015, Huang et al. completed an extensive

computational study of several cation substitutes (Mg^{2+}, Cu^{2+}, Sr^{2+}, Fe^{3+}, Ir^{4+}, P^{5+}, V^{5+}) on both insulative and reduced mayenite using DFT simulations [32]. This investigation only examined single atomic replacements for both calcium and aluminum and included an extra free oxygen in the cases of replacement with higher oxidation number atoms. Both cohesive and formation energies were calculated for the substituted and pure compounds. Cohesive energies showed that only the higher oxidation number substitutes (including an extra free encaged oxygen) led to greater lattice stability compared to pure mayenite. Meanwhile the formation enthalpies of all substituted species were higher, demonstrating the challenge that formation of substituted mayenite presents. Most substitutions induced lattice changes which followed Vegard's law (larger ionic radius of substituting atom leads to lattice growth) except for the copper and iridium substitutes. These substitutions induce much stronger alterations to the S4 fold symmetry and thus the framework is highly distorted [32]. This is further confirmed by local density of states maps for the substituted electride structures which shows a greater contribution from both Cu and Ir to the CCB, indicative of a greater change to the framework. In particular, it was noted that that Cu^{2+}species migrated from the cage wall toward the center of the cage which led to significant alteration to the cage window and created a "channel" between cages as seen in Figure 1.11. This channel was recreated at even lower levels of substitution for the copper species and demonstrates the possibility to increase electron interaction across cages leading to greater thermal stability and electronic conductivity.

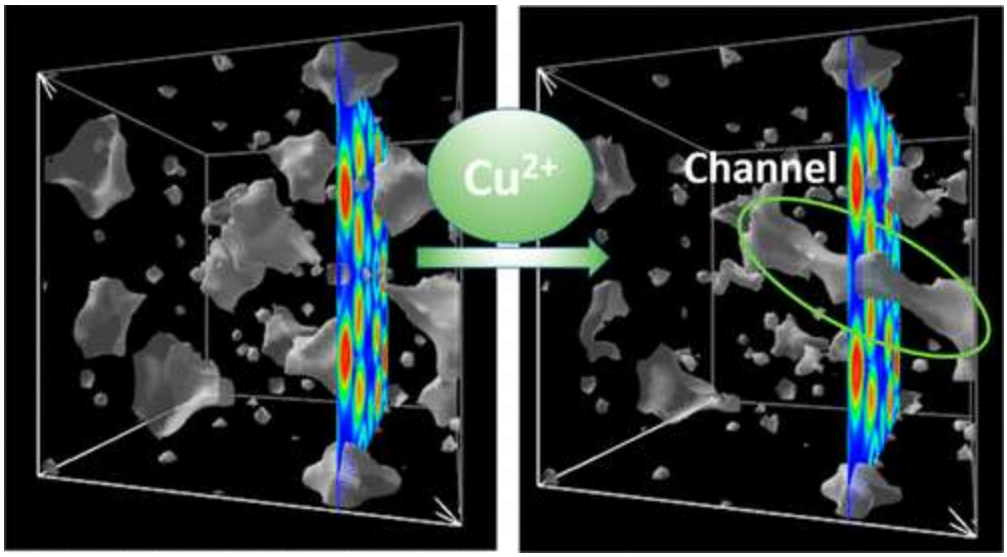

Figure 1.11 Creation of channel between cages via copper substitution [32]

More experimental studies have been conducted in the last five years to confirm and expand on computational predictions. In 2017 Ali et al. experimented with very low-level substitution of neodymium ($Ca_{11.988}Nd_{0.012}Al_{14}O_{33.006}$) on floating zone grown single crystal mayenite and reduced it to electride via Ti annealing over extended time periods (36-72hrs). Reduction to the black electride form was successful, though after 48hrs continued annealing led to more brittle, partially decomposed samples which was further reflected by the changes in conductivity [33]. Figure 1.12 shows electrical conductivity as a function of temperature and an Arrhenius plot for the pure single crystal electride annealed for 48hrs (a) as well as the neodymium substituted samples (b-e). All samples demonstrate metallic conductivity, however, the greatest conductivity is observed in sample c which was annealed for 48hrs while samples d and e showed a decreasing conductivity compared to the shorter annealing time samples.

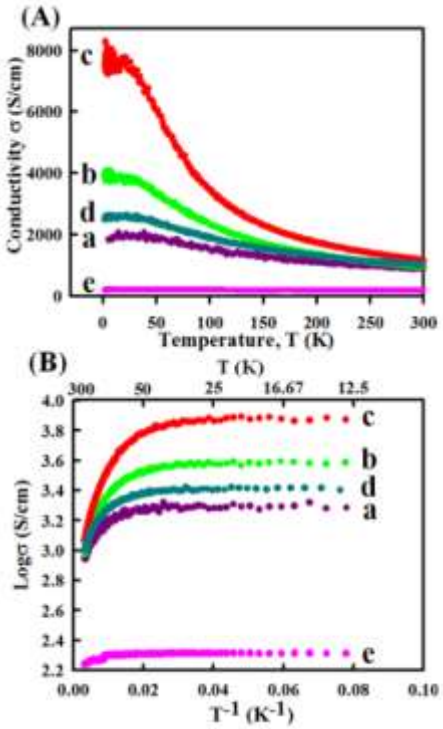

Figure 1.12 (a) Improvement of electrical conductivity for C12A7:e^- by Nd substitution (b) Arrhenius plot [33]

A similar effect was observed by Zhao et al. when they synthesized strontium substituted polycrystalline mayenite via powder SSR and reduced it via Ti treatment for 20hrs. The $Ca_{11.52}Sr_{0.48}Al_{14}O_{33}$ reduced sample achieved high conductivity (1136S/cm) compared to the pure sample (142S/cm) however, once the substitution profile was increased to $Ca_{11.4}Sr_{0.6}Al_{14}O_{33}$ conductivity dropped off to 25S/cm [34]. Again, it was partially attributed to structural issues as observed in scanning electron microscopy (SEM) (Figure 1.13) images wherein increased substitution led to increased porosity.

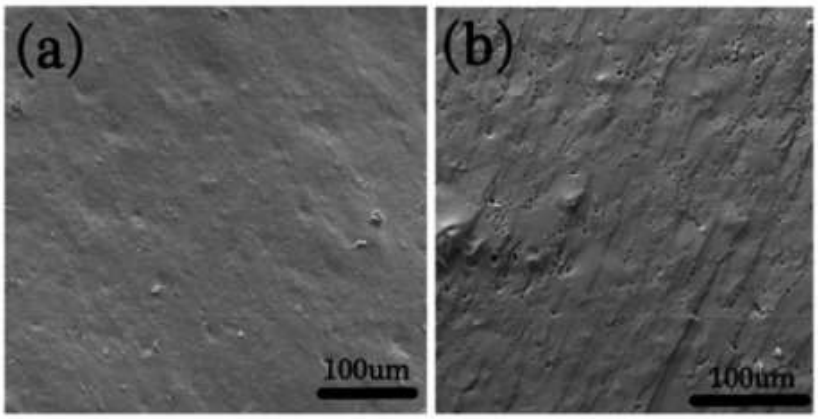

Figure 1.13 SEM micrographs of Sr substituted electride (a) $Sr_{0.48}$ level (b) $Sr_{0.6}$ level [35]

The increase in conductivity is also observed in the changes to the electron concentration which translates to an increased mobility as observed in Figure 1.14. This change was also reflected in the calculated density of states which showed that compared to the pure mayenite electride the Sr-substituted compound had more bands surrounding the Fermi energy level and broken down by element the strontium p-orbitals are seen to be the main contributor to the density of states around the Fermi level. Additionally, the FCB was shifted downward by 0.3eV allowing easier electronic conduction. Similar studies of cationic substitution of mayenite electride with Sn [35], Si [18], and Ga [18] have further confirmed that cation substitution has the capacity to improve electronic properties though there exists a range of improvement they offer as well as the limit on the capacity of the structure to handle large amounts of substitutional cations. Most experimental work in this field does not examine the oxidation behavior of the material nor the effects of cation substitution on thermionic emission.

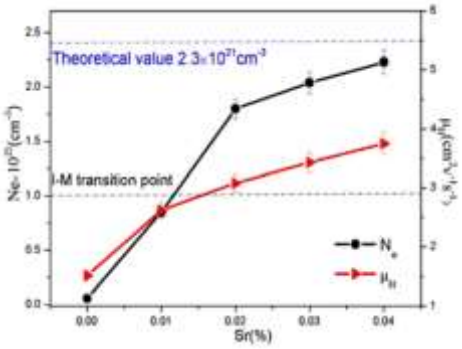

Figure 1.14 Electron concentration and mobility as a function of Sr substitutional dosage [34]

1.4 Strontium Vanadate

Perovskite oxides (ABO_3) where A and B are cations of different sizes (A>B) which bond to the oxygen, have attracted a great deal of attention in recent decades due to their applicability in energy transportation via phenomena such as thermoelectric conversion and thermionic emission. Perovskite oxides have a cubic structure (Figure 1.15) in which the B cations sit in the center of an octahedron of oxygens and the A cation is surrounded by the octahedrons.

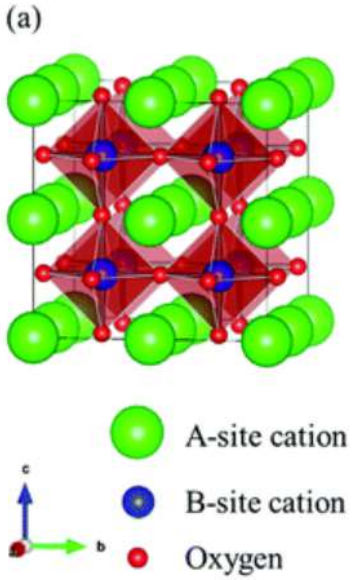

Figure 1.15 Structure of perovskite oxides [36]

This structure is attractive because it is accommodating to over 90% of metals on the periodic table which allows for extensive substitutions of cations [36], [37]. In an ideal touching hard sphere model the distance between the A cation and an O anion would be $a/\sqrt{2}$ and between B and O $a/2$. However, it has been observed that the cubic structure still exists apart from this ideal so Goldschmidt developed the tolerance factor seen in EQ(6) defined in terms of the ionic radii of the atoms to define the limits to wish the structure is maintained [37]. From this definition the cubic perovskite structure can generally accommodate 0.75<t<1.1.

$$t = \frac{r_A + r_O}{(r_B + r_O)\sqrt{2}} \qquad \text{EQ(6)}$$

Perovskite oxides containing transition metals have the unique quality of high electrical conductivity while theoretically still possessing low work function. The transition metal itself is highly correlated to the work function as the more ionic materials which contain metals like vanadium and niobium display lower theoretical work functions. This is based on the transition metal chemistry for which it is known that the 3d band for these metals is closer to the vacuum

level than that of metals like cobalt [38]. This was thoroughly explored by Ma et al. in a high throughput screening of perovskite oxides using DFT modeling. The group paired down a pool of over 2900 molecules using predicted work function, conductivity, and operating condition stability criteria in order to find candidates for electron emission. One of the trends discovered was that materials with a moderately populated d-band (1-3 electrons) were shown to have the lowest work function whereas the materials above and below this threshold often had work functions exceeding 2eV as shown in Figure 1.16 [36].

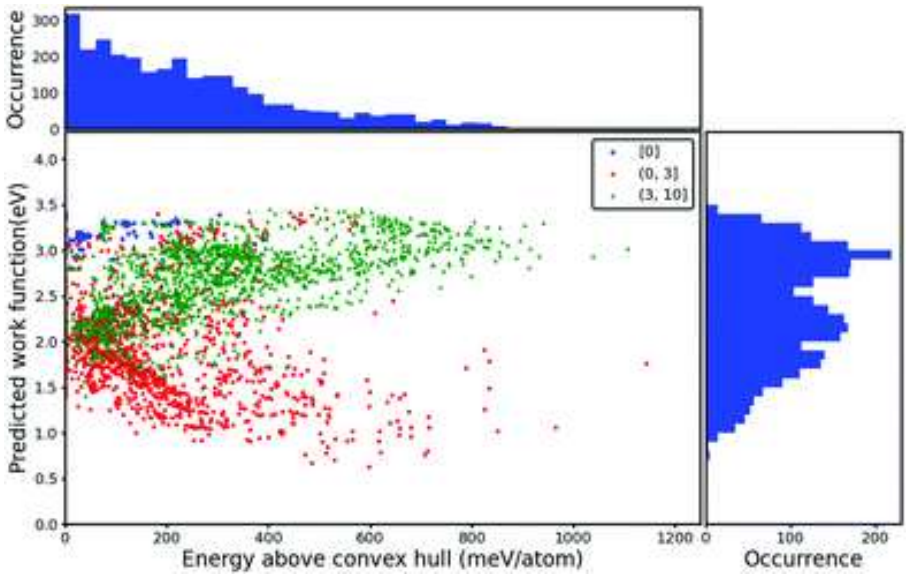

Figure 1.16 Plot of predicted work functions calculated using the O p-band center descriptor as a function of E_{hull} under typical thermionic cathode operating conditions for all materials in this study. The two histograms along x- and y-axis demonstrate the distribution of energies above convex hull and the distribution of predicted work functions, respectively. The blue, red and green symbols denote perovskites with n electrons in the d-band (n = 0, $0<n\leq3$, $3<n\leq10$, respectively), based on electron counting rules assuming complete ionic bonding [36]

Perovskite oxide materials have also shown improvement in their thermal stability as a result of cation replacement. Investigating A-site substitution, Arakawa et al. studied lanthanide cobalt perovskite oxides and found that stability decreased when lanthanum was substituted for the smaller europium [39]. This same trend was observed by Futai et al. [40] although further reducing the cation size (dysprosium) eventually bucked the trend and led to difficulties in

reducibility. Work analyzing Gibbs formation energies of lanthanide iron oxides showed that ΔG was negatively correlated with the tolerance factor, that is free energy was reduced with substitution of larger cations at the A-site [41]. B-site substitution has also shown a capacity to increase stability. Nakamura et al. studied a series of $LaMO_3$ (M=V, Cr, Mn, Fe, Co, Ni) compounds and found that stability in regard to $p(O_2)$ was again positively correlated with ionic radius of the M metal cation [42].

Though many of these perovskite oxide materials proposed by Ma have a theoretically low work function, few have been studied experimentally. Strontium vanadate ($SrVO_{3-\delta}$) is an oxygen-deficient perovskite oxide material which has been predicted to have a low work function according to Density Functional Theory modeling; modeling the SrO terminated surface (the AO surface generally has a lower work function than the BO_2 surface), Jacobs et al. observed a theoretical ultra-low work function of 1.79eV [43]. The material is made from a 2:1 stoichiometric mixture of strontium oxide and vanadium pentoxide. Vanadium sesquioxide can also be used as a starting powder, but this results in the formation of strontium orthovanadate ($Sr_3V_2O_8$) from which the cubic phase cannot be recovered [44], [45]. Traditionally the product is synthesized via solid state reaction of strontium carbonate and vanadium pentoxide at high temperatures (≥1373K) for long periods (≥10hrs) in a reducing atmosphere, such as a hydrogen-inert gas mixture, with intermediate regrinding steps [46]. It has also been shown that the cubic perovskite phase can be recovered through the reduction of the intermediate strontium pyrovanadate phase $Sr_2V_2O_7$, though this process has been shown to take longer (≥25hrs) [45]. In the few experimental works published, it has been documented to have excellent electrical conductivity in excess of 1000S/cm which is ascribed to the tetravalent V^{4+} ions in the $3d^1$ configuration which have a broad conduction band [44], [45], [46], [47]. Its conduction is also

assisted by the oxygen vacancies present which is represented by the $3-\delta$ term on the oxygen. Strontium vanadate also has the drawback of being prone to oxidation due to the open nature of the structure. As seen in the thermogravimetric analysis plot (Figure 1.17) over half of the vanadium cations have been oxidized to the pentavalent state before it reaches 900K which results in severely decreased conductivity [45].

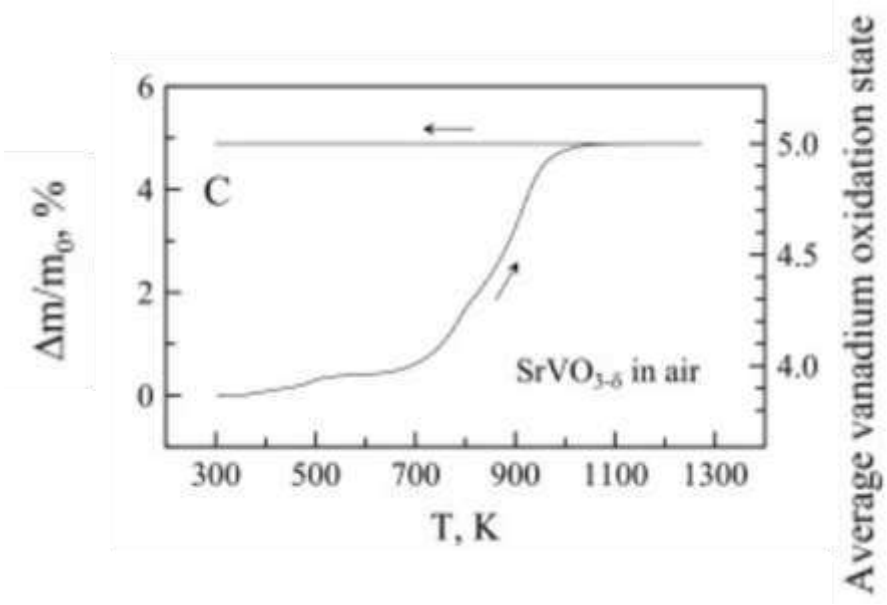

Figure 1.17 Thermogravimetric analysis of strontium vanadate in air [45] (modified)

Additionally, there has been little work on the effects of cation substitutions with this material. Miruszewski et al. synthesized strontium vanadate in which niobium was substituted for the vanadium at levels of 20, 50, and 80%. XRD results of the 20% substituted sample (Figure 1.18) showed slight peak shifting of the $SrVO_3$ peak indicating the integration of the larger niobium cation, but also present was a shifted $SrNbO_3$ indicating a substituted strontium niobate phase and also revealing possible solubility issues for Nb moving into the strontium vanadate lattice. The 20% substituted sample also showed a decrease in conductivity by an order of magnitude down from the 1500S/cm observed in the pure sample. The authors did not

measure mass gain under oxidizing atmosphere, but it was noted that both the 20% and 50% samples' conductivity degraded by a similar magnitude after 10 hours in an oxidizing atmosphere suggesting niobium did not sufficiently stabilize the material [48].

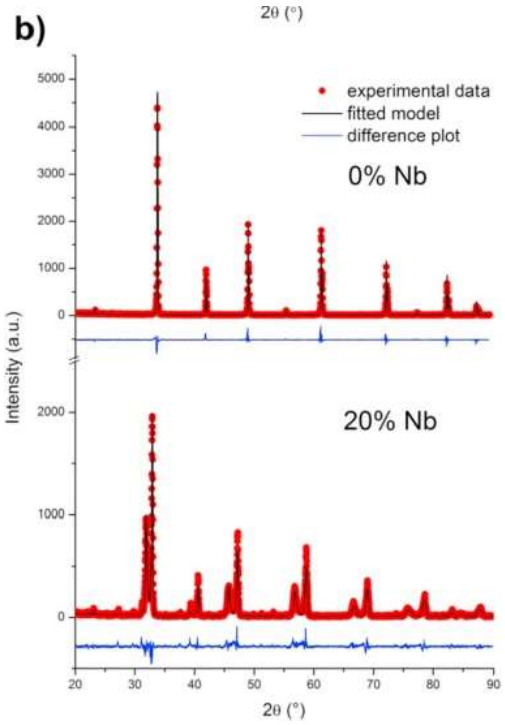

Figure 1.18 XRD plots of pure (top) and Nb substituted (bottom) strontium vanadate [48]

Macias et al. were able to improve resistance to oxidation while experimenting with simultaneous substitution of both Sr and V. Substituting 20% of strontium for yttrium raised the $p(O_2)$ stability boundary from 10^{-15} to $6*10^{-13}$ atm and the results were more pronounced for a lanthanum substitute which raised the limit as high as 10^{-5} atm (Figure 1.19). Interestingly, this also seemed to be correlated with the tolerance factor as stability increased as t moved toward unity. Simultaneous substitution combing niobium substitution for vanadium with the previous substitutions proved to be negligible (yttrium) or detrimental (lanthanum) to stability [46].

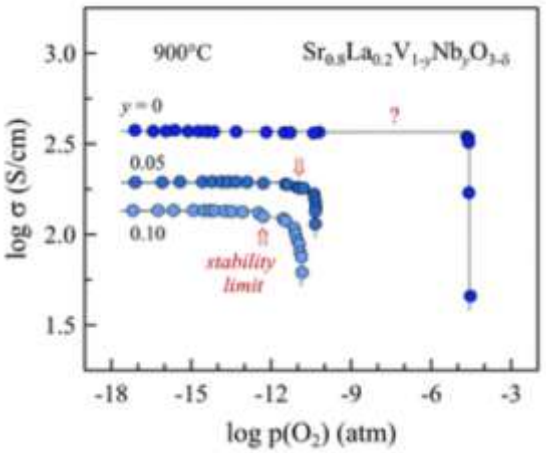

Figure 1.19 Log-log plot of oxygen pressure versus electrical conductivity for strontium vanadate with A and B-site substitutions [46]

Clearly there are possible advantages to cation substitution in the strontium vanadate structure. Jacobs DFT simulation of a Ba-enriched SrO surface revealed a possibly ultra-low work function of 1.07eV [43]. However, to my knowledge there has been no work to date which has experimentally investigated the effects of cation substitution on work function or even confirmed the predictions of its thermionic emission capabilities.

1.5 Motivation

Thermionic emission materials have a broad range of applications, including but not limited to, ionization sources for electric propulsion devices, electron beam generation for microscopy and spectroscopy, thermal management materials, and thermionic energy conversion. However, while thermionic emission shows promise in these capacities, there remains the issue that current materials must be operated at extremely high temperatures for meaningful current generation which opens the window for material instability and short material life cycles. The problem of implementing thermionic emission materials can be solved by either lowering the work function of the material such that devices can do meaningful work at low

temperatures or by improving material stability at high temperatures to extend the lifetime of the material. Intuitively these two solutions would seem to hold a contradiction: how can a material so easily emit electrons while maintaining stability? Mayenite electride is an interesting example of this phenomena because of the cage structure which gives rise to good thermal stability and low work function through the CCB. This high Fermi level as a result of the encaged electron is much different in comparison to more studied ionic solids such as oxide perovskites which have their low work functions ascribed to the d-band electrons in their structure. Still, both of them, as previously discussed, have shown the capacity for improvement to both electronic structure and stability with prescribed cation replacement. It is pertinent to develop further understanding of both materials in this regard in order to synthesize oxide ceramics with an ideal combination of work function and material stability such that it can be employed in thermionic emission devices.

1.6 Overarching Goals and Specific Aims

My primary research objective is to elucidate the connection between substitutional cations and lattice structure, thermal stability, and electronic conductivity of low work function oxide ceramic materials. In this endeavor, I have selected two promising ionic materials, $C12A7e^-$ and $SrVO_{3-\delta}$, as the foundational materials. My approach is geared toward enhancing both thermal stability and electronic structure through cation substitution. By conducting comprehensive studies on individual cation substitutions within each system, I aim to establish correlations between specific modifications and the key properties (onset of rapid oxidation, electrical conductivity) based on the attributes of the substituting cation (ionic radius, valence, dosage). Once these individual trends are identified, dual substitution will be utilized to synergize the optimal effects and/or to compensate for deficiencies from one cation with another.

Another key research objective is to assess the efficacy of employing Rietveld refinement in analyzing complex systems such as mayenite, in comparison to simpler systems like strontium vanadate. Rietveld refinement is a powerful technique for extracting detailed crystallographic information from powder diffraction data, and its application to complex structures is crucial for advancing our understanding of these materials. This research aims to evaluate the precision and accuracy of Rietveld refinement in resolving structural details of mayenite, characterized by its intricate lattice and multiple cation sites, against the relatively straightforward structure of strontium vanadate. By conducting a series of comparative studies, the goal is to identify the specific challenges and limitations encountered when applying Rietveld refinement to complex systems and to develop methodologies that enhance its reliability. This investigation will involve detailed analysis of the refinement process, including the handling of cation disorder, site occupancy, and thermal parameters, with the aim of establishing robust protocols for accurate structural characterization. The outcomes of this research are expected to significantly contribute to the refinement techniques used in materials science, providing a deeper understanding of the structural intricacies in complex materials and enhancing the accuracy of their crystallographic analyses.

The anticipated outcome of this research is to elucidate the mechanisms underlying the favorable properties of these materials. Specifically, my research aims to address the following scientific questions:

1) Which of the two cations in mayenite electride predominantly contributes to thermal stability? It is hypothesized that the size of the window between cages, through which electrons and free oxygen move, is the crucial factor controlling stability. Given that

more Al cations are present in this window, it is provisionally assumed that Al cations are the controlling factor.

2) What is the limiting cation size at both the A-site and B-site of strontium vanadate that would lead to phase breakdown as opposed to restricted oxidation? Generally, increasing cation size tends to reduce the space available for oxygen to fill vacancies and/or oxidize the V^{4+} cations in $SrVO_{3-\delta}$. However, there must be a limit to this effect for both sites.
3) What simultaneous substitution of both cations, i.e., dual substitution, can enhance the thermal stability of both materials while maintaining or increasing the electrical conductivity? The relevant hypothesis for mayenite electride is that selected cation substitutions should reduce the average size of the Ca site to restrict the window, as Ca^{2+} ions are larger than Al cations. Nevertheless, the work function must be compensated for by Al, as the density of states (DOS) around the Fermi level is largely due to the Ca^{2+} ions. For strontium vanadate, it is hypothesized that the low work function is attributed to the 3d band electrons of the V^{4+} ions. Thus, increasing the A-site size to improve stability should be balanced with slight adjustments to the B-site with cations possessing a similar amount of 3d band electrons, thereby enhancing both key properties.

This research is expected to provide significant insights into the development of advanced materials with superior high-temperature electronic properties.

References

[1] D. M. Trucchi and N. A. Melosh, "Electron-emission materials: Advances, applications, and models," *MRS Bulletin*, vol. 42, no. 7, pp. 488–492, Jul. 2017, doi: 10.1557/mrs.2017.142.

[2] K. Jensen, "Richardson–Laue–Dushman equation," in *Introduction to the Physics of Electron Emission*, John Wiley & Sons, Ltd, 2017, pp. 135–137. doi: 10.1002/9781119051794.ch12.

[3] D. B. Go *et al.*, "Thermionic Energy Conversion in the Twenty-first Century: Advances and Opportunities for Space and Terrestrial Applications," *Frontiers in Mechanical Engineering*, vol. 3, p. 13, 2017, doi: 10.3389/fmech.2017.00013.

[4] N. S. Rasor, "Thermionic energy conversion plasmas," *IEEE Transactions on Plasma Science*, vol. 19, no. 6, pp. 1191–1208, Dec. 1991, doi: 10.1109/27.125041.

[5] L. Uribarri and E. H. Allen, "Electron Transpiration Cooling for Hot Aerospace Surfaces," in *20th AIAA International Space Planes and Hypersonic Systems and Technologies Conference*, Glasgow, Scotland: American Institute of Aeronautics and Astronautics, Jul. 2015. doi: 10.2514/6.2015-3674.

[6] K. M. Hanquist, K. Hara, and I. D. Boyd, "Detailed modeling of electron emission for transpiration cooling of hypersonic vehicles," *Journal of Applied Physics*, vol. 121, no. 5, p. 053302, Feb. 2017, doi: 10.1063/1.4974961.

[7] K. M. Hanquist and I. D. Boyd, "Plasma Assisted Cooling of Hot Surfaces on Hypersonic Vehicles," *Front. Phys.*, vol. 7, 2019, doi: 10.3389/fphy.2019.00009.

[8] L. R. Falce and L. Garbini, "Chemistry and surface physics phenomena involved in the activation of impregnated tungsten dispenser cathodes," in *Fifth IEEE International*

Vacuum Electronics Conference (IEEE Cat. No.04EX786), Apr. 2004, pp. 295–296. doi: 10.1109/IVELEC.2004.1316325.

[9] D. R. Lev, I. G. Mikellides, D. Pedrini, D. M. Goebel, B. A. Jorns, and M. S. McDonald, "Recent progress in research and development of hollow cathodes for electric propulsion," *Rev. Mod. Plasma Phys.*, vol. 3, no. 1, p. 6, Dec. 2019, doi: 10.1007/s41614-019-0026-0.

[10] Y. Toda *et al.*, "Field Emission of Electron Anions Clathrated in Subnanometer-Sized Cages in [Ca24Al28O64]4+(4e-)," *Adv. Mater.*, vol. 16, no. 8, pp. 685–689, Apr. 2004, doi: 10.1002/adma.200306484.

[11] Y. Toda *et al.*, "Work Function of a Room-Temperature, Stable Electride [Ca24Al28O64]4+(e–)4," *Advanced Materials*, vol. 19, no. 21, pp. 3564–3569, 2007, doi: 10.1002/adma.200700663.

[12] S. Matsuishi *et al.*, "High-Density Electron Anions in a Nanoporous Single Crystal: [Ca24Al28O64]4+(4e-)," *Science*, vol. 301, no. 5633, pp. 626–629, Aug. 2003, doi: 10.1126/science.1083842.

[13] S. W. Kim and H. Hosono, "Synthesis and properties of 12CaO · 7Al2O3 electride: review of single crystal and thin film growth," *Philosophical Magazine*, vol. 92, no. 19–21, pp. 2596–2628, Jul. 2012, doi: 10.1080/14786435.2012.685770.

[14] H. Hosono and M. Kitano, "Advances in Materials and Applications of Inorganic Electrides," *Chem. Rev.*, vol. 121, no. 5, pp. 3121–3185, Mar. 2021, doi: 10.1021/acs.chemrev.0c01071.

[15] Y. Li, C. Liu, T. Zhang, M. Tian, and C. Peng, "Phase diagram assessment of CaO–Al $_2$ O $_3$ –La $_2$ O $_3$ system," *Canadian Metallurgical Quarterly*, vol. 56, no. 3, pp. 245–251, Jul. 2017, doi: 10.1080/00084433.2017.1327473.

[16] L. Palacios, A. Cabeza, S. Bruque, S. García-Granda, and M. A. G. Aranda, "Structure and Electrons in Mayenite Electrides," *Inorg. Chem.*, vol. 47, no. 7, pp. 2661–2667, Apr. 2008, doi: 10.1021/ic7021193.

[17] K. Khan *et al.*, "Facile metal-free reduction-based synthesis of pristine and cation-substituted conductive mayenite," *RSC Adv.*, vol. 8, no. 43, pp. 24276–24285, Jul. 2018, doi: 10.1039/C8RA02790K.

[18] K. Khan *et al.*, "Facile synthesis of a cationic-doped [Ca24Al28O64]4+(4e−) composite via a rapid citrate sol–gel method," *Dalton Trans.*, vol. 47, no. 11, pp. 3819–3830, Mar. 2018, doi: 10.1039/C7DT04543C.

[19] K. Khan *et al.*, "Facile synthesis of tin-doped mayenite electride composite as a non-noble metal durable electrocatalyst for oxygen reduction reaction (ORR)," *Dalton Trans.*, vol. 47, no. 38, pp. 13498–13506, Oct. 2018, doi: 10.1039/C8DT02548G.

[20] J. L. Dye, "Electrons as Anions," *Science*, vol. 301, no. 5633, pp. 607–608, Aug. 2003, doi: 10.1126/science.1088103.

[21] K. Hayashi, S. Matsuishi, T. Kamiya, M. Hirano, and H. Hosono, "Light-induced conversion of an insulating refractory oxide into a persistent electronic conductor," *Nature*, vol. 419, no. 6906, Art. no. 6906, Oct. 2002, doi: 10.1038/nature01053.

[22] K. Khan *et al.*, "A comprehensive review on synthesis of pristine and doped inorganic room temperature stable mayenite electride, [Ca24Al28O64]4+(e−)4 and its applications as a catalyst," *Progress in Solid State Chemistry*, vol. 54, pp. 1–19, Jun. 2019, doi: 10.1016/j.progsolidstchem.2018.12.001.

[23] J. H. Chung, J. H. Ryu, J. W. Eun, B. G. Choi, and K. B. Shim, “One-Step Synthesis of a 12CaO·7Al2O3 Electride via the Spark Plasma Sintering (SPS) Method,” *Electrochem. Solid-State Lett.*, vol. 14, no. 12, p. E41, Oct. 2011, doi: 10.1149/2.021112esl.

[24] T. Yoshizumi and K. Hayashi, “Thermionic Electron Emission from a Mayenite Electride–Metallic Titanium Composite Cathode,” *Appl. Phys. Express*, vol. 6, no. 1, p. 015802, Dec. 2012, doi: 10.7567/APEX.6.015802.

[25] X. Zhang *et al.*, “Sr-doping enhanced electrical transport and thermionic emission of single crystal 12CaO·7Al2O3 electride,” *Current Applied Physics*, vol. 20, no. 1, pp. 96–101, Jan. 2020, doi: 10.1016/j.cap.2019.10.008.

[26] P. V. Sushko, A. L. Shluger, M. Hirano, and H. Hosono, “From Insulator to Electride: A Theoretical Model of Nanoporous Oxide 12CaO·7Al2O3,” *J. Am. Chem. Soc.*, vol. 129, no. 4, pp. 942–951, Jan. 2007, doi: 10.1021/ja066177w.

[27] J. T. S. Irvine and A. R. West, “Ca12Al14O33 solid electrolytes doped with zinc and phosphorus,” *Solid State Ionics*, vol. 40–41, pp. 896–899, Aug. 1990, doi: 10.1016/0167-2738(90)90147-J.

[28] M. I. Bertoni, T. O. Mason, J. E. Medvedeva, A. J. Freeman, K. R. Poeppelmeier, and B. Delley, “Tunable conductivity and conduction mechanism in an ultraviolet light activated electronic conductor,” *Journal of Applied Physics*, vol. 97, no. 10, p. 103713, May 2005, doi: 10.1063/1.1899246.

[29] M. I. Bertoni, T. O. Mason, J. E. Medvedeva, Y. Wang, A. J. Freeman, and K. R. Poeppelmeier, “Enhanced electronic conductivity in Si-substituted calcium aluminate,” *Journal of Applied Physics*, vol. 102, no. 11, p. 113704, Dec. 2007, doi: 10.1063/1.2817605.

[30] L. Palacios, S. Bruque, and M. A. G. Aranda, “Structure of gallium-doped mayenite and its reduction behaviour,” *physica status solidi (b)*, vol. 245, no. 4, pp. 666–672, 2008, doi: 10.1002/pssb.200743425.

[31] S. G. Ebbinghaus, H. Krause, D.-K. Lee, and J. Janek, “Single Crystals of C12A7 (Ca12Al14O33) Substituted with 1 mol % Iron,” *Crystal Growth & Design*, vol. 14, no. 5, pp. 2240–2245, May 2014, doi: 10.1021/cg401823k.

[32] J. Huang, L. Valenzano, and G. Sant, “Framework and Channel Modifications in Mayenite (12CaO·7Al2O3) Nanocages By Cationic Doping,” *Chem. Mater.*, vol. 27, no. 13, pp. 4731–4741, Jul. 2015, doi: 10.1021/acs.chemmater.5b01360.

[33] M. M. Ali, “Floating Zone Growth and Characterization of (Ca1–xNdx)12Al14O33+6x (x ∼ 0.001) Single Crystals,” *ACS Omega*, vol. 2, no. 1, pp. 127–127, Jan. 2017, doi: 10.1021/acsomega.6b00544.

[34] J. Zhao, X. Zhang, H. Liu, Y. Xiao, H. Jiang, and J. Zhang, “Synthesis and Characterization of (Ca1−xSrx)12Al14O33 Electrides,” *Crystal Research and Technology*, vol. 53, no. 1, p. 1700201, 2018, doi: 10.1002/crat.201700201.

[35] Q. Hu, R. Tan, W. Yao, Y. Cui, J. Li, and W. Song, “Preparation and X-ray photoelectron spectroscopic characterization of Sn-doped C12A7:e− electride nanoparticles,” *Applied Surface Science*, vol. 508, p. 145244, Apr. 2020, doi: 10.1016/j.apsusc.2019.145244.

[36] T. Ma, R. Jacobs, J. Booske, and D. Morgan, “Discovery and engineering of low work function perovskite materials,” *Journal of Materials Chemistry C*, vol. 9, no. 37, pp. 12778–12790, 2021, doi: 10.1039/D1TC01286J.

[37] M. A. Peña and J. L. G. Fierro, “Chemical Structures and Performance of Perovskite Oxides,” *Chem. Rev.*, vol. 101, no. 7, pp. 1981–2018, Jul. 2001, doi: 10.1021/cr980129f.

[38] M. T. Greiner, L. Chai, M. G. Helander, W.-M. Tang, and Z.-H. Lu, “Transition Metal Oxide Work Functions: The Influence of Cation Oxidation State and Oxygen Vacancies,” *Adv. Funct. Mater.*, vol. 22, no. 21, pp. 4557–4568, Nov. 2012, doi: 10.1002/adfm.201200615.

[39] T. Arakawa, N. Ohara, and J. Shiokawa, “Reduction of perovskite oxide LnCoO3(Ln = La-Eu) in a hydrogen atmosphere,” *J Mater Sci*, vol. 21, no. 5, pp. 1824–1827, May 1986, doi: 10.1007/BF01114746.

[40] M. Futai, C. Yonghua, and Louhui, “Characterization of perovskite-type oxide catalysts RECoO3 by TPR,” *React Kinet Catal Lett*, vol. 31, no. 1, pp. 47–54, Mar. 1986, doi: 10.1007/BF02062510.

[41] T. Katsura, T. Sekine, K. Kitayama, T. Sugihara, and N. Kimizuka, “Thermodynamic properties of Fe-lathanoid-O compounds at high temperatures,” *Journal of Solid State Chemistry*, vol. 23, no. 1, pp. 43–57, Jan. 1978, doi: 10.1016/0022-4596(78)90052-X.

[42] T. Nakamura, G. Petzow, and L. J. Gauckler, “Stability of the perovskite phase LaBO3 (B = V, Cr, Mn, Fe, Co, Ni) in reducing atmosphere I. Experimental results,” *Materials Research Bulletin*, vol. 14, no. 5, pp. 649–659, May 1979, doi: 10.1016/0025-5408(79)90048-5.

[43] R. M. Jacobs, D. Morgan, and J. H. Booske, “Strontium vanadate: An ultra-low work function electron emission material,” in *2015 IEEE International Vacuum Electronics Conference (IVEC)*, Apr. 2015, pp. 1–2. doi: 10.1109/IVEC.2015.7223772.

[44] T. Maekawa, K. Kurosaki, and S. Yamanaka, “Physical properties of polycrystalline SrVO3−δ,” *Journal of Alloys and Compounds*, vol. 426, no. 1, pp. 46–50, Dec. 2006, doi: 10.1016/j.jallcom.2006.02.026.

[45] J. Macías, A. A. Yaremchenko, and J. R. Frade, “Redox transitions in strontium vanadates: Electrical conductivity and dimensional changes,” *Journal of Alloys and Compounds*, vol. 601, pp. 186–194, Jul. 2014, doi: 10.1016/j.jallcom.2014.02.148.

[46] J. Macías, “Enhanced stability of perovskite-like SrVO3-based anode materials by donor-type substitutions,” *Journal of Materials Chemistry A*, p. 9, 2016.

[47] J. A. Moyer, C. Eaton, and R. Engel-Herbert, “Highly Conductive SrVO3 as a Bottom Electrode for Functional Perovskite Oxides,” *Advanced Materials*, vol. 25, no. 26, pp. 3578–3582, 2013, doi: 10.1002/adma.201300900.

[48] T. Miruszewski, B. Kamecki, M. Łapiński, and J. Karczewski, “Fabrication, structural and electrical properties of Sr(V,Nb)O3-δ perovskite materials,” *Materials Chemistry and Physics*, vol. 212, pp. 446–452, Jun. 2018, doi: 10.1016/j.matchemphys.2018.03.070.

Chapter 2 General Approach

This chapter provides an overview of the major aspects of the approach I took in this research including the material selection and synthesis, structural modeling, and characterization methods. More details regarding the specific characterization or testing method are provided in individual chapters concerning different material systems.

2.1 Material Selection

My research focused primarily on the two material systems described in chapter one: mayenite electride and strontium vanadate, driven by their inherently low work functions that give promising application in the field of thermionic emission. Both materials systems can be made from naturally abundant and cost-effective precursor materials, which makes these two material systems competitive relative to other thermionic emissive materials like lanthanum hexaboride, which are much rarer and over ten times the cost. Mayenite electride and strontium vanadate also have radical differences in their structures which give rise to their desirable properties. These differences make the simultaneous study of them useful to informing effectiveness of the approach taken hereafter (cation substitution). The future improvement of the materials, as well as other electride or perovskite systems, can be streamlined with the knowledge generated in this study.

Mayenite electride is an intriguing candidate for thermionic emission material due to its unique structural and electronic properties [1], [2]. Alloying and substitution with elements such as titanium and strontium have been shown to enhance its thermionic emission capabilities by reducing the work function and increasing electron density and mobility [3], [4]. The thermal

stability of mayenite electride, relative to organic electrides, is another significant advantage that enables thermionic emission applications operating at high temperatures. To achieve consistent performance, it is essential to maintain structural integrity and electronic properties over a wide temperature range. This stability ensures that mayenite electride can reliably function in demanding thermal environments without significant degradation. The material's promising properties are attributed to its unique and complex structure, which enables both chemical stability and gives rise to the cage conduction band, which enables efficient electron transport, making mayenite electride a viable option for various engineering applications in thermionic emission.

Strontium vanadate, on the other hand, has a relatively simple cubic perovskite structure. This cubic perovskite structure is more readily to accommodate a wide range of cations, allowing for extensive substitutions to tailor its properties. Strontium vanadate exhibits high electrical conductivity, exceeding 1000S/cm, attributed to its tetravalent vanadium ions and oxygen vacancies [5], [6]. Despite its susceptibility to oxidation, previous studies have shown that strategic substitution can significantly improve its oxidation resistance, expanding its operational stability under various conditions [7], [8]. These attributes make strontium vanadate a highly attractive material for thermionic emission applications.

Selection of these two promising thermionic material systems was motivated by the two different mechanisms leading to their low work function, respectively. The scientific insights into the role of lattice structure, large unit cell with caged structure vs. relatively simple perovskite cubic structure, will promote extensive and more in-depth research on potential thermionic materials that can operate at harsh environments such as high temperatures or oxidizing environments.

2.2 Material Synthesis and Processing

In my work, the materials were synthesized and processed via a combination of powder solid state reactions (PSSR) and spark plasma sintering (SPS). Starting powders of purity ≥99.0% were mixed in the appropriate stoichiometric ratio as previously outlined and ball milled for 10 hours. Once powders are milled, any needed initial solid-state reaction prior to sintering was carried out in a furnace in either an ambient air (mayenite) or reducing (strontium vanadate) environment. Powder solid state reaction is chosen over other methods such as ethylene glycol as it has a shorter time scale. Once the substituted powders are formed, they are prepared for SPS. This entails loading the powder into a 20mm diameter graphite die. Contact between the powder and tooling is improved with graphite foil surrounding the powder on the die wall as well as on the top and bottom where the powder is compressed by graphite punches. The powders are compressed to a green body with pressure 40MPa prior to sintering. SPS is chosen as the method

for sintering as the joule heating and simultaneous axial pressure allow for rapid sintering of samples. The synthesis and processing flow is shown in Figure 2.1.

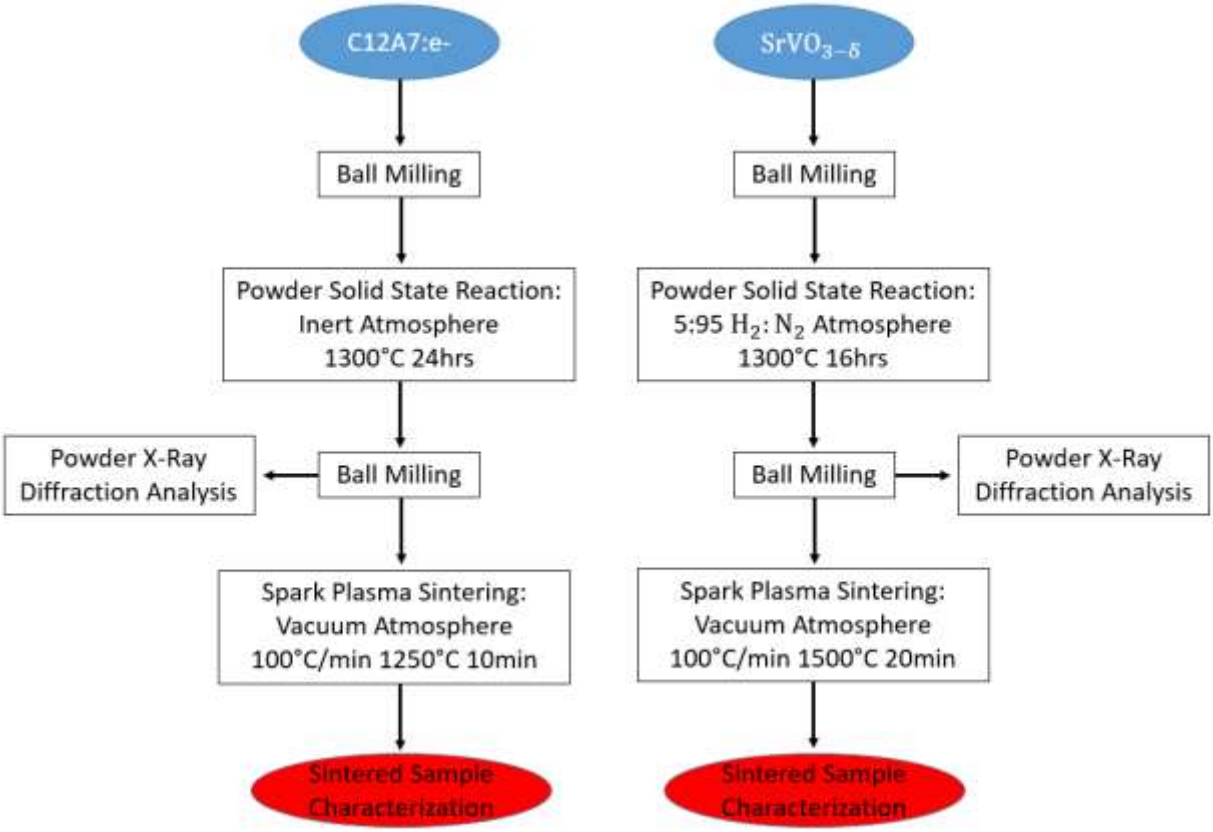

Figure 2.1 Powder Processing and Sample Synthesis Workflow

2.3 Structure Modeling - Rietveld Refinement

One of the pillars of this research is studying the effects of cation substitutions on crystal structures and this is modeled using Rietveld refinement. Rietveld refinement is a sophisticated technique in crystallography used to extract detailed structural information from X-ray diffraction data [9], [10], [11]. This method allows for determination of atomic positions, thermal vibrations, and other structural parameters of crystalline materials. The process begins with the collection of diffraction data, followed by proposing an initial structural model. A theoretical diffraction pattern is then calculated and compared to the experimental pattern. Through iterative

adjustments, the differences between the calculated and experimental patterns are minimized using least-squares fitting. Parameters such as lattice dimensions, atomic positions, thermal vibrations, and occupancy factors are "refined" (adjusted) in order to minimize the difference between the calculated and observed patterns. The quality of the refinement is evaluated using statistical indicators like the weighted profile R-factor (R_{wp}). As discussed by Toby, R-factor should not be the only measure of model quality; therefore, graphical inspection and chemical plausibility are also considered in this work [12]. This technique provides evidence for successful cation substitutions through examination of both atomic position movement (mayenite) and substitutional cation occupancy (strontium vanadate).

2.4 Material Characterization Methods

Figures 2.4 and 2.5 provide the characterization and testing methods that were applied to investigate the lattice structure and properties of the two material systems. Characterization is geared toward establishing correlations between the cation substitutes, lattice change, and key properties as outlined in the Chapter 1 specific aims. The crystal structures of each sample were analyzed using powder X-ray diffraction (XRD) with a Bruker D8 Discover DaVinci Powder X-ray Diffractometer, scanning 2θ ranges of 15°-120° (mayenite) and 20°-150° (strontium vanadate) with kα radiation. The phase composition was identified by matching patterns to the International Center for Diffraction Data (ICDD) database, focusing on secondary calcium aluminate phases (for mayenite), secondary phases in the $SrO\text{-}V_2O_5$ phase diagram, and precursor powders. Lattice parameters and structural data were calculated through Rietveld refinement using TOPAS6 software, with a small amount of silicon added to the powder to correctly model sample height displacement and improve lattice parameter calculations. The refinement process included fitting the silicon peak to correct sample height displacement,

adjusting background, lattice, and peak shape parameters, followed by positional and isotropic displacement parameters, and finally refining occupancies. The microstructures of the samples were characterized in SEM/EDS to examine porosity and homogeneity in microstructure. As the substitution level is very low and is not inspectable via SEM, only representative SEM images for each material system are provided below to demonstrate the typical microstructure.

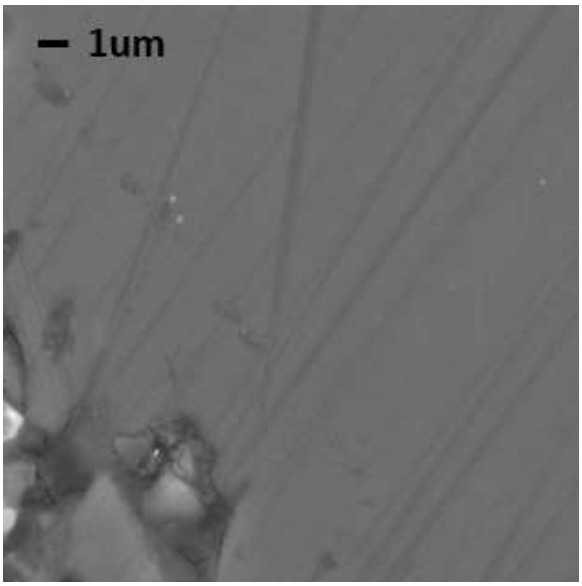

Figure 2.2 SEM Micrograph Mayenite Electride

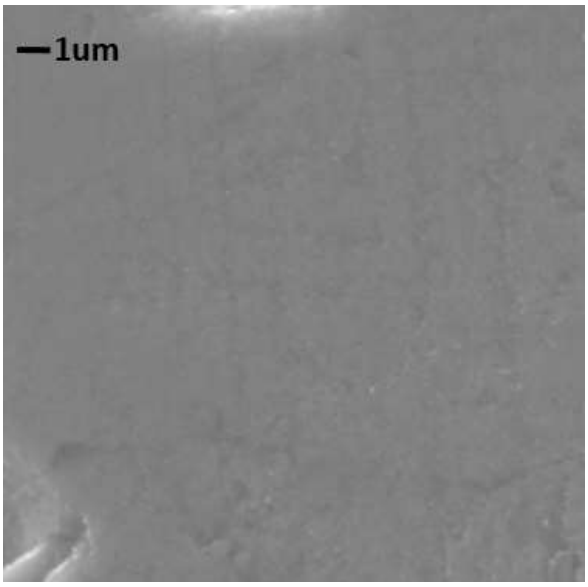

Figure 2.3 SEM Micrograph Strontium Vanadate

Thermal analysis involved cutting and polishing small samples for thermogravimetric analysis (SEIKO) in an ambient atmosphere with a heating rate of 10°C/min from 50°C to 1050°C. Oxidation points were determined using the second derivative of polynomial fits to mass change data, and the rate of oxidation was reported as percent mass change over time. Some of the strontium vanadate samples have two inflection points indicative of the typical two stage oxidation. Delay in rapid oxidation is considered representative of the thermal stability of the sample as increased resistance to oxidation allows samples to be used for thermionic emission at higher temperatures thus allowing for extraction of greater currents.

Electrical conductivity testing involved cutting sintered samples into rectangular bars, attaching copper leads with silver epoxy, and measuring electrical resistance as a function of temperature (from 25°C to 125°C in ten-degree increments) using a four-probe setup in a Quantum Design Physical Property Measurement System (PPMS). Resistance was calculated from voltage measurements at various input currents, with three measurements averaged at each temperature point. Data presented is that which showed minimum shift in phase angle of AC current indicative of reliability. Electrical conductivity has shown to be negatively correlated with work function (lower work function observed with higher electrical conductivity) in cation substituted mayenite electride. Very limited data exists for strontium vanadate, but DFT simulations have shown that the work function is tied to the d-band electrons of the structure which are also highly correlated with the electrical conductivity [13], [14]. Thus, for both material systems, electrical conductivity is considered to be negatively correlated with work function.

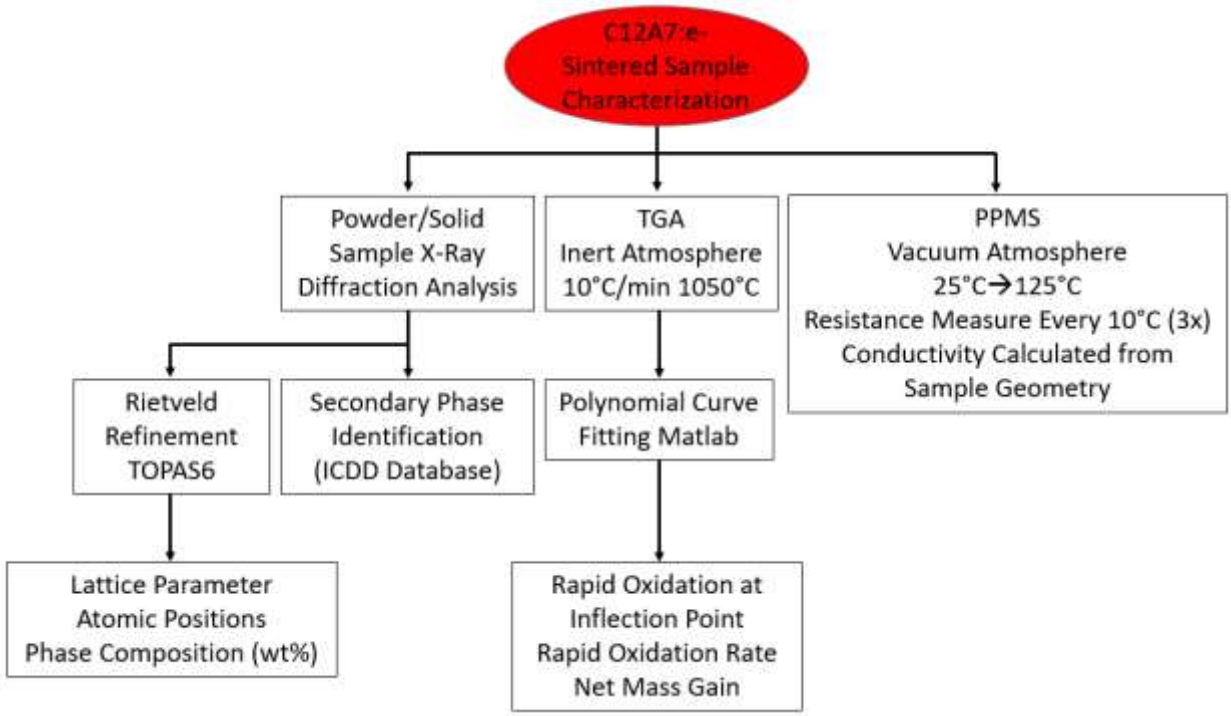

Figure 2.4 Mayenite Electride Characterization Flowchart

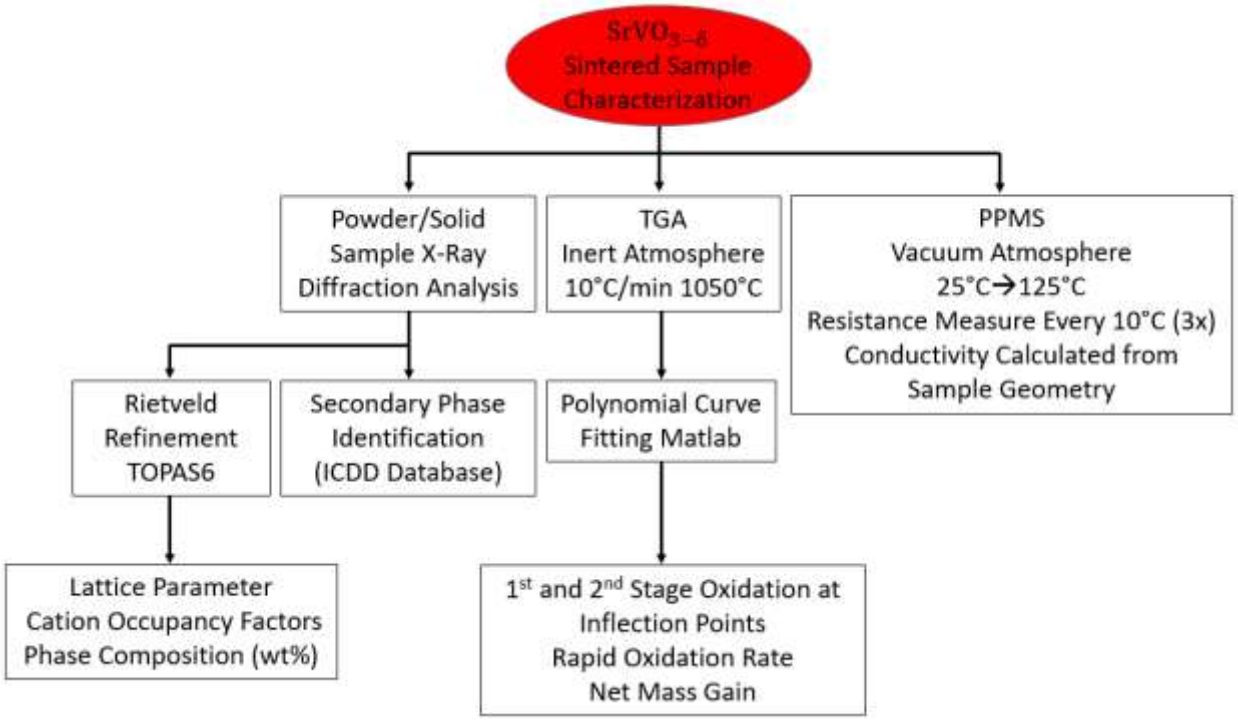

Figure 2.5 Strontium Vanadate Characterization Flowchart

References

[1] S. Matsuishi *et al.*, "High-Density Electron Anions in a Nanoporous Single Crystal: [Ca24Al28O64]4+(4e-)," *Science*, vol. 301, no. 5633, pp. 626–629, Aug. 2003, doi: 10.1126/science.1083842.

[2] Y. Toda *et al.*, "Work Function of a Room-Temperature, Stable Electride [Ca24Al28O64]4+(e–)4," *Adv. Mater.*, vol. 19, no. 21, pp. 3564–3569, 2007, doi: 10.1002/adma.200700663.

[3] T. Yoshizumi and K. Hayashi, "Thermionic Electron Emission from a Mayenite Electride–Metallic Titanium Composite Cathode," *Appl. Phys. Express*, vol. 6, no. 1, p. 015802, Dec. 2012, doi: 10.7567/APEX.6.015802.

[4] X. Zhang *et al.*, "Sr-doping enhanced electrical transport and thermionic emission of single crystal 12CaO·7Al2O3 electride," *Curr. Appl. Phys.*, vol. 20, no. 1, pp. 96–101, Jan. 2020, doi: 10.1016/j.cap.2019.10.008.

[5] T. Maekawa, K. Kurosaki, and S. Yamanaka, "Physical properties of polycrystalline SrVO3−δ," *J. Alloys Compd.*, vol. 426, no. 1, pp. 46–50, Dec. 2006, doi: 10.1016/j.jallcom.2006.02.026.

[6] J. Macías, A. A. Yaremchenko, and J. R. Frade, "Redox transitions in strontium vanadates: Electrical conductivity and dimensional changes," *J. Alloys Compd.*, vol. 601, pp. 186–194, Jul. 2014, doi: 10.1016/j.jallcom.2014.02.148.

[7] J. Macías, A. A. Yaremchenko, and J. R. Frade, "Enhanced stability of perovskite-like SrVO3-based anode materials by donor-type substitutions," *J. Mater. Chem. A*, vol. 4, no. 26, pp. 10186–10194, Jun. 2016, doi: 10.1039/C6TA02672A.

[8] J. Macías, A. A. Yaremchenko, E. Rodríguez-Castellón, M. Starykevich, and J. R. Frade, "Compromising Between Phase Stability and Electrical Performance: SrVO3–SrTiO3 Solid Solutions as Solid Oxide Fuel Cell Anode Components," *ChemSusChem*, vol. 12, no. 1, pp. 240–251, 2019, doi: 10.1002/cssc.201801727.

[9] T. Runčevski and C. M. Brown, "The Rietveld Refinement Method: Half of a Century Anniversary," *Cryst. Growth Des.*, vol. 21, no. 9, pp. 4821–4822, Sep. 2021, doi: 10.1021/acs.cgd.1c00854.

[10] T. A. Para, S. K. Sarkar, T. A. Para, and S. K. Sarkar, "Challenges in Rietveld Refinement and Structure Visualization in Ceramics," in *Advanced Ceramic Materials*, IntechOpen, 2021. doi: 10.5772/intechopen.96065.

[11] L. B. McCusker, R. B. Von Dreele, D. E. Cox, D. Louër, and P. Scardi, "Rietveld refinement guidelines," *J. Appl. Crystallogr.*, vol. 32, no. 1, pp. 36–50, Feb. 1999, doi: 10.1107/S0021889898009856.

[12] B. H. Toby, "R factors in Rietveld analysis: How good is good enough?," Powder Diffraction, vol. 21, no. 1, pp. 67–70, Mar. 2006, doi: 10.1154/1.2179804.

[13] H. He, Z. Yang, Y. Xu, A. T. Smith, G. Yang, and L. Sun, "Perovskite oxides as transparent semiconductors: a review," *Nano Converg.*, vol. 7, no. 1, p. 32, Oct. 2020, doi: 10.1186/s40580-020-00242-7.

[14] T. Ma, R. Jacobs, J. Booske, and D. Morgan, "Discovery and engineering of low work function perovskite materials," *J. Mater. Chem. C*, vol. 9, no. 37, pp. 12778–12790, 2021, doi: 10.1039/D1TC01286J.

Chapter 3 Effects of Individual and Dual Cationic Substitutions in Mayenite on Its Structure, Thermal stability and Electrical Conductivity

This research began with an interest in the unique nature of mayenite electride. This relatively new material is capable of housing free anion-like electrons in the cavities of its structure and this property can be harnessed for solving a variety of engineering problems. Moreover, as more inorganic electrides are developed, there is a growing need to expand the study of this material to understand the relationship between its structure and properties. This chapter covers an investigation of several cation substitutions for the framework calcium (Ca) and aluminum (Al) ions in the lattice of mayenite both in oxy- status and electride status. It is anticipated that cation substitutions induce substantial structural changes, which subsequently modify the thermal stability and electrical conductivity of the material. Additionally, dual substitution, simultaneous replacement of both the Ca and Al ion sites, is explored as a possible solution to couple effects observed from individual substitutions. The approach of dual cationic substitution is novel and has not been reported for this material. X-ray diffraction in combination with Rietveld refinement is used to characterize the structural changes in the material; thermal stability is characterized via thermogravimetric analysis to reveal oxidation kinetics; and electrical conductivity is measured for a temperature range of 25°C-125°C. Results suggest that substitution with smaller cations leads to substantial resistance to oxidation and that dual substitution is dominated by effects from one of the replacements.

3.1 Introduction

Electrons are central to many fields of study within the realm of materials engineering and thus the conception of electrides that emerged in the 1990s was met with great excitement.

The realization of crystal structures with specific anion sites occupied by "free" or delocalized electrons pointed toward a frontier of materials with new chemical, optical, magnetic, and electrical properties that could be harnessed for a variety of applications. However, the initial group of electrides were all organic materials (alkali metals combined with complexants) which are sensitive to air and moisture and tend to decompose above 40°C, and thus have very limited practical use [1], [2]. Hosono et al., developed a stable inorganic electride material based on mayenite via reduction processes [3]. The new material, mayenite electride, became a representative electride material for thermionic emission applications [4], [5], [6], [7], [8].

Mayenite, or $Ca_{12}Al_{14}O_{33}$ (C12A7), is a stoichiometric compound of the $CaO\text{-}Al_2O_3$ system with a 12:7 ratio of calcium oxide to alumina. The crystal structure of C12A7 consists of a series of cages, which make up a positively charged framework. In the unit cell of the material sits twelve cages which, in total, have a 4+ charge, which is balanced by two oxygen anions that are randomly distributed amongst the twelve cages. Therefore, the material is sometimes written as $[Ca_{24}Al_{28}O_{64}]^{4+}(O^{2-})_2$. Mayenite has a cubic structure which belongs to the $I\bar{4}3d$ space group, and the positions of the framework atoms are given in Table 3.01. These positions only hold true for the unoccupied cages as the oxygen anions are not stable in the center of the cage due to the cage's large diameter (4.5Å) being more than 50% larger than the oxygen anion's diameter [9], [10]. In cages populated with oxygen anions, some of the cations have displaced sites as shown in Table 3.02 and Figure 3.01. This also shows that the free oxygen is prone to sitting off the center position of the cage (0.375, 0, 0.25). While the oxygen anions share bonds with the framework Ca cations and some of the framework Al cations, they are still considered as "free" oxygen ions as this bonding is weak due to the large cage diameter. The free oxygen anions can move between cages but are restricted by the size of the cage windows, rings of Ca1-O2-Al1-O1-

Al2-O2 structure. This is one of the essential structural features of mayenite (and its electride derivative) that gives rise to its thermal stability and resistance to oxidation below 400°C [11].

Table 3.01 Positions for Framework Atoms in Mayenite Structure. Lattice parameters: a~11.99Å, space group $I\bar{4}3d$

Site	**Wyckoff**	**x**	**y**	**z**
Ca1	24d	0.15	0	0.25
Al1	16c	0.018	0.018	0.018
Al2	12b	0.875	0	0.25
O1	48e	0.03	0.44	0.15
O2	16c	0.18	0.18	0.18

Table 3.02 Positions for Framework Atoms and the Displaced Variants of Framework Atoms in Mayenite Structure. Lattice parameters: a~11.99Å, space group $I\bar{4}3d$

Site	**Wyckoff**	**x**	**y**	**z**
Ca1	24d	0.15	0	0.25
Ca2	24d	0.17	0	0.25
Ca3	24d	0.18	0	0.25
Al1	16c	0.018	0.018	0.018
Al2	12b	0.875	0	0.25
Al3	48e	0.3	0.19	0.26
O1	48e	0.03	0.44	0.15
O2	16c	0.18	0.18	0.18
O3	48e	0.36	0.05	0.24

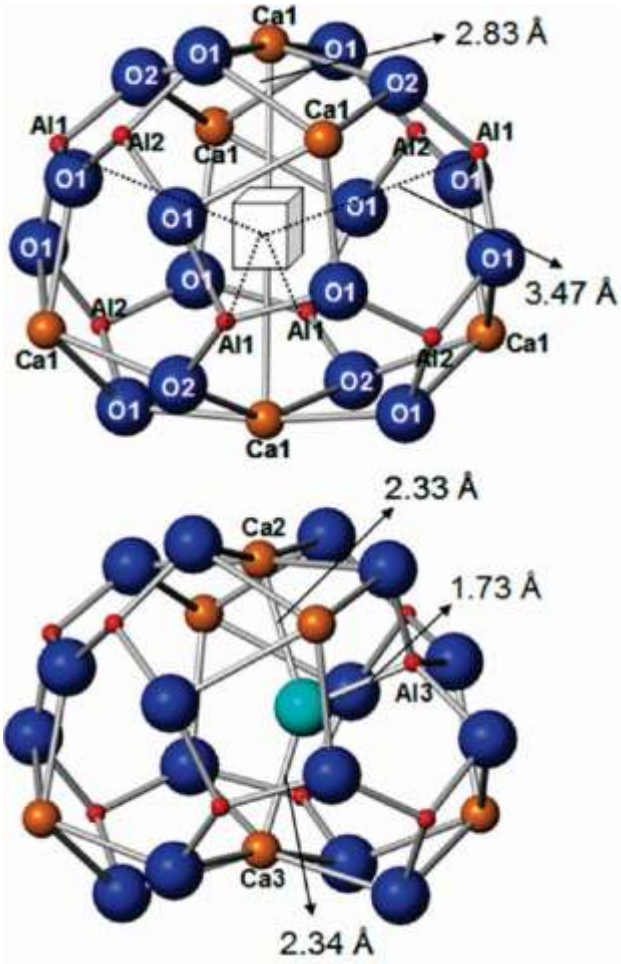

Figure 3.01 Unoccupied (upper) and Occupied Insulative Mayenite Cages with Displaced Framework Cations [9]

Reduction of mayenite to the electride form is done by drawing out the oxygen atoms from the center of the cage, leaving behind four electron anions which are randomly distributed throughout the twelve cages [12], [13], [14]. This has a pronounced effect on the electronic structure of the material. Insulative mayenite has a band structure comprised of a framework conduction band (FCB), a valence band (VB), and a cage conduction band (CCB) which sits between the two (Figure 1.10). The FCB is entirely comprised of states of the framework cations. The CCB is comprised of electronic states in the "empty space" of the unoccupied cages. This can be thought of as interconnected network of "particle in a box" like states, dependent on all of the framework cations equally [14]. As more free oxygens are replaced, the electron density increases, causing the cage conduction band (CCB) to widen. Simultaneously, the CCB and

framework conduction band (FCB) decrease in energy, with some CCB states beginning to overlap with the states of the electron anions [15]. In total, this results in a massive increase to the electrical conductivity to the material (1500S/cm) [16]. The increased anion replacement also results in an increase to the fermi level of the material, giving rise to mayenite electride's low work function (2.4eV) [15], [17]. From this perspective, it is clear that the framework cations have a strong influence on the electronic state of the material in that it can alter the states of the CCB and can limit the amount of electron density by controlling the window through which the oxygen anions escape.

While mayenite electride has immense promise as a thermionic emission material, its instability when temperature is higher than 400 °C yet constrains its widespread use in the field. For example, the amount of emission current is limited as mayenite electride oxidizes in air at temperatures above 400°C. Current materials at the forefront of this space, such as BaO-W, can survive up to 1000°C without suffering serious oxygen poisoning or material degradation [8]. One way to expand the capabilities of mayenite electride is through cation substitution. Several works have explored different substitutions for both Ca and Al in the cage framework. Most of these substitutions have focused on improving the electrical properties either by expanding the lattice with larger cations to encourage better overall reduction and increased electron density, or by integrating cations of higher charge to then accommodate increased electron density [18], [19], [20], [21]. However, few of these works examined the structural changes brought on by the substitutional cations, and so far, the effects on the oxidation behavior remain unknown. There remains a gap in understanding between how the cation substitutions alter the structure of mayenite and how certain structural changes alter the material properties, particularly the thermal stability and electronic state. The current work aims to (1) investigate the effects of cation

substitutions of both the Ca and Al sites in the mayenite framework on the lattice structure, and (2) connect the structural changes to the electrical conductivity and oxidation behavior. Moreover, the concept of dual substitution, or substituting both the Ca and Al sites simultaneously, is investigated to verify if a combination of increased electrical conductivity and improved oxidation resistance can be achieved.

3.2 Materials and Methods

3.2.1 Cation Selection

One of the goals of this chapter is to elucidate the effect of cation size on the mayenite crystal structure. Therefore, both a substitutional cation with a larger ionic radius and one with a smaller ionic radius than the solvent cations (i.e., Ca^{2+} and Al^{3+}) were selected for the calcium and aluminum sites, respectively. Some researchers investigated substitute cations that alter the charge of the solvent cation site. For example, Bertoni et al. experimented with an Si^{4+} substitute for the Al^{3+} site in order to allow the additional charge to be balanced out by additional free oxygen cations [22]. In contrast, the present work does not attempt to alter the charge state of the site, and thus, the substitute cations with the same valence with the solvent ions were chosen when considering the respective precursor. To select suitable cationic substitutes, the trade-off between a sufficiently large difference in ionic radius (to induce perceptible change in lattice structure) and the solubility limit (the threshold amount of substitutional solutes that can be added without causing phase change or forming new second phase) must be considered. The latter point leans heavily on the traditional knowledge of the Hume-Rothery rules and the Goldschmidt rules, particularly the size effect [23], [24]. In general, three regimes are specified according to the difference in the ionic radius between the solvent atom and the solute atom.

Less than a 15% difference in the radii generally results in significant substitution. A difference between 15% and 30% generally results in limited ability to substitute. Greater than 30% difference makes substitution difficult. However, the immense empty cage space in the mayenite structure can accommodate larger substitutional ions than the lattice points, particularly when the substitution is at a small atomic percent (at%). This has already been demonstrated in practice by Schwarz et al., whose work showed the feasibility of using substitutional atoms with over 40% size difference when they substituted Ni^{2+} at 0.26 at% at the aluminum site [25]. With all of these considerations described above, Table 3.03 provides the information of the substitutional cations selected in this study, with difference in ionic radius noted.

Table 3.03 Cation Substitute Selection. Radii from Shannon Database of Ionic Radii used.

Solute Cation	**Solvent Cation**	**Difference in Ionic Radius**
Mg	Ca	-28%
Ba	Ca	35%
B	Al	-71/-49.5% (site dependent)
Mn	Al	14.5%

3.2.2 Powder Processing and Sintering

The cation substituted mayenite powder was processed via powder solid state reactions. For pure mayenite powder, the precursor powders calcium carbonate and alumina are mixed in a 12:7 ratio and reacted according to EQ(1)

$$12SrCO_3 + 7Al_2O_3 \rightarrow Ca_{12}Al_{14}O_{33} + 12CO_2 \qquad \text{EQ(1)}$$

Cation substituted powders were produced in a similar fashion but with the corresponding precursors substituted for calcium carbonate and alumina. Precursor powders were mixed to produce compounds $Ca_{12-x}Z_xAl_{14}O_{33}$ or $Ca_{12}Al_{14-x}Z_xO_{33}$ where Z is the substitutional cation and x=(0.05, 0.1, 0.2, 0.4). Dual substitution was done at two levels for two separate pairs of

substitutional atoms. The first pair of atoms was a magnesium (Mg) substitute for calcium and a manganese (Mn) substitute for aluminum. The second pair was a barium (Ba) substitute for calcium and a boron (B) substitute for aluminum. The pairs were selected in such a way that lattice distortion resulting from the increase in size on one atom could possibly be balanced by the decrease in size at another site. First, a sample with equivalently low dose for each substitution was synthesized (x=0.1 for both substitutes). Subsequently, prescribing a higher dose for the substitute predicted to decrease the lattice parameter (x=0.1 for the large substitute and x=0.2 for the smaller substitute). This would allow for an overall contraction of the lattice to be observed while the structure still experienced some of the influence of the larger cation substitute on the electronic structure.

Starting powders are $CaCO_3$ (≥ 99.9%, Sigma Aldrich), Al_2O_3 (≥99.9%, Sigma Aldrich), MgO (≥ 99.9%, Sigma Aldrich), $BaCO_3$ (≥99%, Oakwood Chemical), B_2O_3 (≥99.98%, Sigma Aldrich), and MnO (≥99%, Sigma Aldrich). These are mixed in the proper stoichiometric ratio and milled in a planetary ball mill (Across International PQ-N4) with a ball to powder weight ratio of 10:1 at 400 RPM using a 5-minute-on and 10-minute-off duty cycle to minimize frictional heating in the alumina jars. Mixed precursors are loaded into alumina crucibles for powder solid state reaction in air at 1300 °C for 12hrs. After the reaction, the mayenite powders are ground in agate ball mill jars for an additional two hours and then loaded into a 28mm diameter graphite tooling set used in the SPS. Within the tooling set, the powder is surrounded on the circumference and on top and bottom with titanium metal foil to facilitate the replacement of free oxygens with electrons and graphite foils surround the titanium to curb effects of contact resistance with the tooling. C12A7 powders are then heated to 1250℃ in SPS vacuum chamber at a rate of 100℃/min with a small uniaxial load (15MPa) and a ten-minute hold.

Table 3.04 Mayenite Sample IDs

Sample ID	Notes
C12A7P	Pure Mayenite Powder
C12A7e$^-$	Pure Mayenite Electride Disc
0.xZ-C12A7P	Cation Substituted Mayenite Powder (Z is solute atom, x is substitution level)
0.xZ-C12A7e$^-$	Cation Substituted Mayenite Electride Disc (Z is solute atom, x is substitution level)
(0.xW+0.yZ)-C12A7P	Dual Cation Substituted Mayenite Powder (W,Z are solute atoms; x,y are substitution levels)
(0.xW+0.yZ)-C12A7e$^-$	Dual Cation Substituted Mayenite Electride Disc (W,Z are solute atoms; x,y are substitution levels)

3.2.3 Phase Identification and Rietveld Modeling

The crystal structures present in each sample were characterized via powder X-ray diffraction (XRD) using a Bruker D8 Discover DaVinci Powder X-ray Diffractometer. Scans were taken in a 2θ range of 15°-120° using kα radiation (k=1.5406Å) with a step size of 0.01°. Phase composition is analyzed matching patterns to those found on the International Center for Diffraction Data (ICDD) database. Particular attention was paid to any secondary calcium aluminate phases as well as the precursor powders. Lattice parameter and structural data were calculated by Rietveld refinement using TOPAS6 software. A small amount of silicon (≤5wt%) is added to the powder. The main peak from the silicon is fit first to give a better correction to the sample height and provide more confidence in lattice parameter calculations. The mayenite structure is given below in Table 3.05.

Table 3.05 Mayenite Structure and Rietveld Refinement Parameters. Lattice parameters: a~11.99Å, space group $I\bar{4}3d$

Site	**Wyckoff**	**x**	**y**	**z**	**Occ.**	**B_{iso}**
Ca1	24d	Ca1x	0	0.25	Ca1Occ	Ca1B
Ca2	24d	Ca2x	0	0.25	Ca2Occ	Ca2B
Al1	16c	Al1x	Al1x	Al1x	1	Al1B
Al2	12b	0.875	0	0.25	1	Al2B
O1	48e	O1x	O1y	O1z	1	O1B
O2	16c	O2x	O2x	O2x	1	O2B
O3	48e	O3x	O3y	O3z	O3Occ	(O1B+O2B)/2

Any parameters given by a variable name rather than a number (Ca1, O3Occ, etc.) are variable refined in the model. Ca2 is a displaced calcium drawn toward the center of the cage by the free oxygen anion. It still occupies the same site as Ca1, so their occupancies are restricted to adding to one to give the structure full calcium occupancy. The free oxygen (O3) has an upper bound on its occupancy corresponding to the theoretical maximum of two anions per twelve cages (with 48 possible sites that yields 2/48=0.04167). Isotropic displacement parameters are employed as the resolution of the data does not provide enough reliability to use anisotropic parameters. The O3 thermal parameter is set to an average of the O1 and O2 parameters due to the weak signal from O3 as has been previously established. First refined were the background, lattice parameters, and peak shape parameters. This was followed by the positional parameters and then isotropic displacement parameters. After all of these were fit to an acceptable degree the occupancies were refined. Attempts to include the solute atoms (modeled as sitting on the same site as the solvent atoms) resulted in unacceptable error in the occupancy of the solute atoms (standard deviation in these refined values exceed the value itself). Therefore, solute atoms were not included in the models.

3.2.4 Thermal Analysis

Small samples (20-30mg) are cut and polished for thermal analysis. Thermogravimetric analysis (SEIKO) is performed using Pt pans in an ambient atmosphere (pO_2 ~ 0.21atm) using a heating rate of 10°C/min. Scans were performed between 50°C and 1050°C. Oxidation point is calculated by examining the second derivative of polynomial fit to the mass change data. Rate of oxidation is reported as percent mass change over time to correct for different sizes of samples.

3.2.5 Electrical Conductivity Testing

Sintered samples were cut into rectangular bars and polished for analysis. Copper leads are attached to the bar samples using a silver epoxy (EpoTek), as shown in Figure 3.02, to have four-point contacts. Electrical resistance is measured as a function of temperature using a four-probe set-up in a Quantum Design Physical Property Measurement System (PPMS). Resistance is calculated from measured voltage to reach input current given to PPMS system. Several input currents (0.1-100mA) are tested to maximize current without throwing AC current out of phase. Three specimens were tested for each level of substitute and the baseline materials. All specimens were tested at temperatures ranging from 25°C to 125 °C. Data were collected every ten degrees and every data point is an average of three measurements at each temperature point.

Figure 3.02 Electrical Conductivity PPMS Sample

3.3 Results

3.3.1 Baseline Materials: Mayenite and Mayenite Electride without Substitutions

3.3.1.1 Mayenite Powder

To highlight the effects resulting from cation substitutions, mayenite and mayenite electride without substitutions must be studied first as the baseline materials. Of particular concern when it comes to oxy-mayenite powder (**C12A7P**) is the phase composition and structural information that can be extracted from XRD data. Figure 3.03 shows that the powder contains 87.7wt% (weight percent) pure mayenite with a small amount of other calcium aluminate phases such as $CaO•Al_2O_3$ (CA). After fitting a calculated curve using Rietveld refinement, the structural parameters are extracted and provided in Table 3.06.

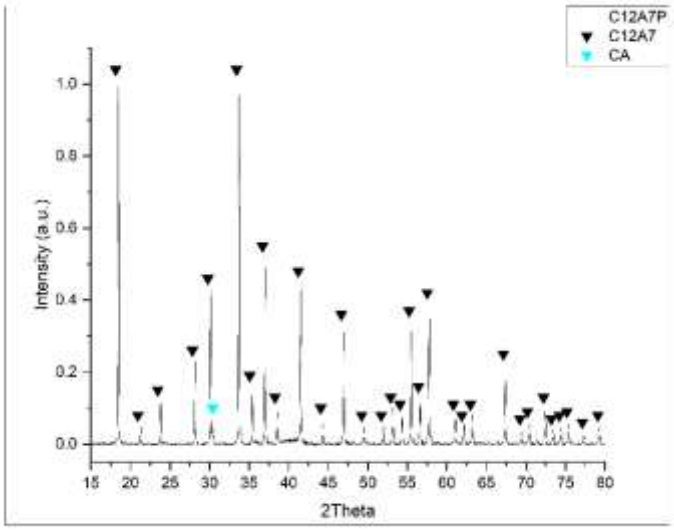

Figure 3.03 XRD Pattern of Pure Mayenite Powder (C12A7P)

The model has an R_{wp} factor of 4.886% and the parameters are similar to those reported in literature. The R-factor reflects the discrepancy between the calculated diffraction profile and the observed profile and thus lower R-factor reflects a better fit. The calculated model also shows the material to have a lattice parameter of 11.98676(2)Å where the number in parentheses represents the standard deviation (uncertainty) in the last one or two decimal places. This value of lattice parameter is in agreement with the typically reported value of 11.99Å. The occupancy of the displaced Ca2 site (Figure 3.01) is 0.225 which is slightly above the theoretical maximum

(0.167). It is more appropriate to interpret these occupancy factors from a qualitative standpoint, as they depend on the thermal parameters that are chosen, which makes quantitative interpretation less reliable. However, the occupancy for Ca2 site is still in the range of previously reported parameters. The Ca2 occupancy factor agrees with the occupancy factor for the O3 site, which shows that the "center" of the cage is fully occupied. Those results suggest that one of every six cages has an O^{2-} anion near the center. These encaged anions are responsible for the displacement of the Ca1 cation toward the center of the cage, which results in the Ca2 site occupation.

Table 3.06 Refined Model Parameters for C12A7P. Numbers in parentheses following refined values are standard uncertainty (deviation) in the decimal place prior. Lattice parameters: a=11.98676(2)Å, space group $I\bar{4}3d$

Site	**Wyckoff**	**x**	**y**	**z**	**Occ.**	**B_{iso}**
Ca1	24d	0.1382(5)	0	0.25	0.78(2)	0.70(6)
Ca2	24d	0.179(2)	0	0.25	0.22(2)	1.7(2)
Al1	16c	0.01816(10)	0.01816(10)	0.01816(10)	1	1.16(6)
Al2	12a	0.875	0	0.25	1	0.90(6)
O1	48e	0.0365(2)	0.4428(2)	0.1509(2)	1	0.93(6)
O2	16c	0.1853(2)	0.1853(2)	0.1853(2)	1	1.3(2)
O3	48e	0.364(7)	0.032(7)	0.26(2)	0.041(2)	1.13(7)

3.3.1.2 Mayenite Electride

A representative photo of pure mayenite electride samples(**C12A7e$^-$**) is inset in Figure 3.04. The XRD pattern shows that the electride sample has high phase purity (89.5%). The pattern looks identical to that of C12A7P, but slight shifts in peak positioning are present due to the increase of the lattice parameter (a = 11.996302(12)Å).

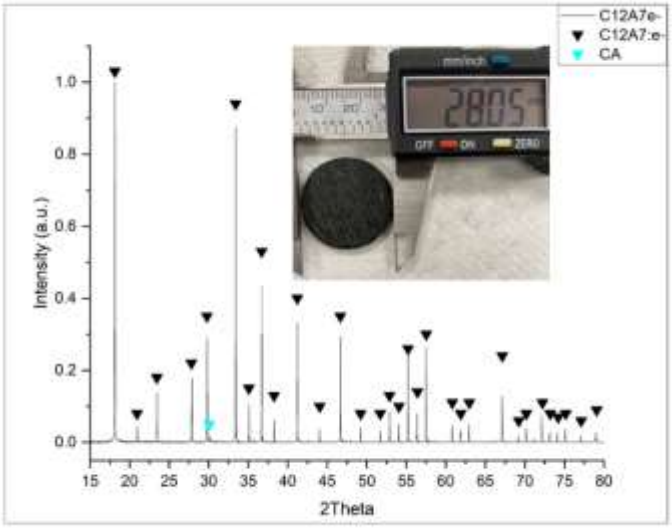

Figure 3.04 XRD Pattern of Pure Mayenite Electride ($C12A7e^-$)

As previously discussed, the replacement of oxygen anions with electron anions in the center of the cages allows the structure to relax, and as a result, the cages expand and give rise to a larger lattice parameter. Table 3.07 shows the results of the Rietveld refinement for $C12A7e^-$ (R_{wp}=5.966%), which provide evidence of the lattice structural change. The Ca2 site, which is displaced from the Ca1 site because of the oxygen anion, has a lower occupancy compared to the occupancy in C12A7P and the refined position suggests that it is positioned further from the center of the cage as compared to the position in C12A7P. The changed position is represented more accurately by the interatomic distance. In the case of C12A7P, the Ca2-center distance (2.339Å) is smaller than that for $C12A7e^-$ (2.423Å). This is an increase of 0.084Å when the mayenite is reduced to the mayenite electride. Other framework atom sites, such as Al1 and O1, experienced movement from the cage center by a similar magnitude of distance (0.013Å and 0.021Å, respectively). Both Ca1 and O2 sites were displaced away from the center as well, but with a distance less than 0.005Å.

Table 3.07 Refined Structural Parameters for C12A7e$^-$. Lattice parameters: a=11.996302(12)Å, space group $I\bar{4}3d$

Site	Wyckoff	x	y	z	Occ.	B_{iso}
Ca1	24d	0.1383(5)	0	0.25	0.81(3)	0.21(6)
Ca2	24d	0.173(3)	0	0.25	0.19(3)	1.5(3)
Al1	16c	0.01763(8)	0.01763(8)	0.01763(8)	1	0.59(4)
Al2	12a	0.875	0	0.25	1	0.56(5)
O1	48e	0.0349(2)	0.4435(2)	0.1521(2)	1	0.57(5)
O2	16c	0.1848(2)	0.1848(2)	0.1848(2)	1	1.20(11)
O3	48e	0.398(5)	0.035(4)	0.385(4)	0.040(3)	0.88(6)

3.3.2 Calcium Site Substitution

3.3.2.1 Magnesium

The XRD pattern of the x=0.2 level Mg substitute electride sample (**0.2Mg-C12A7e$^-$**) is shown in Figure 3.05. All diffraction patterns obtained from the substitute samples showed similarity in the presence of a small amount of secondary calcium aluminate phase. No peaks related to Mg-containing oxide phases were observed in the scans. The diffraction patterns of the CA and C3A phases are very similar, but given the calcium deficiency in these substituted samples, krotite (CA) is the more likely phase.

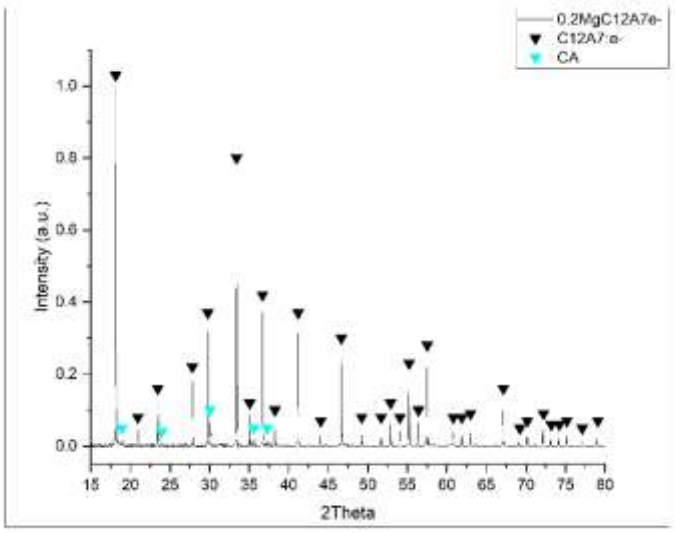

Figure 3.05 XRD Pattern of Mg Substituted Electride (0.2Mg-C12A7e$^-$)

Mayenite is a stoichiometric phase with 12:7 CaO to Al_2O_3 ratio in the calcium aluminate phase diagram. With an increasing level of Mg substitutes for the Ca site, the starting powders have a CaO:Al_2O_3 ratio straying from the 12:7 ratio toward 1:1, which discourages nucleation and growth of the C12A7 phase, and instead, a larger amount of krotite is formed. However, the relative amounts of the two phases, provided in Table 3.08, do not show a linear correlation to the level of Mg substitutes.

Table 3.08 Phase Composition (wt%) of Mg Substituted Mayenite Powder

Sample	**C12A7 wt%**	**CA wt%**
C12A7P	87.7	12.3
0.05Mg-C12A7P	95.3	4.7
0.1Mg-C12A7P	95.6	4.4
0.2Mg-C12A7P	85.7	14.3
0.4Mg-C12A7P	88.9	11.1

The lattice parameter of each sample is shown in Table 3.09 with standard uncertainty in parentheses. It is worth noting that the results were obtained from Mg-substitute C12A7 powder rather than the sintered bulk samples, because of the better reliability of sample height correction by using a small amount of cubic silicon powder for its relatively simple structure. There is little difference expected (<0.1%) in the lattice parameter between powder and bulk in this case as large differences are typically associated with nano sized powders. All four Mg substituted

samples show an increase of the lattice parameter compared to the nominally pure mayenite, as shown in Figure 3.06. The increase shows a linear correlation with the substitution level.

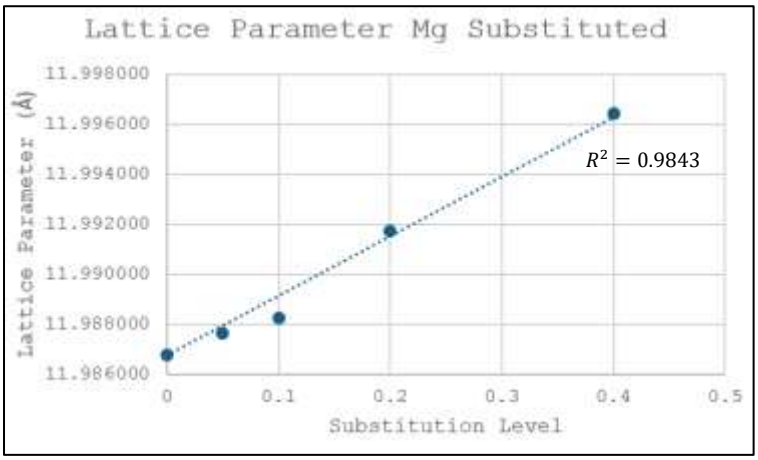

Figure 3.06 Lattice Parameters of Mg Substituted C12A7 Powders

Table 3.09 Lattice Parameters of Mg Substituted Mayenite Powder

Substitution Level	**Lattice Parameter (Å)**
x = 0.00	11.98677(2)
x = 0.05	11.98765(2)
x = 0.10	11.98824(2)
x = 0.20	11.99176(2)
x = 0.40	11.99642(3)

The structural parameters for 0.2Mg-C12A7P are given in Table 3.10. Each of the refinements for each substitution level powder achieved an R_{wp} factor of 6.2% or lower, indicating acceptable fit. The Rietveld modeling results suggest that all the powders have similar Ca1/Ca2 ratios to that for pure C12A7P and have full occupancy of the O3 site.

Table 3.10 Refined Structural Parameters for 0.2Mg-C12A7P. Lattice parameters: a=11.99176(2)Å, space group $I\bar{4}3d$

Site	Wyckoff	x	y	z	Occ.	B_{iso}
Ca1	24d	0.1376(5)	0	0.25	0.76(2)	0.29(6)
Ca2	24d	0.1751(17)	0	0.25	0.24(2)	1.32(19)
Al1	16c	0.01804(9)	0.01804(9)	0.01804(9)	1	0.84(5)
Al2	12a	0.875	0	0.25	1	0.53(5)
O1	48e	0.03686(16)	0.44275(15)	0.15086(18)	1	0.54(5)
O2	16c	0.1848(2)	0.1848(2)	0.1848(2)	1	0.95(12)
O3	48e	0.357(5)	-0.038(4)	0.264(8)	0.0416(19)	0.75(6)

Expansion of the lattice is evident based on the shift of the framework atoms away from the center of the cage according to the information in Table 3.11. As the Mg content increases from 0 to the 0.1 level, every framework ion, except for O2, moves away from the center of the cage, with the movement from the Ca sites being most stark. For 0.1Mg-C12A7P, the Ca1 and Ca2 sites shift away from the center of the cage by 0.012Å and 0.035Å, respectively. The Al1 and O1 atoms shift only by several thousandths of an angstrom. For 0.2Mg-C12A7P, the Ca1 and Ca2 atoms move in opposite directions. However, for 0.4Mg-C12A7P, they both have settled almost exactly back to the same position as the 0.1 level. For 0.2Mg-C12A7P and 0.4Mg-C12A7P, the Al1 and O2 atoms have a steady progression outward by several thousandths of an angstrom. The O1 atom has a slight retreat for 0.2Mg-C12A7P before moving outward by a hundredth of an angstrom for 0.4Mg-C12A7P.

Table 3.11 Changing Distance of Framework Atoms from Cage Center for Mg Substituted Mayenite Powder

Substitution Level	Ca1-center (Å)	Ca2-center (Å)	Al1-center (Å)	O1-center (Å)	O2-center (Å)
x = 0.0	2.838	2.339	5.105	6.786	3.272
x = 0.05	2.849	2.358	5.104	6.786	3.272
x = 0.1	2.850	2.374	5.106	6.788	3.272
x = 0.2	2.847	2.397	5.110	6.786	3.275
x = 0.4	2.849	2.375	5.113	6.796	3.277

Figure 3.07 shows the mass gain of the Mg substitute mayenite electride samples as a function of temperature. The C12A7e$^-$ and 0.4Mg-C12A7e$^-$ samples experience a slight decrease in mass before increasing which is attributed to evaporation of small amounts of water absorbed during processing of samples. The theoretical maximum mass gain for C12A7:e$^-$ is 1.17%, which is exceeded by 0.05Mg-C12A7e$^-$, 0.1Mg-C12A7e$^-$, and 0.2Mg-C12A7e$^-$ [11]. Several groups have reported results like this, and it can be attributed to higher mass oxygen radicals (O_2^-) integrating into the cages [11], [26]. Were the instrument capable of higher temperatures, it is likely the mass gain would drop down below this theoretical maximum as the higher mass radicals would be desorbed. Phase analysis of the sample post-heating was also conducted, and the result is shown in Figure 3.08.

It is clear from Figure 3.07 that the increasing levels of Mg result in an increase in the onset temperature of rapid oxidation of the material. The relevant data and the values of peak oxidation rate are provided in Table 3.12. The pure C12A7e$^-$ sample begins to rapidly oxidize at a temperature of 662.1°C. All the curves for the Mg-substitute samples flatten out and show rapid oxidation beginning at higher temperatures. TGA curves for 0.05Mg-C12A7e$^-$, 0.1Mg-C12A7e$^-$, and 0.2Mg-C12A7e$^-$ show rapid oxidation happening approximately at 783.7°C, 753.2°C, and 793.2°C, respectively. These correspond to an increase in rapid oxidation onset temperature of 121.6°C, 91.1°C, and 131.1°C, respectively for those Mg substitute samples, compared to the baseline material – pure mayenite electride. The sample with the highest level of substitution (0.4Mg-C12A7e$^-$) begins to rapidly oxidize at 813.5°C, delaying the onset of rapid oxidation by over 150°C. In addition, most of the samples only have a slight increase to the peak rate of oxidation. It is worth noting that these results are slightly affected by small variations in

surface area of the sample but still are compelling evidence for the positive effect of Mg substitution on the oxidation behavior.

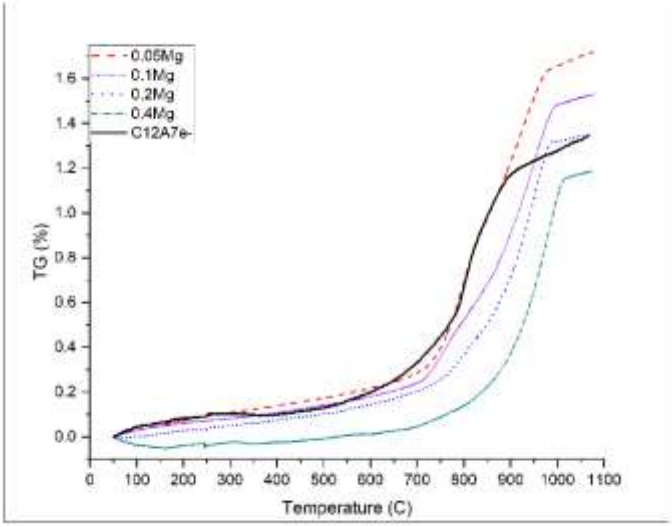

Figure 3.07 Increase in Onset of Rapid Oxidation of Mg Substituted Mayenite Electride

Table 3.12 TGA Data-points of Mg Substituted Mayenite Electride

Substitution Level	**Onset of Rapid Oxidation (°C)**	**Peak Oxidation Rate (%/min)**
x = 0.00	662.1	0.0783
x = 0.05	783.7	0.0687
x = 0.10	753.2	0.0580
x = 0.20	793.2	0.0819
x = 0.40	813.5	0.0876

After the thermal exposure during the TG analysis, all samples maintained mechanical integrity with no evidence of any cracking or ablation when examined under optical microscopy. As seen in the XRD scan of the post thermal analysis sample (Figure 3.08) there is no appearance of any magnesium oxide phases nor an increase in number/intensity for secondary calcium aluminate peaks compared to the diffraction patterns of the samples before TGA. There is some remaining black coloration indicative of the increased ability of the Mg substituted sample to resist oxidation.

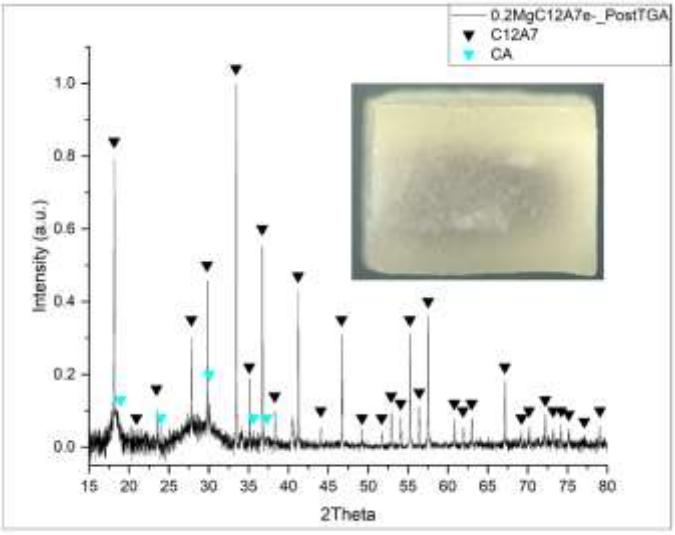

Figure 3.08 Post-TGA XRD Pattern of Mg Substituted Electride (0.2Mg-C12A7e$^-$)

The results of electrical conductivity measurements are provided in Figure 3.09. The pure electride sample has a room temperature conductivity of 22.8S/cm. This is a low conductivity compared to some other works investigating polycrystalline mayenite electride. It should be noted that the porosity (~10%) present in the samples as well as the fine grains (i.e. high volume of grain boundaries) in the bulk due to the rapid sintering in SPS contributed to decrease the conductivity compared to other studies. It is also known that mechanically grinding and polishing of the sample surface leads to oxidized cages, which also decreases the electrical conductivity. All samples display a slight increase in electrical conductivity as temperature increases, which is typical of semiconductors. The 0.05Mg-C12A7e$^-$ conductivity tailed off slightly at higher temperature, but these data points are related to the AC current falling slightly out of phase. Therefore, the data points for temperature 105°C-125°C are less reliable. A similar phenomenon is observed for the first two data points (25°C-35°C) collected for the 0.1Mg-C12A7e$^-$ sample as well as the first data point for the pure electride sample (25°C). All but the 0.05Mg-C12A7e$^-$ sample display decreased conductivities compared to pure electride. The 0.05Mg-C12A7e$^-$ sample has an average room temperature conductivity of 137.0S/cm. In

contrast, 0.1Mg-C12A7e$^-$, 0.2Mg-C12A7e$^-$, and 0.4Mg-C12A7e$^-$ samples all had room temperature conductivities two orders of magnitude lower than the pure electride sample, at 2.4S/cm, 8.0S/cm, and 2.6S/cm respectively. The change in the electrical conductivities is attributed to the lattice structural change, which will be discussed in Section 3.4.

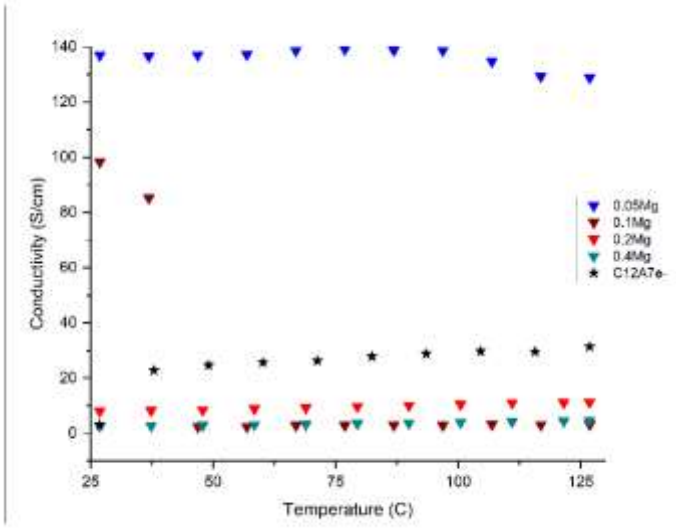

Figure 3.09 Electrical Conductivity of Mg Substituted Mayenite Electride

3.3.2.2 Barium

The Ba substituted powder and electride discs are mostly phase pure as shown in the XRD pattern in Figure 3.10. The Ba substitute did induce a peak which previously had not been observed in the XRD of the mayenite powder, but this peak could not be matched to any barium related phase and was one of the prominent peaks of a $Ca_3Al_2O_6$ (C3A) pattern. Furthermore, Figure 3.10 (lower) shows that the electride disc has lost most of the secondary phase peaks during sintering including this previously unobserved peak. There is no noticeable correlation between phase purity and the Ba substitution and in fact most of the Ba substituted samples have

higher weight percent mayenite than the C12A7P sample as seen in Table 3.13. However, the 0.4Ba-C12A7P stands out in this regard as it is comprised more of secondary calcium aluminate phases (in particular C3A) than mayenite. This is more evident when observing the XRD pattern for the 0.4Ba-C12A7P sample where the most prominent peak is that of C3A (Figure 3.11). For this reason, there was no attempt to sinter 0.4Ba-C12A7P into a reduced disc.

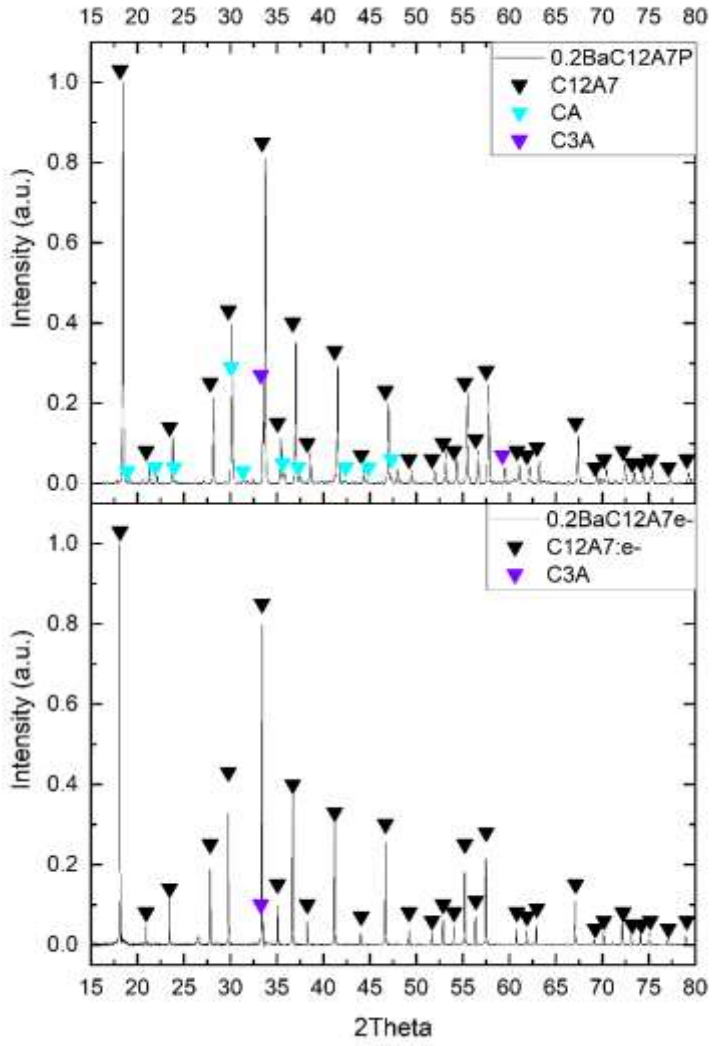

Figure 3.10 XRD Patterns of Ba Substituted Mayenite Powder (upper) and Ba Substituted Mayenite Electride (lower)

Table 3.13 Phase Composition (wt%) of Ba Substituted Mayenite Powder

Sample	C12A7 wt%	CA/C3A wt%
C12A7P	87.7	12.3
0.05Ba-C12A7P	93.2	6.8
0.1Ba-C12A7P	92.7	7.3
0.2Ba-C12A7P	93.1	6.9
0.4Ba-C12A7P	32.6	67.4

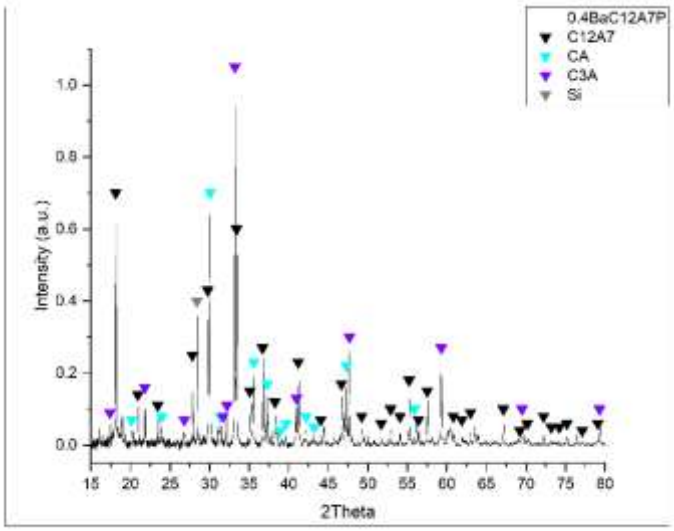

Figure 3.11 Secondary Calcium Aluminates Dominate XRD Pattern of 0.4Ba-C12A7P

The Ba substitute samples all have a lattice parameter smaller than that of C12A7P. The substituted samples (aside from the 0.4Ba-C12A7P) are shown to have increases to the parameter as substitution level increases.

Table 3.14 Lattice Parameters of Ba Substituted Mayenite Powder

Substitution Level	Lattice Parameter (Å)
x = 0.00	11.98677(2)
x = 0.05	11.98277(1)
x = 0.10	11.98322(2)
x = 0.20	11.98657(2)
x = 0.40	11.98187(9)

Table 3.15 Refined Structural Parameters for 0.2Ba-C12A7P. Lattice parameters: a=11.98657(2)Å, space group $I\bar{4}3d$

Site	Wyckoff	x	y	z	Occ.	B_{iso}
Ca1	24d	0.1397(5)	0	0.25	0.759(19)	0.75(7)
Ca2	24d	0.1824(17)	0	0.25	0.241(19)	1.1(2)
Al1	16c	0.01776(11)	0.01776(11)	0.01776(11)	1	1.13(7)
Al2	12a	0.875	0	0.25	1	0.94(7)
O1	48e	0.0360(2)	0.44414(19)	0.1505(2)	1	1.12(7)
O2	16c	0.1860(3)	0.1860(3)	0.1860(3)	1	1.59(15)
O3	48e	0.372(19)	0.023(17)	0.25(7)	0.042(2)	1.36(8)

There is movement of some of the framework atoms (Al1, O1) away from the center of the cage matching the expansion from 0.05Ba-C12A7P to 0.2Ba-C12A7P but these are smaller movements than those of Ca1 and Ca2 as seen in Table 3.15 and Table 3.16. The Ca1 and Ca2 movement toward the center is on the scale of hundredths of angstroms compared to the thousandths for the other framework atoms.

Table 3.16 Changing Distance of Framework Atoms from Cage Center for Ba Substituted Mayenite Powder

Substitution Level	Ca1-center (Å)	Ca2-center (Å)	Al1-center (Å)	O1-center (Å)	O2-center (Å)
x = 0.0	2.838	2.339	5.105	6.786	3.272
x = 0.05	2.826	2.361	5.107	6.788	3.270
x = 0.1	2.818	2.318	5.105	6.792	3.270
x = 0.2	2.820	2.309	5.112	6.803	3.270
x = 0.4	2.824	2.241	5.120	6.823	3.263

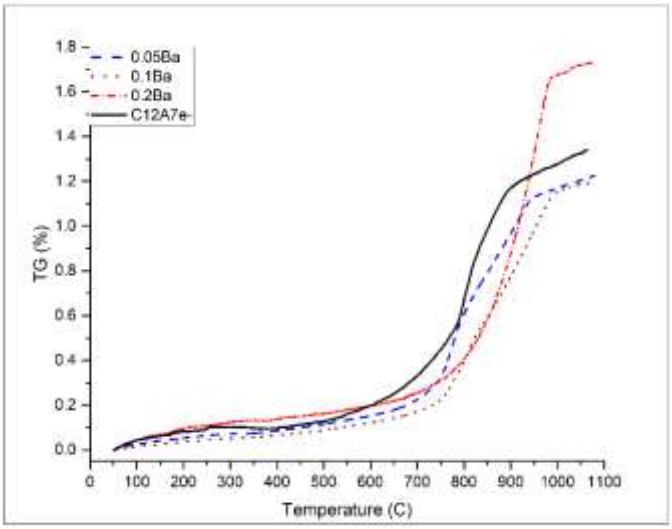

Figure 3.12 Oxidation and Mass Gain of Ba Substituted Mayenite Electride

Observed in Figure 3.12 and Table 3.17 there are increases in onset temperature of rapid oxidation comparable to those observed from the Mg substitution. There is also less variance in the net mass gain amongst the samples though the 0.2Ba-C12A7e$^-$ sample does exceed the theoretical maximum.

Table 3.17 TGA Data-points of Ba Substituted Mayenite Electride

Substitution Level	**Onset of Rapid Oxidation (°C)**	**Peak Oxidation Rate (%/min)**
x = 0.00	662.1	0.0783
x = 0.05	752.1	0.0646
x = 0.10	773.6	0.0448
x = 0.20	789.8	0.1048

As seen in Figure 3.13 all of the Ba substituted samples have increased electrical conductivity compared to the pure electride. All of the samples have a stark increase in their conductivity compared to the pure electride, though the 0.1 level sample does tail off at higher temperatures. The low dose sample (0.05Ba-C12A7e$^-$) has the highest room temperature conductivity at 56.8S/cm followed by the 0.2Ba-C12A7e$^-$ and the 0.1Ba-C12A7e$^-$ levels at 36.3 and 26.0S/cm respectively.

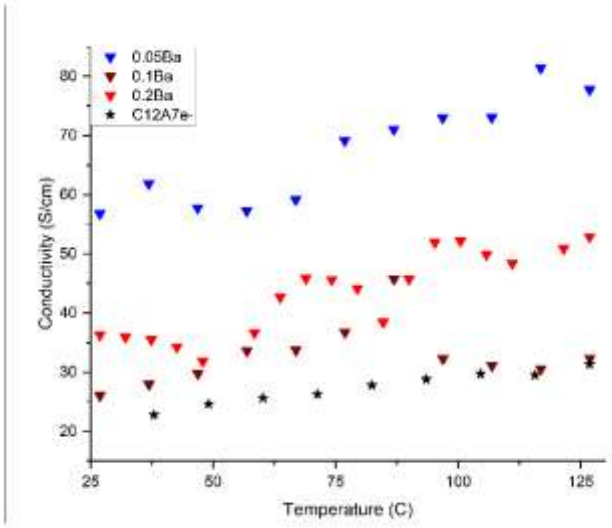

Figure 3.13 Electrical Conductivity of Ba Substituted Mayenite Electride

3.3.3 Aluminum Site Substitution

3.3.3.1 Boron

The XRD results for sample **0.1B-C12A7P** (upper) and **0.1B-C12A7e$^-$** (lower) are shown in Figure 3.14. The data shows that the B substituted samples have significant variation in phase composition as compared to the Mg substituted samples. The diffraction patterns reveal the presence of both C12A7 and CA phases. The B substituted samples do not exhibit a clear linear correlation between the substitution level and the weight percentage of the CA phase. Both the 0.05B-C12A7P and 0.4B-C12A7P samples have much higher CA content than the other B substituted samples, as shown in Table 3.17.

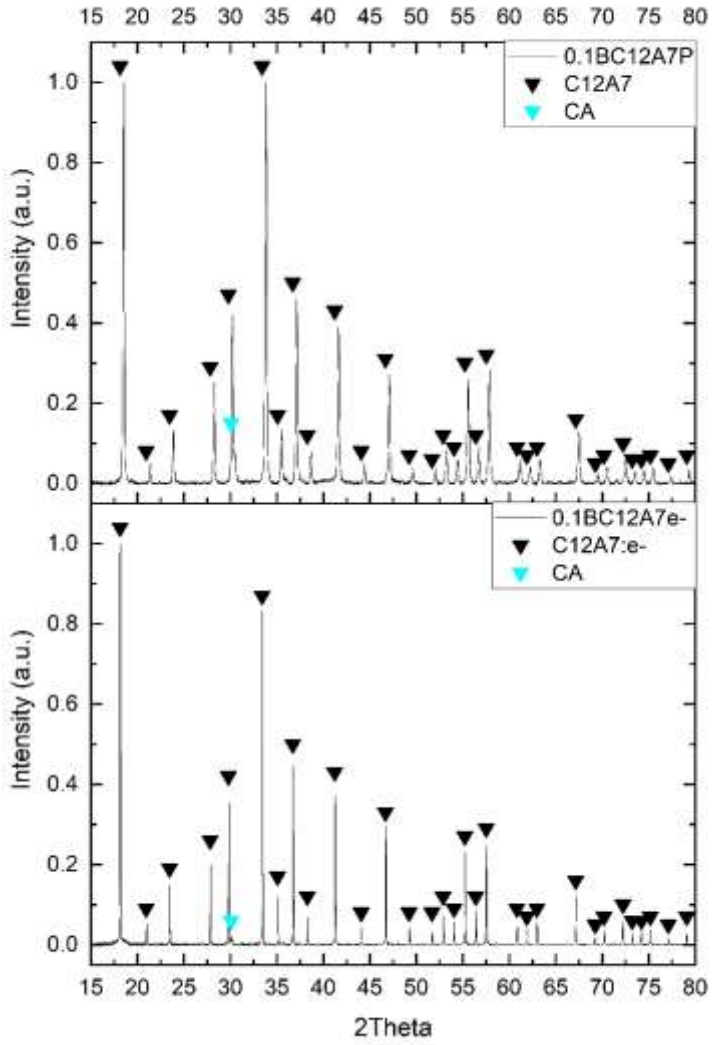

Figure 3.14 XRD Patterns of B Substituted Mayenite Powder (upper) and B Substituted Mayenite Electride (lower)

Table 3.18 Phase Composition (wt%) of B Substituted Mayenite Powder

Sample	C12A7 wt%	CA wt%
C12A7P	87.7	12.3
0.05B-C12A7P	83.3	16.7
0.1B-C12A7P	95.4	4.6
0.2B-C12A7P	92.9	7.1
0.4B-C12A7P	80.8	19.3

The lattice parameters of the boron-substituted samples are smaller than that of C12A7P but there is an increasing trend with B content. This data would indicate that the B substitute is behaving similarly to the Mg substitute.

Table 3.19 Lattice Parameters of B Substituted Mayenite Powder

Substitution Level	Lattice Parameter (Å)
x = 0.00	11.98677(2)
x = 0.05	11.98357(5)
x = 0.10	11.98538(3)
x = 0.20	11.98604(3)
x = 0.40	11.98782(3)

The effect of B substitution on the atomic positioning within the mayenite structure is notable, particularly in the shifts observed in the framework atoms. As shown in Table 3.20, the introduction of B leads to nuanced changes in the positions of the Ca, Al, and O atoms. Initially, with a substitution level of 0.05, the lattice contracts compared to C12A7P, as indicated by a minor decrease in the lattice parameter. This contraction corresponds with the movement of framework atoms closer to the center of the cage. For instance, the Ca1 and Ca2 atoms shift inward by 0.043 and 0.11 angstroms respectively. This is not the case with Al1 site where B is predicted to go. This site experiences an outward expansion. However, as the substitution level increases to 0.1, the Ca1 atom moves outward by 0.031 angstroms, while the Ca2 atom makes a large jump backwards by 0.064 angstroms. The Al1 atom meanwhile begins moving toward the center of the cage by several thousandths of angstroms. At the 0.4 substitution level movement is more pronounced and outward. The Ca1 and Ca2 atoms shift the most (0.014Å and 0.049Å respectively), indicating a substantial expansion of the lattice. The Al1 and O2 atoms stay in place while the O1 atom shifts outward by 0.007 angstroms.

Table 3.20 Refined Structural Parameters for 0.2B-C12A7P. Lattice parameters: a=11.98604(3)Å, space group $I\bar{4}3d$

Site	Wyckoff	x	y	z	Occ.	B_{iso}
Ca1	24d	0.1397(5)	0	0.25	0.809(19)	1.06(7)
Ca2	24d	0.184(2)	0	0.25	0.191(19)	1.3(3)
Al1	16c	0.01828(12)	0.01828(12)	0.01828(12)	1	1.37(8)
Al2	12a	0.875	0	0.25	1	1.16(8)
O1	48e	0.0363(2)	0.4425(2)	0.1512(3)	1	1.63(8)
O2	16c	0.1851(3)	0.1851(3)	0.1851(3)	1	1.91(18)
O3	48e	0.388(8)	0.00(4)	0.271(9)	0.0416(19)	1.77(10)

Table 3.21 Changing Distance of Framework Atoms from Cage Center for B Substituted Mayenite Powder

Substitution Level	Ca1-center (Å)	Ca2-center (Å)	Al1-center (Å)	O1-center (Å)	O2-center (Å)
x = 0.0	2.838	2.339	5.105	6.786	3.272
x = 0.05	2.795	2.229	5.111	6.787	3.269
x = 0.1	2.819	2.277	5.106	6.790	3.270
x = 0.2	2.820	2.289	5.103	6.783	3.272
x = 0.4	2.834	2.338	5.103	6.790	3.272

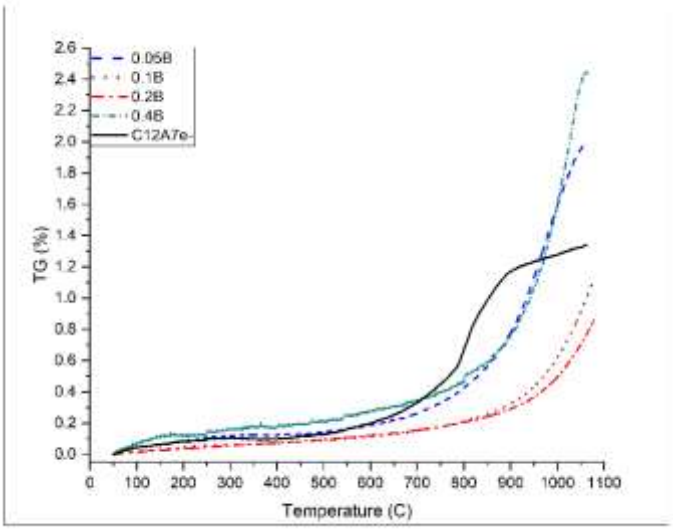

Figure 3.15 Increase to Onset of Rapid Oxidation for B Substituted Mayenite Electride

The B substitute samples in Figure 3.15 all have significant increase to the onset of rapid oxidation temperature. The 0.2B-C12A7e$^-$ sample shows the most significant change to the mass gain pattern and does not even hit 1% mass gain at maximum temperature. Note that these

samples (particularly 0.1B-C12A7e$^-$ and 0.2BC12A7e$^-$) did have the tailing off trend in mass gain, further demonstrating the significant improvement in stability.

Table 3.22 TGA Data-points of B Substituted Mayenite Electride

Substitution Level	Onset of Rapid Oxidation (°C)	Peak Oxidation Rate (%/min)
x = 0.00	662.1	0.0783
x = 0.05	821.6	0.0929
x = 0.10	906.9	0.0755
x = 0.20	911.5	0.0559
x = 0.40	787.7	0.0163

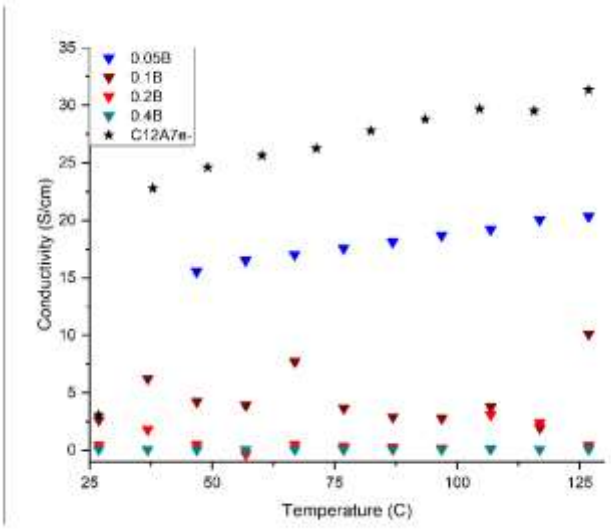

Figure 3.16 Decreased Electrical Conductivity of B Substituted Mayenite Electride

At room temperature, the electrical conductivity of boron-substituted samples varies significantly with the level of substitution but for every sample it decreases (Figure 3.16). The pure C12A7e$^-$ sample exhibits a conductivity of 22.8S/cm. For the 0.05B-C12A7e$^-$ sample, the conductivity decreases to 15.3S/cm, indicating a slight degradation to electrical performance. As the B substitution level rises to 0.1, the conductivity decreases to 2.5S/cm, reflecting a reduction in electrical efficiency. This trend continues with higher substitution levels; for 0.2B-C12A7e$^-$ and 0.4C12A7e$^-$, the conductivities drop further to 0.15S/cm and 0.1S/cm, respectively.

3.3.3.2 Manganese

The Mn substitution results in a distinct set of structural and compositional changes compared to B substitutions. The phase analysis indicates the presence of a $CaMnO_3$ phase at higher substitution levels, specifically in 0.2Mn-C12A7P and 0.4Mn-C12A7P as shown in Figure 3.17. The increasing weight percentage of the CA phase and the appearance of $CaMnO_3$ suggest that Mn incorporation leads to significant phase evolution during the powder solid state reaction, as shown in Table 3.23.

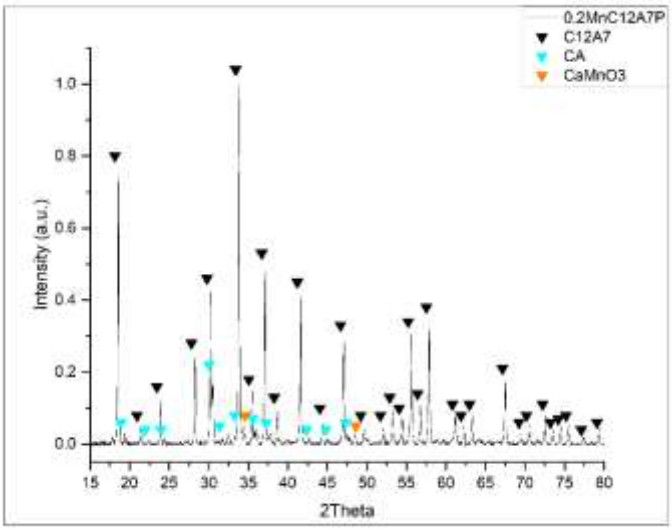

Figure 3.17 Appearance of Mn Based Secondary Phase in XRD Pattern of Mn Substituted Mayenite Powder

Table 3.23 Phase Composition (wt%) of Mn Substituted Mayenite Powder

Sample	**C12A7 wt%**	**CA wt%**	**$CaMnO_3$ wt%**
C12A7P	87.7	12.3	N/A
0.05Mn-C12A7P	95.4	4.6	N/A
0.1Mn-C12A7P	94.3	5.7	N/A
0.2Mn-C12A7P	83.0	15.4	1.6
0.4Mn-C12A7P	75.8	17.9	6.3

The lattice parameters of the manganese-substituted samples decreased with increasing substitution level except for Sample 0.4Mn-C12A7e^-, as shown in Table 3.24. For example, the

lattice parameter decreases from 11.9868Å (without Mn substitution) to 11.9592Å when the Mn substitution level increased to x=0.20.

Table 3.24 Lattice Parameters of Mn Substituted Mayenite Powder

Substitution Level	Lattice Parameter (Å)
x = 0.00	11.98677(2)
x = 0.05	11.97987(2)
x = 0.10	11.97888(2)
x = 0.20	11.95917(12)
x = 0.40	11.98143(5)

Mn substitution introduces even more pronounced changes in atomic positioning compared to B. The decrease in lattice parameter suggests a contraction of the crystal lattice. This lattice contraction is also reflected in the inward shifts of the framework atoms, particularly at higher substitution levels. At a substitution level of 0.05, the Ca1 atom shifts inward by 0.038 angstroms, and the Ca2 atom by 0.047 angstroms. This trend continues for 0.1Mn-C12A7P but to a smaller degree, where the Ca1 and Ca2 atoms shift inward by 0.002Å and 0.003Å respectively. The Al1 shifts outward at these substitution levels but only by a few thousandths of an angstrom. The O1 atom moves outward then inward in small movements while the O2 atom makes small movements inward. As the substitution level increases to 0.2, the Ca1 atom reverses course by 0.006 angstroms while the Ca2 atom movement becomes even more significant, shifting inward 0.016 angstroms. Interestingly, at the 0.4 substitution level, the Ca1 and Ca2 atoms experience a slightly outward shift of 0.001 and 0.016 angstroms, respectively, suggesting a minor relaxation of the lattice. The O1 atoms follow a similar pattern to the Ca2 atom shifting inward for sample 0.2Mn-C12A7P; while the O1 atoms in the for 0.4Mn-C12A7P sample moved outward significantly.

Table 3.25 Refined Structural Parameters for 0.2Mn-C12A7P. Lattice parameters: a=11.95917(12)Å, space group $I\bar{4}3d$

Site	Wyckoff	x	y	z	Occ.	B_{iso}
Ca1	24d	0.1405(9)	0	0.25	0.81(3)	1.17(12)
Ca2	24d	0.185(4)	0	0.25	0.19(3)	0.9(6)
Al1	16c	0.0174(2)	0.0174(2)	0.0174(2)	1	1.40(14)
Al2	12a	0.875	0	0.25	1	1.72(15)
O1	48e	0.0395(4)	0.4446(4)	0.1477(5)	1	1.68(13)
O2	16c	0.1893(6)	0.1893(6)	0.1893(6)	1	2.2(3)
O3	48e	0.37(8)	-0.0(5)	0.23(3)	0.042(4)	1.93(18)

Table 3.26 Changing Distance of Framework Atoms from Cage Center for Mn Substituted Mayenite Powder

Substitution Level	Ca1-center (Å)	Ca2-center (Å)	Al1-center (Å)	O1-center (Å)	O2-center (Å)
x = 0.0	2.838	2.339	5.105	6.786	3.272
x = 0.05	2.800	2.292	5.107	6.790	3.268
x = 0.1	2.798	2.288	5.108	6.785	3.267
x = 0.2	2.804	2.272	5.106	6.772	3.253
x = 0.4	2.805	2.288	5.111	6.802	3.264

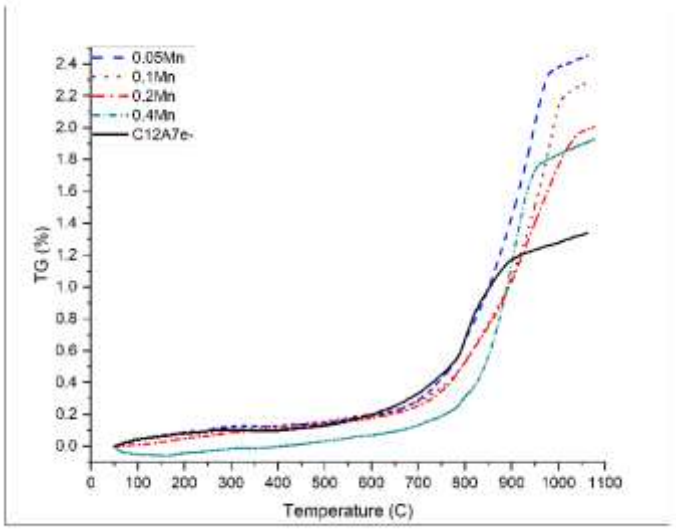

Figure 3.18 TGA Results of Mn Substituted Mayenite Electride

The Mn substitutes resulted in increases to the onset temperature of rapid oxidation, as seen in Figure 3.18. The effect of Mn substitutes on oxidation resistance is a mixing trend as demonstrated by the onset temperatures and peak oxidation rates provided in Table 3.27. Compared to the baseline sample without Mn substitutes, adding Mn increased both onset

temperatures and oxidation rates, while ideally improved oxidation resistance means an increase in onset temperature and decrease in oxidation rates. Mn has many more oxidation states compared to the previous substitutes discussed (Mg, Ba, B) and this could explain the distinct behavior of increase onset of rapid oxidation temperature combined with increased peak oxidation rate. While initially the smaller lattice size restricts oxidation possible progression of Mn to different oxidation states could allow for an expanded lattice and more rapid oxidation once the process starts.

Table 3.27 TGA Data-points of Mn Substituted Mayenite Electride

Substitution Level	**Onset of Rapid Oxidation (°C)**	**Peak Oxidation Rate (%/min)**
x = 0.00	662.1	0.0783
x = 0.05	789.8	0.1254
x = 0.10	834.8	0.1285
x = 0.20	776.7	0.0766
x = 0.40	884.7	0.1465

The Mn-substituted samples also have a notable variation in electrical conductivity at room temperature (Figure 3.19). The initial conductivity of the pure C12A7e$^-$ sample remains at 22.8S/cm. Substituting Mn at the 0.05 level slightly decreases the conductivity to 12.5S/cm. The 0.1Mn-C12A7e$^-$ sample exhibited an increased conductivity (116.4S/cm) compared to pure electride. However, it should be noted the degenerating of this as temperature increases is not the typical semiconductor behavior. As the Mn content increases to 0.4 level, conductivity decreases to 0.4S/cm.

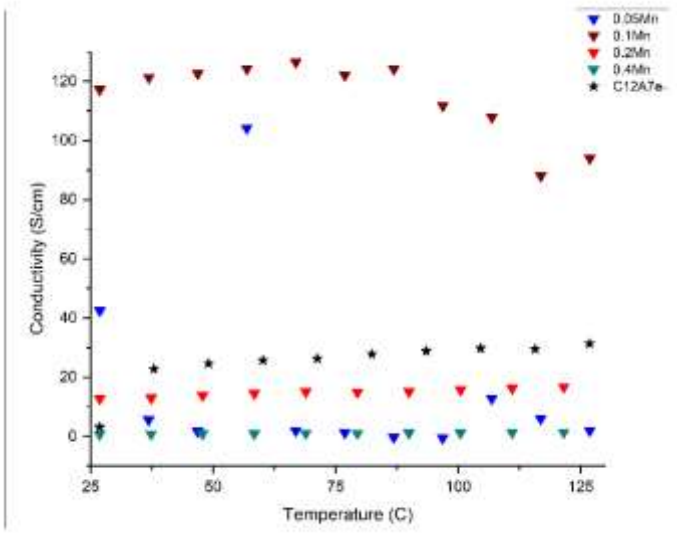

Figure 3.19 Electrical Conductivity of Mn Substituted Mayenite Electride

3.3.4 Dual Substitution

3.3.4.1 Magnesium and Manganese

The XRD results of the dual substitution powder samples, (**0.1Mg+0.1Mn)-C12A7P** and **(0.2Mg+0.1Mn)-C12A7P**, are shown in Figure 3.20. Both samples have the secondary CA phase, and the (0.1Mg+0.1Mn)-C12A7P sample has a much higher content of the secondary CA phase as shown in Table 3.28. No magnesium or manganese-related peaks were observed in the scan.

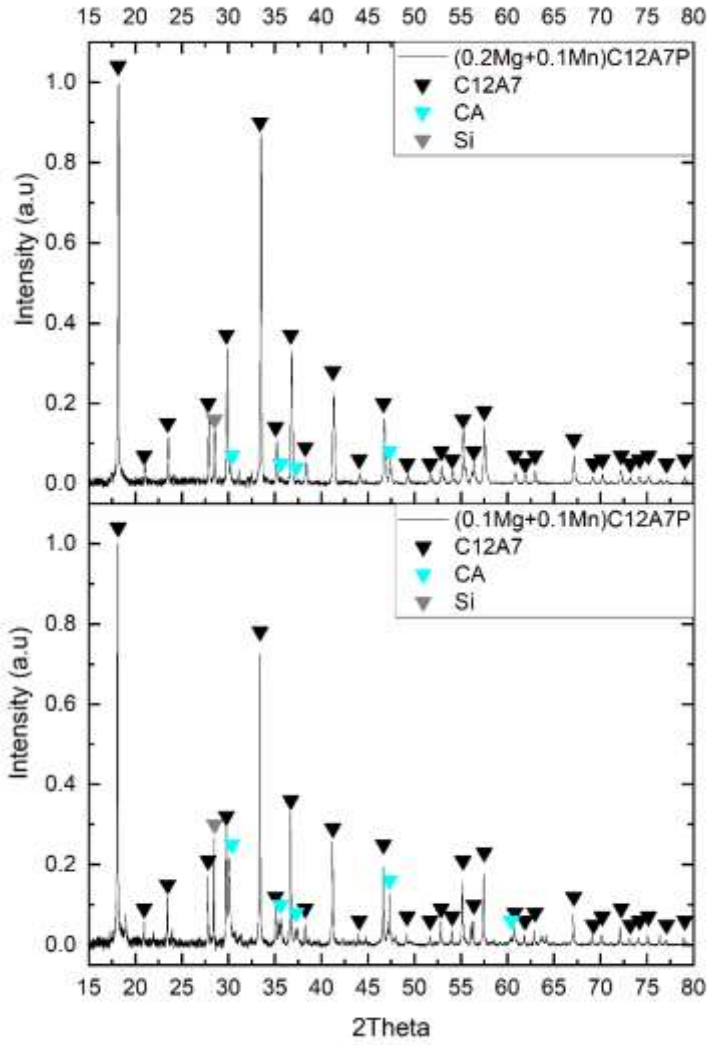

Figure 3.20 XRD Patterns of (Mg+Mn) Dual Substituted Mayenite Powder. (0.1Mg+0.1Mn)-C12A7P (lower) and (0.2Mg+0.1Mn)-C12A7P (upper).

Table 3.28 Phase Composition (wt%) of (Mg+Mn) Dual Substituted Mayenite Powder

Sample	C12A7 wt%	CA wt%
C12A7P	87.7	12.3
0.1Mg-C12A7P	95.6	4.4
0.1Mn-C12A7P	94.3	5.7
0.2Mg-C12A7P	85.7	14.3
(0.1Mg+0.1Mn)-C12A7P	58.7	41.3
(0.2Mg+0.1Mn)-C12A7P	94.4	5.6

The lattice parameter of each sample is shown in Table 3.29 with errors in parentheses. Included are previously discussed samples which had an individual substitution for comparison. In general, the (Mg+Mn) substitutions show similar patterns as the individually substituted samples, though the increased dose of Mg in (0.2Mg+0.1Mn)-C12A7P sample does result in a slight contraction in the parameter breaking the previous pattern.

Table 3.29 Lattice Parameters of (Mg+Mn) Dual Substituted Mayenite Powder Compared to Individually Substituted (Mg,Mn) Mayenite Powders

Substitution Level x is Mg and y is Mn	Lattice Parameter (Å)
x = 0.0 y = 0.0	11.98677(2)
x = 0.1 y = 0.0	11.98824(2)
x = 0.0 y = 0.1	11.98322(2)
x = 0.2 y = 0.0	11.99176(2)
x = 0.1 y = 0.1	11.99503(5)
x = 0.2 y = 0.1	11.98923(10)

The structural parameter tables for both samples are given below. The refinement for (0.1Mg+0.1Mn)-C12A7P sample has an R_{wp} factor of 4.7%. The refinement for the (0.2Mg+0.1Mn)-C12A7P sample has an R_{wp} factor of 7.9%. This refinement is accepted as the main source of error is from several small unmatched peaks.

Table 3.30 Refined Structural Parameters for (0.1Mg+0.1Mn)-C12A7P. Lattice parameters: a=11.99503(5)Å, space group $I\bar{4}3d$

Site	Wyckoff	x	y	z	Occ.	B_{iso}
Ca1	24d	0.1372(11)	0	0.25	0.80(5)	1.17(14)
Ca2	24d	0.1790(5)	0	0.25	0.20(5)	2.1(5)
Al1	16c	0.01790(16)	0.01815(18)	0.01815(18)	1	1.53(11)
Al2	12a	0.875	0	0.25	1	1.07(11)
O1	48e	0.0347(3)	0.4437(3)	0.1501(4)	1	1.86(11)
O2	16c	0.1838(4)	0.1838(4)	0.1838(4)	1	2.0(3)
O3	48e	0.433(7)	-0.055(7)	0.276(10)	0.042(3)	1.94(15)

Table 3.31 Refined Structural Parameters for (0.2Mg+0.1Mn)-C12A7P. Lattice parameters: a=11.98923(10)Å, space group $I\bar{4}3d$

Site	Wyckoff	x	y	z	Occ.	B_{iso}
Ca1	24d	0.1383(7)	0	0.25	0.80(3)	0.115(12)
Ca2	24d	0.185(3)	0	0.25	0.20(3)	2.5(6)
Al1	16c	0.01876(19)	0.01876(19)	0.01876(19)	1	1.57(13)
Al2	12a	0.875	0	0.25	1	2.03(14)
O1	48e	0.0379(4)	0.4453(3)	0.1498(4)	1	2.00(12)
O2	16c	0.1870(5)	0.1870(5)	0.1870(5)	1	1.8(3)
O3	48e	0.38(7)	0.02(8)	0.3(4)	0.042(4)	1.89(15)

Expansion of the lattice in the (0.1Mg+0.1Mn)-C12A7P sample is indicated by the shift of the framework atoms away from the center of the cage as shown in Table 3.32. These movements are all in the hundredths of angstroms except for the Al1 and O2 sites. Nevertheless, the modeling result of (0.2Mg+0.1Mn)-C12A7P shows different structural changes. Specifically, there is no movement from the Ca1 site in the model of (0.2Mg+0.1Mn)-C12A7P, while the Ca2 and Al1 sites shift toward the center of the cage by several hundredths of an angstrom. The O1 and O2 framework atoms also shift toward the cage center, but the O1 atoms are still expanded out from the center compared to the C12A7P structure.

Table 3.32 Changing Distance of Framework Atoms from Cage Center for (Mg+Mn) Dual Substituted Mayenite Powder Compared to the Individually Substituted (Mg,Mn) Mayenite Powders

Substitution Level x is Mg and y is Mn	**Ca1-center (Å)**	**Ca2-center (Å)**	**Al1-center (Å)**	**O1-center (Å)**	**O2-center (Å)**
x=0.0 y=0.0	2.838	2.339	5.105	6.786	3.272
x=0.1 y=0.0	2.850	2.374	5.106	6.788	3.272
x=0.0 y=0.1	2.819	2.277	5.106	6.790	3.270
x=0.2 y=0.0	2.849	2.375	5.113	6.796	3.277
x=0.1 y=0.1	2.852	2.423	5.112	6.813	3.279
x=0.2 y=0.1	2.838	2.278	5.097	6.803	3.268

Figure 3.21 shows the TGA results of the (Mg+Mn) dual substituted samples compared to the individual substitution samples. The effect of the dual substitutes on the oxidation behavior is not consistent. The (0.2Mg+0.1Mn)-C12A7e$^-$ sample has a lower onset temperature of rapid oxidation than the C12A7e$^-$ sample, while individual Mg substituted samples showed higher onset temperatures than the C12A7e$^-$ sample. The TGA result of the (0.1Mg+0.1Mn)-C12A7e$^-$ sample showed an increase in the onset temperature of rapid oxidation (835.1 °C) comparable to that of the 0.1Mg-C12A7e$^-$ sample (834.8 °C). And no tailing off of the mass gain was observed at the maximum temperature for the (0.1Mg+0.1Mn)-C12A7e$^-$ sample.

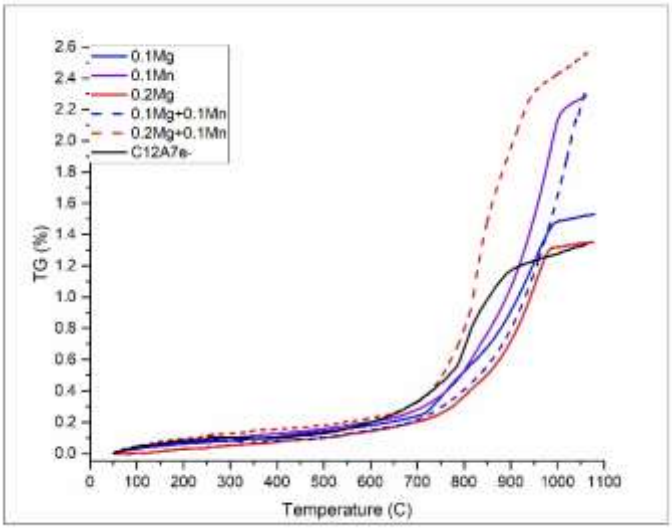

Figure 3.21 TGA Results of (Mg+Mn) Dual Substituted Mayenite Electride Compared to Individually Substituted (Mg,Mn) Mayenite Electride

Table 3.33 TGA Data-points of Mg and Mn Substituted Mayenite Electride

Substitution Level x is Mg and y is Mn	**Onset of Rapid Oxidation (°C)**	**Peak Oxidation Rate (%/min)**
x = 0.0 y = 0.0	662.1	0.0783
x = 0.1 y = 0.0	753.2	0.0580
x = 0.0 y = 0.1	834.8	0.1285
x = 0.2 y = 0.0	793.2	0.0819
x = 0.1 y = 0.1	835.1	0.1262
x = 0.2 y = 0.1	642.8	0.1368

The results of electrical conductivity of the samples are shown in Figure 3.22. The conductivity of (0.1Mg+0.1Mn)-C12A7e$^-$ sample (59.8S/cm at RT) is higher than that of the baseline C12A7e$^-$ sample (22.8S/cm). However, the (0.2Mg+0.1Mn)-C12A7e$^-$ sample shows conductivity (21.4S/cm at RT) almost the same as that of C12A7e$^-$.

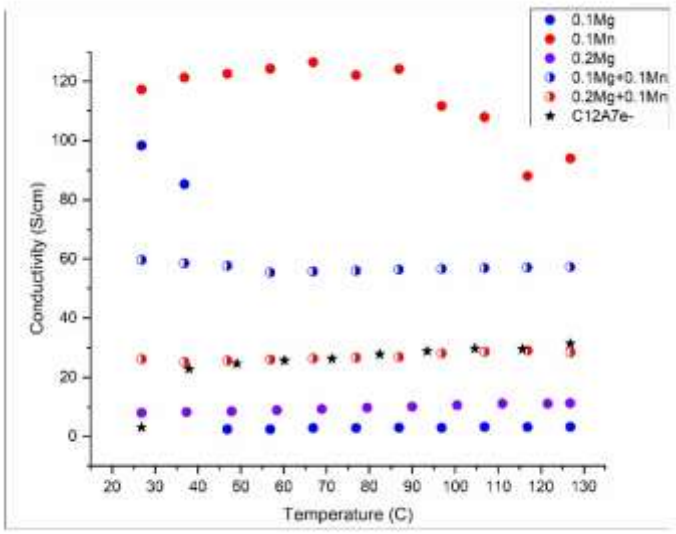

Figure 3.22 Electrical Conductivity of (Mg+Mn) Dual Substituted Mayenite Electride Compared to Individually Substituted (Mg,Mn) Mayenite Electride

3.3.4.1 Barium and Boron

The XRD results for the dual substitution powder samples, (0.1Ba+0.1B)-C12A7P and (0.1Ba+0.2B)-C12A7P, are shown in Figure 3.23. Both samples have the secondary CA phase at fairly elevated levels, as shown in Table 3.34. No barium or boron related peaks were observed in the XRD patterns.

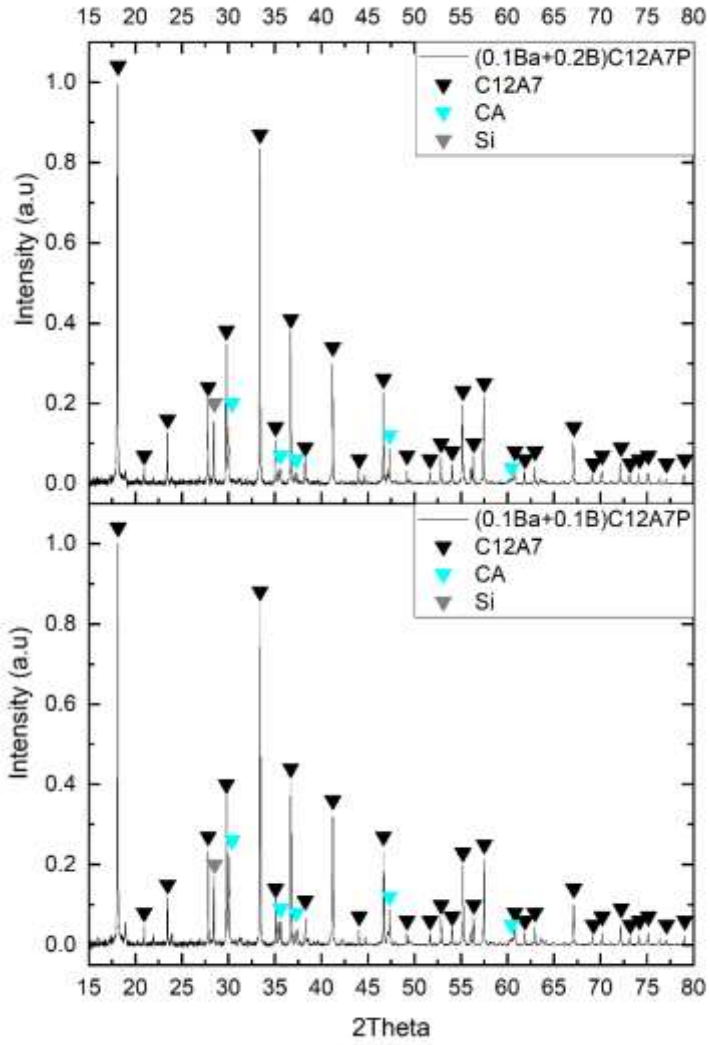

3.23 XRD Patterns of (Ba+B) Dual Substituted Mayenite Powder. (0.1Ba+0.1B)-C12A7P (lower) and (0.1Ba+0.2B)-C12A7P (upper).

Table 3.34 Phase Composition (wt%) of (Ba+B) Dual Substituted Mayenite Powder

Sample	C12A7 wt%	CA/C3A wt%
C12A7P	87.7	12.3
0.1B-C12A7P	95.4	4.6
0.1Ba-C12A7P	92.7	7.3
0.2B-C12A7P	92.9	7.1
(0.1Ba+0.1B)-C12A7P	67.6	32.4
(0.1Ba+0.2B)-C12A7P	75.6	24.4

The lattice parameters of the various samples with different substitute levels are provided in Table 3.35. The values in parentheses means the standard deviations at the last decimal digit. A progressive increase in the lattice parameter was observed when the substitute level is increased, which is consistent with the trend observed in both sets of the individual substitutions.

Table 3.35 Lattice Parameters of (Ba+B) Dual Substituted Mayenite Powder Compared to Individually Substituted (Ba,B) Mayenite Powders

Substitution Level x is Ba and y is B	Lattice Parameter (Å)
x = 0.0 y = 0.0	11.98677(2)
x = 0.1 y = 0.0	11.98322(2)
x = 0.0 y = 0.1	11.98538(3)
x = 0.0 y = 0.2	11.98604(3)
x = 0.1 y = 0.1	11.98806(3)
x = 0.1 y = 0.2	11.99024(3)

The structural parameters for (0.1Ba+0.1B)-C12A7P and (0.1Ba+0.2B)-C12A7P are given in Table 3.36 and Table 3.37. All the refinements for each substitution level achieved an R_{wp} factor of 5.4% or lower, indicating acceptable fit. The model refinement results of all the powder samples showed full occupancy of the O3 site and that the Ca1/Ca2 ratios are similar to those for the pure C12A7P.

Table 3.36 Refined Structural Parameters for (0.1Ba+0.1B)-C12A7P. Lattice parameters: a=11.98806(3)Å, space group $I\bar{4}3d$

Site	Wyckoff	x	y	z	Occ.	B_{iso}
Ca1	24d	0.1396(6)	0	0.25	0.81(2)	0.77(7)
Ca2	24d	0.181(2)	0	0.25	0.19(2)	0.5(3)
Al1	16c	0.01823(12)	0.01823(12)	0.01823(12)	1	0.90(8)
Al2	12a	0.875	0	0.25	1	0.73(8)
O1	48e	0.0364(2)	0.4431(2)	0.1513(3)	1	1.06(8)
O2	16c	0.1846(3)	0.1846(3)	0.1846(3)	1	1.88(19)
O3	48e	0.387(9)	0.01(4)	0.266(17)	0.042(3)	1.47(10)

Table 3.37 Refined Structural Parameters for (0.1Ba+0.2B)-C12A7P. Lattice parameters: a=11.99024(3)Å, space group $I\bar{4}3d$

Site	Wyckoff	x	y	z	Occ.	B_{iso}
Ca1	24d	0.1392(6)	0	0.25	0.80(2)	0.61(7)
Ca2	24d	0.181(2)	0	0.25	0.20(2)	0.7(3)
Al1	16c	0.01831(13)	0.01831(13)	0.01831(13)	1	0.94(8)
Al2	12a	0.875	0	0.25	1	0.53(8)
O1	48e	0.0368(2)	0.4422(2)	0.1516(3)	1	0.91(8)
O2	16c	0.1839(3)	0.1839(3)	0.1839(3)	1	1.68(19)
O3	48e	0.392(7)	-0.01(3)	0.273(10)	0.042(3)	1.29(10)

The change in structural parameters of the dual substituted samples does not significantly differ from that for the individual substitute samples. Additional B substitutes in the (0.1Ba+0.2B)-C12A7P sample shift the Ca1 site further away from the cage center, compared to how it changed the Ca1 site in the individual substitute samples.

Table 3.38 Changing Distance of Framework Atoms from Cage Center for (Ba+B) Dual Substituted Mayenite Powder Compared to Individually Substituted (Ba,B) Mayenite Powders

Substitution Level x is Ba and y is B	**Ca1-center (Å)**	**Ca2-center (Å)**	**Al1-center (Å)**	**O1-center (Å)**	**O2-center (Å)**
x=0.0 y=0.0	2.838	2.339	5.105	6.786	3.272
x=0.1 y=0.0	2.818	2.318	5.105	6.792	3.270
x=0.0 y=0.1	2.819	2.277	5.106	6.790	3.270
x=0.0 y=0.2	2.820	2.289	5.103	6.783	3.272
x=0.1 y=0.1	2.822	2.326	5.105	6.789	3.274
x=0.1 y=0.2	2.827	2.326	5.105	6.778	3.277

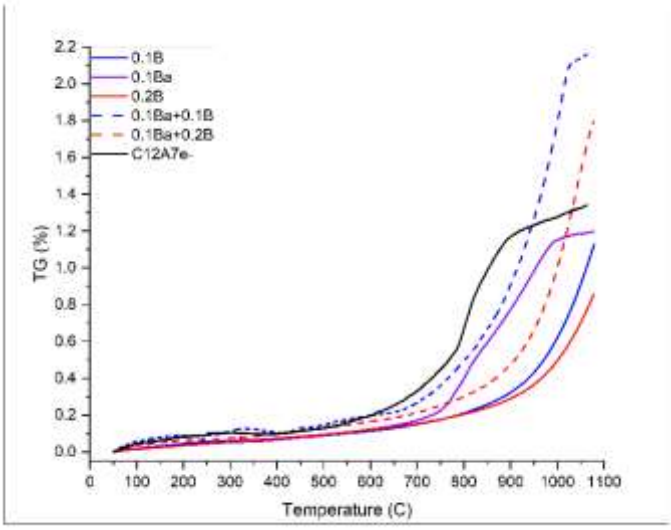

Figure 3.24 TGA Results of (Ba+B) Dual Substituted Mayenite Electride Compared to Individually Substituted (Ba,B) Mayenite Electride

The TGA results in Figure 3.24 show that both (Ba+B) dual substituted samples exhibited improved resistance to oxidation compared to the unsubstituted baseline C12A7e$^-$ sample, as suggested by the increase in onset temperature of rapid oxidation. Additional B in (0.1Ba+0.2B)-C12A7e$^-$ leads to further improvement in oxidation resistance, i.e., onset temperature increased to 878.6 °C, which indicates a cumulating effect from the boron.

Table 3.39 TGA Data-points of Ba and B Substituted Mayenite Electride

Substitution Level x is Ba and y is B	**Onset of Rapid Oxidation (°C)**	**Peak Oxidation Rate (%/min)**
x = 0.0 y = 0.0	662.1	0.0783
x = 0.1 y = 0.0	773.6	0.0448
x = 0.0 y = 0.1	906.9	0.0755
x = 0.0 y = 0.2	911.5	0.0559
x = 0.1 y = 0.1	837.8	0.1273
x = 0.1 y = 0.2	878.6	0.1122

The results of electrical conductivity show certain resemblance to those results of the individual substitute samples as seen in Figure 3.25. The (0.1Ba+0.1B)-C12A7e$^-$ sample shows a stark increase in conductivity up to 97.4S/cm at RT, compared to the baseline C12A7e$^-$ sample

(22.8S/cm). When additional B substitutes are introduced, the electrical conductivity decreased to 8.6S/cm at RT as shown in the (0.1Ba+0.2B)- C12A7e$^-$ sample. The decrease in conductivity with increasing B substitute level is consistent with what has been observed for the individual B substituted samples.

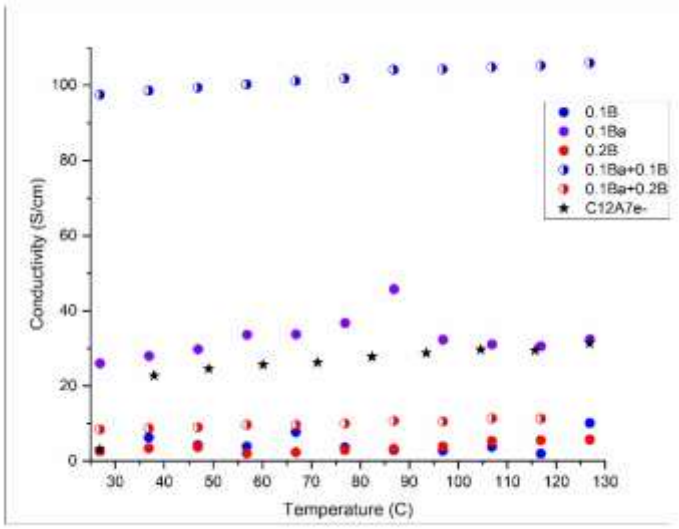

Figure 3.25 Electrical Conductivity of (Ba+Ba) Dual Substituted Mayenite Electride Compared to Individually Substituted (Ba,B) Mayenite Electride

3.4 Discussion

3.4.1 Substitution at Ca Site

In both studies of substitutions at the Ca site, the substitutes induced significant property changes of the mayenite electride. In the case of Mg substitution, it was anticipated that the introduction of smaller substitute atoms (28% reduction in ionic radius) should lead to a reduction in the lattice parameter; but the opposite trend was observed. This was supported by the calculated structural parameters that showed most of the framework atoms moving away from the cage center as the Mg content was increased. This contrasts with a previous study by

Bertoni et al., which reported the lattice parameter decreased as the Mg substitution level increased [27]. The trend of increasing lattice parameter with increasing Mg substitution level conflicts with the TGA results showing increasing Mg content leads to an increased resistance to oxidation. Previous research on the replacement of Ca by Sr reported that an increase in lattice parameter is associated with an increase in electron concentration resulting from easier removal of oxygen anions from the center of the cage [28]. The easier oxygen movement has been attributed to the increase in the size of the windows connecting the cages. In the present study, the samples with Mg substitution possessed larger lattice parameter, indicating larger size of windows, but the samples showed restricted oxygen movement compared to the "pure" mayenite electride sample. What must also be considered is the bonding between the encaged anion and the framework cations. Analyzing this structural change can help to explain the change in oxygen movement in the structure (and thus oxidation of the electride derivative). In the case of the Mg substituted samples, it was observed that the O3 atom moved closer to the Ca1 and Ca2 sites despite the outward expansion of these sites (lattice parameter increase). This can be attributed to the larger electronegativity value of Mg (1.31) compared to Ca (1.00). This is consistent with the theoretical calculations done by Bertoni et al., wherein the modeled hydrogen atom sitting in the center of the cage preferentially moved toward the Mg atom on the pseudo S4 axis [27]. A similar result would thus be expected for the electron anions in the electride: the Mg substitutes would have a stronger attraction to the electron anions thus inhibiting the introduction of oxygen anions back into the cage. The increasing resistance to oxidation is shown in Figure 3.26 below. The substitution level and the oxidation onset temperature have a Pearson correlation of 0.736 (substitution level being a positive number in this case). This indicates a positive linear relationship as the Pearson correlation coefficient is a normalized measure of

covariance taking values from -1 (perfect negative linear relationship) to 1 (perfect positive linear relationship).

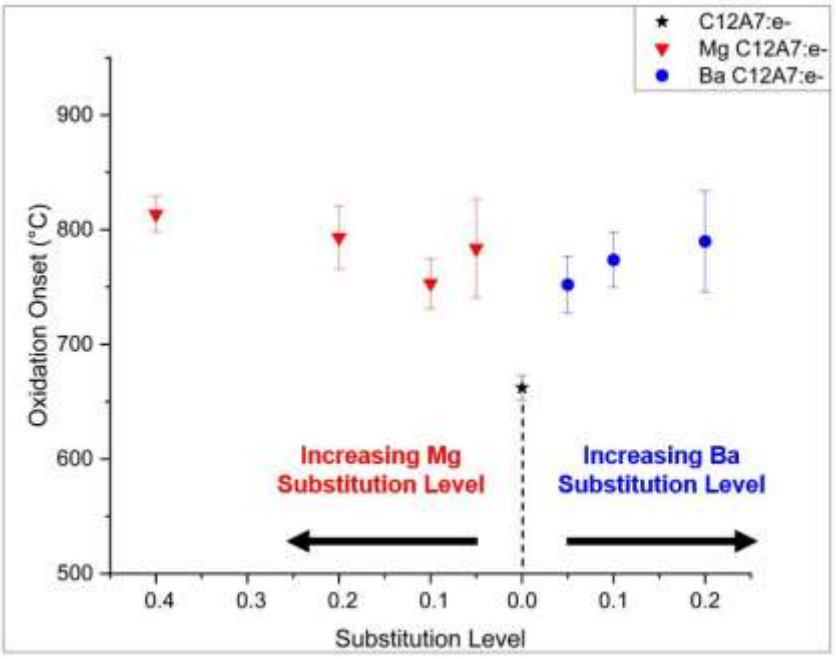

Figure 3.26: Effect of Substitution Level of Ca site Substitutes on Oxidation Onset Temperature.

Unlike the Mg substitute, the Ba substitute samples have lattice parameters smaller than those of the pure C12A7P but they increase as Ba content is raised. The 0.4Ba-C12A7P (C12A7P meaning unreduced mayenite powder) was observed to be distinct from the other samples after the furnace heating processing step as a large amount of secondary phase (67.4wt%) was observed. This indicated a failure to integrate all the substitutes into the lattice. The powder thus could not be reduced to electride completely, and the sample was excluded from the mechanism discussion. The increasing lattice parameters correspond to changes in the atomic positions. While a there is slight movement of the Ca1 and Ca2 atoms toward the cage center, the movement of the framework O1 atoms induced a substantial expansion in lattice across the Ba substitute samples. This movement of the O1 atoms away from the cage center is supported by the greater number of Ca-O1 bonds than Ca-O2 bonds in the cage so substitution for Ca more

directly impacts the O1 positioning. As seen in Figure 3.26, increasing Ba substitution results in increased oxidation resistance, which is reflected in the high Pearson coefficient of 0.848. Ba (0.89) has a lower electronegativity than Ca (1.00) and there is no movement of the O3 atom toward the cage walls as observed in the Mg substitute samples so the increased oxidation resistance cannot be ascribed to stronger bonding of the encaged anion to the framework. Additionally, while the lattice parameters of Ba substituted samples are smaller than those of pure C12A7P, the increasing trend of lattice parameter with substitution level in the Ba substitute samples excludes shrinking window size from being the mechanism by which the Ba substitute samples have increased their oxidation resistance.

As shown in Figure 3.27, the changes in electrical conductivity as a result of substitutes support the hypothesis that smaller cation substitutes induce decreased conductivity. All Mg substituted samples have decreased conductivity relative to the baseline C12A7e$^-$ sample, except the 0.05Mg-C12A7e$^-$ sample. The 0.05Mg-C12A7e$^-$ sample exhibited oxidation behavior (as shown in TGA results) very similar to the pure C12A7e$^-$, indicating that the change to the binding between the Ca/Mg sites and the occluded anion is very minimal. Moreover, the 0.05Mg-C12A7e$^-$ sample had a substantially higher mass gain than the other Mg substituted samples, which could indicate a higher electron concentration was achieved in the as-sintered condition. Higher electron concentration often leads to higher electrical conductivity, which explains why the 0.05Mg-C12A7e$^-$ exhibited an increased electrical conductivity compared to the pure C12A7e$^-$ sample. The other Mg substituted samples exhibited electrical conductivity an order of magnitude lower than that of the baseline C12A7e$^-$ sample. It has previously been shown that electrical conduction mechanism in mayenite electride is a combination of electron hopping and band conduction with the latter dominating at higher electron concentrations [30].

In both mechanisms of charge transport, the Ca site plays a significant role. The hopping path for localized electrons from atom to atom includes the Ca sites. In this conduction mechanism, the substitution of Mg would act as a blocking agent [27]. For the band conduction mechanism, the Mg likely contributes less to the density of states near the fermi level compared to the Ca atom due to lower energy orbitals which are less spatially extended due to smaller size [28]. Thus, the band conduction mechanism is suppressed with increasing Mg substitution. As seen in Figure 3.27, there is a Pearson correlation of -0.441 between conductivity and substitution level. It should be noted that in both oxidation resistance and electrical conductivity data sets for Mg substituted samples, the 0.05Mg-C12A7e$^-$ (electride disc) sample has the largest standard deviation in the experimentally measured data and has the strongest influence on the correlation coefficients.

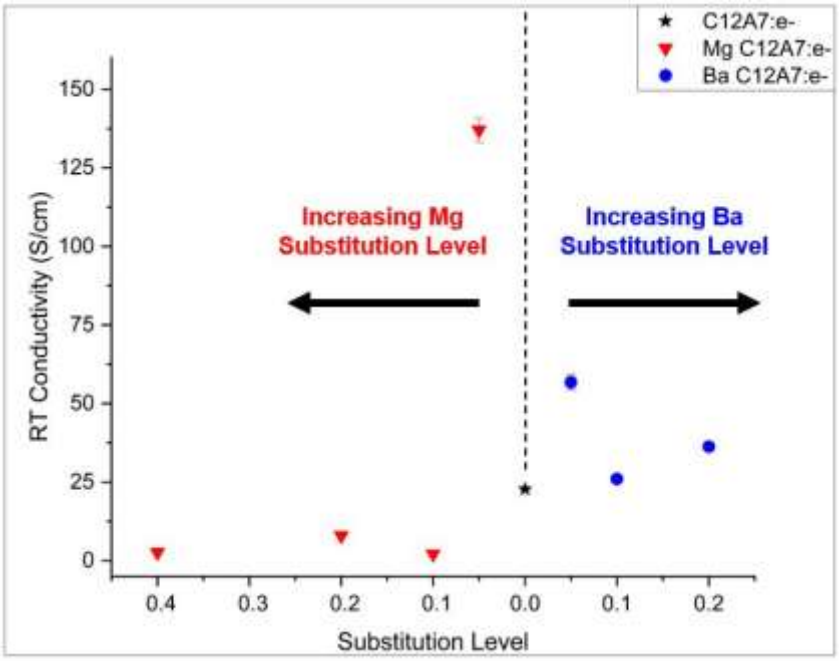

Figure 3.27: Effect of Substitution Level of Ca site Substitutes on Room Temperature Electrical Conductivity.

The opposite effect is observed in the case of the Ba substitute. Like a strontium (Sr) substitute, Ba substitute has a greater number of states to contribute to the DOS and thus, can contribute to

increased band conduction [20]. Though all the Ba substituted samples have increased electrical conductivity compared to pure C12A7e$^-$, there is not a strong statistical correlation between conductivity and Ba substitution level, as suggested by the Pearson coefficient close to zero (0.072). Only the 0.1Ba-C12A7e$^-$ sample had less mass gain than the pure C12A7e$^-$. The smaller mass gain in the TGA result indicates a lower electron concentration in the as sintered 0.1Ba-C12A7e$^-$ sample, which explains why it had the smallest increase in conductivity. The 0.1Ba-C12A7e$^-$ sample also experienced the largest inward movement of the Ca/Ba site (Table 3.16), giving further evidence that the connecting window is distorted, inhibiting oxygen removal during reduction reaction. The 0.05Ba-C12A7e$^-$ sample has the highest conductivity and the refinement model result shows the least movement of the Ca/Ba sites towards the cage center (Table 3.16), indicating the least distorted cage of all the samples. This is also reflected by a net mass gain close to that of the pure C12A7e$^-$ sample. The lack of correlation between electrical conductivity and Ba substitution level, combined with the unexplained effect of Ba substitution level on the oxidation onset temperature, highlights that integrating a substitute of a radical size difference is not a reliable process to improve the properties. Particularly at high substitution levels, the amount of the secondary phase increased significantly in 0.4Ba-C12A7P. In previous studies by others that investigated substitutes that have much larger atomic size than the solvent, inconsistent trends in property changes have also been reported [31], [32].

3.4.2 Substitution at Al Site

The counterpart to the Mg substitution for Ca site is the B substitution for Al. The B substitution resulted in a trend of lattice parameter increase with increasing B content. However, all but the 0.4B-C12A7P sample had a lattice parameter smaller than the pure C12A7P. This increase as a function of B dosage opposes the hypothesis that decrease in ionic radius (0.27Å

for B compared to 0.535Å for Al) to result in a decreased lattice parameter. The expansion to the lattice was mostly due to the outward movement of the Ca1 and Ca2 sites. Opposing the outward expansion of the cage was the Al1 site which progressively moved toward the center of the cage as the B content was increased (Table 3.21). However, this was not accompanied by consistent movement toward the O3 encaged anion site. In a previous study investigating gallium substitutes, the opposite effect was observed wherein the larger cation replacement moved the Al1 site outward and the Ca1 and Ca2 sites inward [21]. In all the B substituted samples, there was a significant increase in the onset temperature of rapid oxidation compared to pure C12A7e$^-$, as shown in Figure 3.28. The TGA results of the 0.2B-C12A7e$^-$ sample showed the greatest increase in the onset temperature of rapid oxidation. One important factor is the presence of the secondary CA phase in the 0.05B-C12A7e$^-$ and 0.4B-C12A7e$^-$ level samples (19.82wt% and 14.58wt% respectively). It was also notable that TGA results of all the B substituted samples did not show the mass gain tailing off at high temperatures in the same way as observed in the pure C12A7e$^-$ sample. This is further evidence that the B substitution is associated with restricted oxidation. The increase in the oxidation resistance of the 0.1B-C12A7e$^-$ and 0.2B-C12A7e$^-$ samples is greater than that of the Mg substituted samples, indicating that the cation size on the Al site has a more pronounced structural effect than the Ca site. However, the B substitute induces a much more radical size change (49.5% smaller than Al), compared to the case of Mg substituting Ca (28% size difference). The Pearson correlation between the rapid oxidation onset temperature and B substitution level is relatively low (0.242). However, if the 0.4B-C12A7e$^-$ sample was excluded, the correlation would increase to 0.842. It is likely that 0.4 level of B substitutes exceeds the acceptable substitution level, i.e., “over-substituted”, due to the large size change from Al to B.

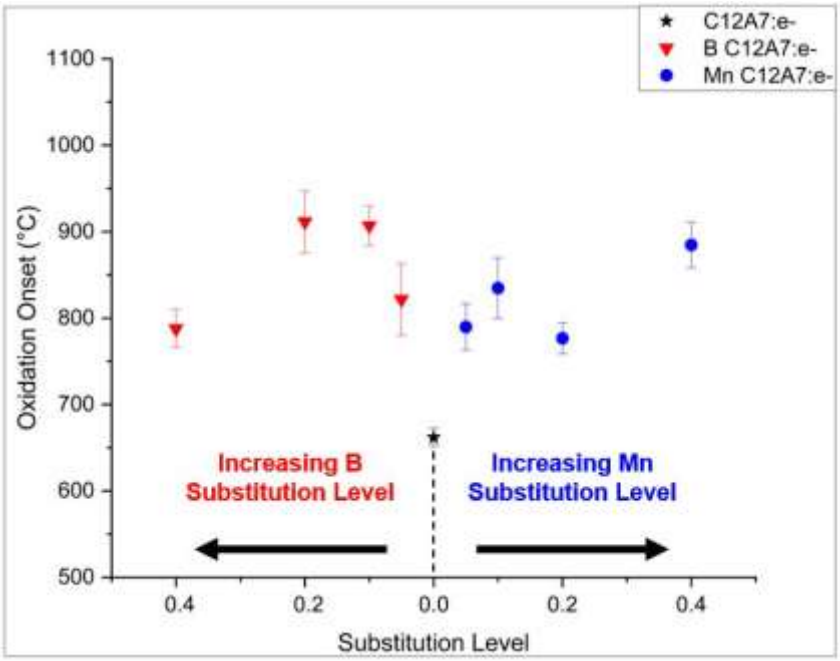

Figure 3.28: Effect of Substitution Level of Al site Substitutes on Oxidation Onset Temperature.

Similar to the B substituted samples, the Mn substituted samples exhibited decreased lattice parameters compared to C12A7P. These samples also have a decreasing trend in lattice parameter with increasing Mn content. This is the opposite of the hypothesis, as Mn has an ionic radius 14.5% larger the the solvent Al cation. One possible explanation is that Mn in a 2+ valence state could substitute at the Ca site rather than the prescribed Al site. This would represent a 25% reduction to the ionic radius of Ca site. The Mn substituted samples exhibited oxidation behavior similar to the Mg substituted samples, despite that the increase in the onset temperature of rapid oxidation for the samples with higher level substitutes is more pronounced than that in the Mg substitute cases. The samples with higher level of Mn substitutes contained a significant amount of secondary phase that could interfere with the effect of the substitutes. It is also worth noting that a $CaMnO_3$ phase was detected in the XRD pattern of the 0.2Mn-C12A7P sample, which indicates that some Ca atoms do not reside at the lattice points of the mayenite structure due to being replaced by the Mn atoms (i.e. Mn has substituted for Ca). It is also

possible that Mn in 4+ state could substitute itself onto either of the Al sites while also bringing extra oxygen or hydroxide anions into the structure, as previously reported in the study on using Si as the substitute [22], [29]. Interestingly this Mn^{4+} substitution would represent no change to the ionic radius, so it still does not explain the decreasing lattice parameter or altered structural parameters. All the Mn substituted samples experienced a particularly high net mass gain, shown by the TGA results, which would give credence to the case that Mn is in a 4+ state and a higher number of occluded anions leads to higher amount of occluded electrons. However, it would not be expected that the additional mass gain in these samples would trend down with additional substitution as it does. The structural data does not have any clear trends to elucidate which of these cases (Mn^{2+} or Mn^{4+}) is most likely.

In both cases of substitutes at the Al site, the electrical conductivity decreased compared to the baseline C12A7e$^-$ material, as observed in Figure 3.29. The electrical conductivity of the B substituted samples decreased with increasing B content. When the B substitute level is ≥ 0.2, the electrical conductivity went below 1S/cm (the 0.2B-C12A7e$^-$ and 0.4B-C12A7e$^-$ samples). The Pearson correlation between conductivity and B substitution level is -0.769. All these samples have a decreased occupancy for the Ca2 site, which is directly connected to the presence of occluded electrons. The trend for the Ca2 occupancy directly follows the lattice parameter trend.

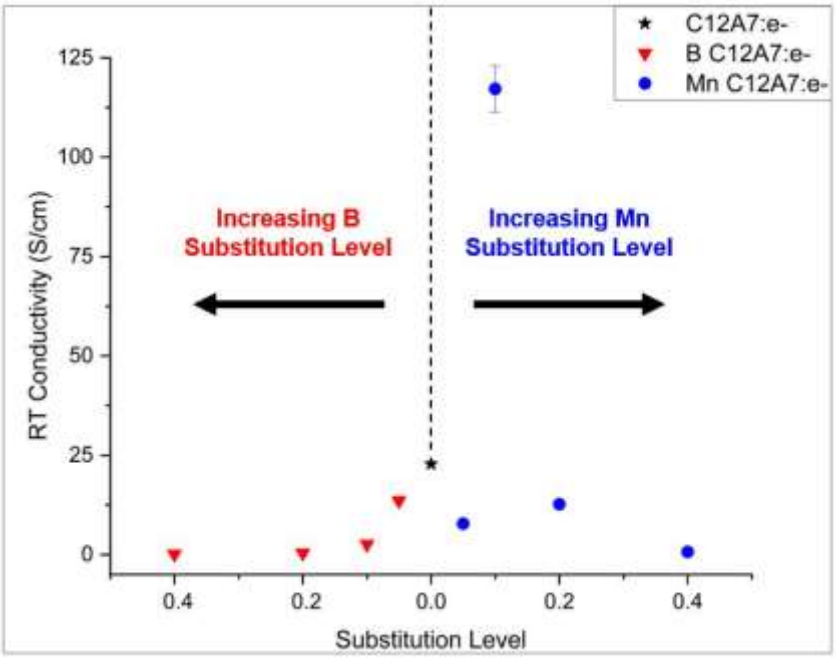

Figure 3.29: Effect of Substitution Level of Al site Substitutes on Room Temperature Electrical Conductivity.

The Mn substituted samples also have decreased Ca2 occupancy in their structural models, though the trend does not follow the decreasing lattice parameter trend. The Pearson coefficient for these data points is -0.303. All but 0.1Mn-C12A7e$^-$ have decreased conductivity, which further disproves the idea that the atom has entered a 4+ state and accommodated more electrons in the cages. It would be expected that given the greater number of accessible states for Mn that it would help to increase conductivity, but it is possible this would be inhibited by clustering of the substitutes due to lattice strain, which has been observed in other atomic substitutions in mayenite such as Fe and Mg [19], [27].

3.4.3 Dual Substitution

The purpose of dual substitution of the Ca and Al sites was to harness the effects observed from individual site substitutions and combine them in order to improve both thermal stability and electrical conductivity, which often seem to be opposed to one another in the mayenite electride system. In Table 3.29, the effects of the individual substitutions on thermal

stability and electrical conductivity are summarized qualitatively. Table 3.30 shows the predicted qualitative change in property assuming ideal combination of the individual substitutional effects. These predictions consider the relative magnitude of property change brought on by the individual substitutions. Highlighted are cases in which the dual substituted sample not only outperformed pure mayenite electride but also outperformed the individually substituted samples.

Table 3.40 Qualitative Changes to Properties for Individually Cation Substituted Mayenite Electride

Individual Substitute	Thermal Stability Change	Electrical Conductivity Change
Mg	↑	↓
Mn	↑	↓
B	↑	↓
Ba	↑	↑

Table 3.41 Predicted and Observed Qualitative Changes to Properties for Dual Substituted Mayenite Electride

Dual Substitute	Predicted Thermal Stability Change	Observed Thermal Stability Change	Predicted Electrical Conductivity Change	Observed Electrical Conductivity Change
0.1Mg+0.1Mn	↑	↑	↓	↑
0.2Mg+0.1Mn	↑	↓	↓	--
0.1Ba+0.1B	↑	↑	↓	↑
0.1Ba+0.2B	↑	↑	↓	↓

The Mg+Mn dual substitute samples do not show a clear combination of substitutional effects. The (0.1Mg+0.1Mn)-C12A7e$^-$ sample has an increased lattice parameter compared to both of the individual 0.1 level substitutions. The structural data shows that, similar to the individual Mg substitutions, this sample had outward movement of all the framework cations. However, unlike the Mg substitution, this is not accompanied by movement of the O3 anion toward the Ca/Mg site. There is notable movement of the anion toward both Al cation sites

which could explain the slight increase in the onset temperatures of rapid oxidation of the sample (tighter bonding of the oxygen to the framework). This movement of O3 site toward the Al sites was also observed in the individual Mn substituted samples. However, the movement in the individual Mn substituted samples was not as great in magnitude and was not correlated with the Mn substitution level. The structural data of the (0.2Mg+0.1Mn)-C12A7e^- sample showed almost the complete opposite effect wherein all the framework atoms (except O1) shifted back toward the center of the cage, resulting in a reduced lattice parameter. The TGA data shows the (0.2Mg+0.1Mn)-C12A7e^- sample oxidizing more readily than (0.1Mg+0.1Mn)-C12A7e^- .(0.2Mg+0.1Mn)-C12A7e^- also tails off in oxidation at a lower temperature than (0.1Mg+0.1Mn)-C12A7e^-. The (0.2Mg+0.1Mn)-C12A7e^- sample also has conductivity almost identical to the C12A7e^-. The similarity in the properties between the (0.2Mg+0.1Mn)-C12A7e^- sample to the pure mayenite electride sample suggests that the increased Mg dosage resulted in lack of integration of Mg and Mn into the C12A7 structure. The relatively small amount of secondary calcium aluminate phases (4.6wt%) in the (0.2Mg+0.1Mn)-C12A7P sample is a clear distinction between this sample and the other (Mg+Mn) and (Ba+B) dual substitution samples. In particular, it is odd to see such a significant decrease in secondary phase compared to the (0.1Mg+0.1Mn)-C12A7P sample (40.9wt%) considering there is an overall trend of increased secondary phase with substitutional dosage. In the case of the (0.1Mg+0.1Mn)-C12A7e^- sample the explanation of the increased conductivity and the increased resistance to oxidation is difficult. Neither Mg nor Mn substitution led to increased electrical conductivity. The most reasonable explanation for (0.1Mg+0.1Mn)-C12A7e^- is that some of the Mn substitutes are in a 4+ valence state. This would account for the increased electrical conductivity as an increase in

valence would accommodate more electron anions. Moreover, the increased charge would be more attractive to the anions, binding them tighter to the Al1 site as was observed.

In the case of the B and Ba dual substituted samples, there are not yet clear combinations of individual substitute effects, but the results suggest that one substitute plays a dominant role in each sample. Each of the individual substitutions have a trend of increasing lattice parameter with increasing substitution level. For both of the dual substituted samples, the calculated lattice parameters were larger than those of the individual substituted samples with the same substitution level. The lattice expansion was mostly owed to the outward expansion of the Ca/Ba sites. This feature was the distinguishing structural feature of the individually substituted B substitute samples. For the (0.1Ba+0.1B)-C12A7e$^-$ sample, the outward movement of the Ca/Ba sites resulted in an increase to onset of rapid oxidation on par with the individual substituted 0.1Ba-C12A7e$^-$ sample, though substantially less than that of the individually substituted B substitute samples. Additionally, this sample displayed an increased electrical conductivity to nearly four times that observed in the 0.1Ba- C12A7e$^-$ sample. The difference in ionic radius between Ba and Ca (35%) is smaller than that between B and Al (-49.5%). Thus, Ba substitutes are more readily to be incorporated into the lattice structure. The substitution effects are dominated by the Ba atom in this sample, as the actual substitution level for Ba is likely higher than B. The additional dosage of B in the (0.1Ba+0.2B)-C12A7e$^-$ sample further delays oxidation to a higher temperature, though still not on par with the individually substituted samples. Additional B dosage in the (0.1Ba+0.2B)-C12A7e$^-$ sample results in a decrease in conductivity compared to (0.1Ba+0.1B)-C12A7e$^-$. Considering all those results together, it is reasonable to conclude that B is the dominant substitute in this sample. While it is yet more difficult to incorporate B substitutes into the mayenite lattice due to the large size difference between B and

Al, the additional amount of B may increase the driving force to diffuse B atoms into the Al site due to the higher concentration gradient.

3.5 Summary

This chapter discussed a variety of individual and dual cation substitutions in the mayenite electride and the effects on the lattice structure, oxidation behavior, and electrical conductivity. The key findings are summarized below.

- Substitutions of Ca- or Al- framework ions with cations of smaller size result in substantial increase in the onset of rapid oxidation of the material (by >200°C). This is attributed to a stronger binding between the framework cation and the occluded electron anions brought about from both structural movement of the substitutional atom toward the center of the cage and/or a stronger attractive force due to the higher electronegativity of smaller cations.
- Increased thermal stability can be achieved through substitution of larger cations (Ba). However, the effects are less pronounced compared to small cation substitution. This applies to much larger cation substitutions as well, though substitutions outside the typical range of size change (15%) result in less consistent effects on the structure and properties.
- Dual substitution, when in equal dosage, is dominated by the site with the larger size change, as shown by the results of (Ba+B) samples. Combined beneficial effects from individual substitutions were observed. But further study on varying substitution levels is required to understand how these combinations can be better tailored.

References

[1] J. L. Dye, "Electrides: Ionic Salts with Electrons as the Anions," *Science*, vol. 247, no. 4943, pp. 663–668, Feb. 1990, doi: 10.1126/science.247.4943.663.

[2] J. L. Dye, "Electrons as Anions," *Science*, vol. 301, no. 5633, pp. 607–608, Aug. 2003, doi: 10.1126/science.1088103.

[3] S. Matsuishi *et al.*, "High-Density Electron Anions in a Nanoporous Single Crystal: [Ca24Al28O64]4+(4e-)," *Science*, vol. 301, no. 5633, pp. 626–629, Aug. 2003, doi: 10.1126/science.1083842.

[4] Y. Toda *et al.*, "Work Function of a Room-Temperature, Stable Electride [Ca24Al28O64]4+(e–)4," *Advanced Materials*, vol. 19, no. 21, pp. 3564–3569, 2007, doi: 10.1002/adma.200700663.

[5] T. Yoshizumi and K. Hayashi, "Thermionic Electron Emission from a Mayenite Electride–Metallic Titanium Composite Cathode," *Appl. Phys. Express*, vol. 6, no. 1, p. 015802, Dec. 2012, doi: 10.7567/APEX.6.015802.

[6] Y. Xiao *et al.*, "Synthesis of [Ca24Al28O64]4+(4e−)+LaB6 composite ceramic bulk and its electron emission properties," *Vacuum*, vol. 205, p. 111437, Nov. 2022, doi: 10.1016/j.vacuum.2022.111437.

[7] M. McDonald and N. R. S. Caruso, "Ignition and Early Operating Characteristics of a Low-Current C 12 A 7 Hollow Cathode IEPC-2017-253 / ISTS." Accessed: Jul. 22, 2022. [Online]. Available: https://www.semanticscholar.org/paper/Ignition-and-Early-Operating-Characteristics-of-a-C-McDonald-Caruso/9c5818b314959befad2bcd55a49fbffe7a2f231c

[8] D. R. Lev, I. G. Mikellides, D. Pedrini, D. M. Goebel, B. A. Jorns, and M. S. McDonald, "Recent progress in research and development of hollow cathodes for electric propulsion," *Rev. Mod. Plasma Phys.*, vol. 3, no. 1, p. 6, Dec. 2019, doi: 10.1007/s41614-019-0026-0.

[9] L. Palacios, A. Cabeza, S. Bruque, S. García-Granda, and M. A. G. Aranda, "Structure and Electrons in Mayenite Electrides," *Inorg. Chem.*, vol. 47, no. 7, pp. 2661–2667, Apr. 2008, doi: 10.1021/ic7021193.

[10] H. Boysen, M. Lerch, A. Stys, and A. Senyshyn, "Structure and oxygen mobility in mayenite (Ca12Al14O33): a high-temperature neutron powder diffraction study," *Acta Cryst B*, vol. 63, no. 5, pp. 675–682, Oct. 2007, doi: 10.1107/S0108768107030005.

[11] F. Li, X. Zhang, and J. Zhang, "Aluminothermic synthesis of [Ca24Al28O64]4+(4e−) electride ceramic directly from Ca3Al2O6 precursor," *Vacuum*, vol. 167, pp. 352–356, Sep. 2019, doi: 10.1016/j.vacuum.2019.06.031.

[12] F. Gfeller, "7. Mayenite $Ca_{12}Al_{14}O_{32}[X^{2-}]$: From minerals to the first stable electride crystals," in *Highlights in Mineralogical Crystallography*, T. Armbruster and R. M. Danisi, Eds., DE GRUYTER, 2015, pp. 169–196. doi: 10.1515/9783110417104-009.

[13] S. Matsuishi, T. Nomura, M. Hirano, K. Kodama, S. Shamoto, and H. Hosono, "Direct Synthesis of Powdery Inorganic Electride [Ca24Al28O64]4+(e−)4 and Determination of Oxygen Stoichiometry," *Chem. Mater.*, vol. 21, no. 13, pp. 2589–2591, Jul. 2009, doi: 10.1021/cm9007987.

[14] S. W. Kim and H. Hosono, "Synthesis and properties of 12CaO · 7Al2O3 electride: review of single crystal and thin film growth," *Philosophical Magazine*, vol. 92, no. 19–21, pp. 2596–2628, Jul. 2012, doi: 10.1080/14786435.2012.685770.

[15] P. V. Sushko, A. L. Shluger, M. Hirano, and H. Hosono, “From Insulator to Electride: A Theoretical Model of Nanoporous Oxide 12CaO·7Al2O3,” *J. Am. Chem. Soc.*, vol. 129, no. 4, pp. 942–951, Jan. 2007, doi: 10.1021/ja066177w.

[16] H. Hosono and M. Kitano, “Advances in Materials and Applications of Inorganic Electrides,” *Chem. Rev.*, vol. 121, no. 5, pp. 3121–3185, Mar. 2021, doi: 10.1021/acs.chemrev.0c01071.

[17] Y. Toda *et al.*, “Field Emission of Electron Anions Clathrated in Subnanometer-Sized Cages in [Ca24Al28O64]4+(4e-),” *Adv. Mater.*, vol. 16, no. 8, pp. 685–689, Apr. 2004, doi: 10.1002/adma.200306484.

[18] K. Khan *et al.*, “A comprehensive review on synthesis of pristine and doped inorganic room temperature stable mayenite electride, [Ca24Al28O64]4+(e−)4 and its applications as a catalyst,” *Progress in Solid State Chemistry*, vol. 54, pp. 1–19, Jun. 2019, doi: 10.1016/j.progsolidstchem.2018.12.001.

[19] J. R. Salasin and C. Rawn, “Structure Property Relationships and Cationic Doping in [Ca24Al28O64]4+ Framework: A Review,” *Crystals*, vol. 7, no. 5, Art. no. 5, May 2017, doi: 10.3390/cryst7050143.

[20] M. Zhang *et al.*, “Enhancement of encaged electron concentration by Sr2+ doping and improvement of Gd3+ emission through controlling encaged anions in conductive C12A7 phosphors,” *Phys. Chem. Chem. Phys.*, vol. 18, no. 28, pp. 18697–18704, Jul. 2016, doi: 10.1039/C6CP02026G.

[21] L. Palacios, S. Bruque, and M. A. G. Aranda, “Structure of gallium-doped mayenite and its reduction behaviour,” *physica status solidi (b)*, vol. 245, no. 4, pp. 666–672, 2008, doi: 10.1002/pssb.200743425.

[22] M. I. Bertoni, T. O. Mason, J. E. Medvedeva, Y. Wang, A. J. Freeman, and K. R. Poeppelmeier, “Enhanced electronic conductivity in Si-substituted calcium aluminate,” *Journal of Applied Physics*, vol. 102, no. 11, p. 113704, Dec. 2007, doi: 10.1063/1.2817605.

[23] “Materials Science and Engineering: An Introduction, 10th Edition | Wiley,” Wiley.com. Accessed: Nov. 19, 2024. [Online]. Available: https://www.wiley.com/en-us/Materials+Science+and+Engineering%3A+An+Introduction%2C+10th+Edition-p-9781119405498

[24] V. M. Goldschmidt, “Die Gesetze der Krystallochemie,” *Naturwissenschaften*, vol. 14, no. 21, pp. 477–485, May 1926, doi: 10.1007/BF01507527.

[25] B. Schwarz *et al.*, “Structure, site symmetry and spin-orbit coupled magnetism of a Ca12Al14O33 mayenite single crystal substituted with 0.26 at.% Ni,” *Physica B: Condensed Matter*, vol. 666, p. 415090, Oct. 2023, doi: 10.1016/j.physb.2023.415090.

[26] K. Hayashi, S. Matsuishi, N. Ueda, M. Hirano, and H. Hosono, “Maximum Incorporation of Oxygen Radicals, O- and O2-, into 12CaO·7Al2O3 with a Nanoporous Structure,” *Chem. Mater.*, vol. 15, no. 9, pp. 1851–1854, May 2003, doi: 10.1021/cm020959g.

[27] M. I. Bertoni, T. O. Mason, J. E. Medvedeva, A. J. Freeman, K. R. Poeppelmeier, and B. Delley, “Tunable conductivity and conduction mechanism in an ultraviolet light activated electronic conductor,” *Journal of Applied Physics*, vol. 97, no. 10, p. 103713, May 2005, doi: 10.1063/1.1899246.

[28] X. Zhang *et al.*, “Sr-doping enhanced electrical transport and thermionic emission of single crystal 12CaO·7Al2O3 electride,” *Current Applied Physics*, vol. 20, no. 1, pp. 96–101, Jan. 2020, doi: 10.1016/j.cap.2019.10.008.

[29] K. Khan *et al.*, “Facile synthesis of a cationic-doped [Ca24Al28O64]4+(4e−) composite via a rapid citrate sol–gel method,” *Dalton Trans.*, vol. 47, no. 11, pp. 3819–3830, Mar. 2018, doi: 10.1039/C7DT04543C.

[30] S. Matsuishi, S. W. Kim, T. Kamiya, M. Hirano, and H. Hosono, “Localized and Delocalized Electrons in Room-Temperature Stable Electride [Ca24Al28O64]4+(O2-)2-x(e-)2x: Analysis of Optical Reflectance Spectra,” J. Phys. Chem. C, vol. 112, no. 12, pp. 4753–4760, Mar. 2008, doi: 10.1021/jp711631j.

[31] H. Yi, Y. Lv, V. Mattick, and J. Xu, “Cobalt-doped Ca12Al14O33 mayenite oxide ion conductors: phases, defects, and electrical properties,” *Ionics*, vol. 25, no. 11, pp. 5105–5115, Nov. 2019, doi: 10.1007/s11581-019-03088-0.

[32] H. Yi, Y. Lv, Y. Wang, X. Fang, V. Mattick, and J. Xu, “Ga-doped Ca12Al14O33 mayenite oxide ion conductors: synthesis, defects, and electrical properties,” *RSC Adv.*, vol. 9, no. 7, pp. 3809–3815, Jan. 2019, doi: 10.1039/C8RA08254E.

Chapter 4 A- and B-site substitutions in the cubic perovskite oxide strontium vanadate structure and the subsequent effects on thermal stability and electrical conductivity

The study on mayenite electride and the associated rigor in developing acceptable models via Rietveld refinement demonstrated the challenges faced when modifying such a complex structure. To separate the effects of cationic substitution from the effects of mayenite's complex cage structure, a similar approach was employed to develop a thermally stable, low work function material with a significantly simpler structure. This chapter discusses the findings from my study on strontium vanadate, a cubic perovskite oxide compound. The perovskite structure has been well studied, but this version of it has not gained attention as a candidate for thermionic emission until recently. The study aims to break ground with regard to specific cation substitutions and elucidate how the A- and B-sites dictate properties in this specific perovskite oxide. The interplay between these sites was further explored with dual substitution which was thought to be more readily accommodated in perovskite structure than in the case of mayenite. X-ray diffraction and Rietveld modeling were used to confirm the integration of the substitute cations into the structure. Thermal analysis was performed to examine the onset of first and second stage oxidation as well as the oxidation rates during the two steps. Electrical conductivity is also reported. Results show that calcium substitution for strontium produces an exceptional increase in both thermal stability and electrical conductivity. Manganese substitution proves to be unstable due to mixed valence states. Key findings from dual substitution suggest that a harder upper boundary of 1.05 should be applied to the tolerance factor when considering substitutes.

4.1 Introduction

Strontium vanadate ($SrVO_{3-\delta}$) has garnered significant attention in recent years due to its potential applications in energy conversion technologies, particularly in the realms of thermoelectric conversion and thermionic emission [1], [2], [3], [4], [5]. This interest is rooted in its perovskite oxide structure, a class of materials renowned for their versatile properties and structural flexibility. The perovskite structure, represented as ABO_3, allows for extensive substitution of cations at both the A- and B-sites. This allows for tailoring the material's properties to meet specific application requirements. Perovskite oxides such as $SrVO_{3-\delta}$ possess a cubic structure wherein the B-site cations (vanadium in this case) are surrounded by an octahedron of oxygen atoms. The A-site cations (strontium) occupy the spaces between these octahedra. This configuration not only facilitates high electrical conductivity but also supports a low theoretical work function [6], [7], [8], [9]. The low work function is particularly advantageous for thermionic emission applications, where efficient electron emission is paramount.

The synthesis of $SrVO_{3-\delta}$ typically involves solid-state reactions between strontium carbonate and vanadium pentoxide at high temperatures (≥1100°C) in a reducing atmosphere [10], [11], [12], [13]. This process is crucial to achieving the desired oxygen-deficient cubic perovskite phase. This is a multistep reaction in which the precursors initially form strontium pyrovanadate ($Sr_2V_2O_7$) before this phase is reduced to a combination of strontium orthovanadate ($Sr_3V_2O_8$) and SrV_6O_{11}. Upon further reduction, the combination of these phases in a 5:1 ratio yields the final pure phase [10].

One of the standout features of $SrVO_{3-\delta}$ is its excellent electrical conductivity, which exceeds 1000S/cm [14]. This high conductivity is attributed to the presence of tetravalent vanadium ions (V^{4+}) in a $3d^1$ configuration, contributing to a broad conduction band [8], [15]. Additionally, the material benefits from oxygen vacancies (denoted by the 3-δ in its formula), which further enhance its conductive properties [16], [17]. Despite these promising attributes, $SrVO_{3-\delta}$ faces challenges related to oxidation stability. The open structure of the perovskite lattice makes it susceptible to oxidation, particularly at elevated temperatures. Thermogravimetric analysis indicates that over half of the vanadium cations can be oxidized to the pentavalent state (V^{5+}) before reaching 600°C, resulting in a significant reduction in conductivity [10], [18]. Furthermore, this often leads to breakdown of the cubic structure with the material returning to a combination of pyrovanadate and orthovanadate which makes any sort of return to the functional state extremely time consuming. To address these stability issues, researchers have explored various cation substitution strategies [11], [19], [20]. For instance, substituting strontium with yttrium or lanthanum has shown potential in enhancing the material's oxidation resistance. Yttrium substitution increased the stability boundary significantly, while lanthanum substitution provided even greater improvements [11]. However, these modifications can also degrade the material's conductivity and other properties, necessitating a balanced approach to substitution. Furthermore, while the perovskite oxide structure can accommodate various cations, extensive substitution can lead to the formation of secondary phases during material processing, which do not contribute to thermionic emission. Despite the basic structure, studies on strontium vanadate are yet very limited. There remains a gap in understanding as to how expansion and contraction of the structure via cation substitution affects the thermal stability and electronic properties. The current work investigated cation substitutions on both the A-site (strontium (Sr)) and B-site

(vanadium (V)) in the strontium vanadate perovskite oxide and aimed to elucidate the correlation between cation substitutes and the changes observed in electrical conductivity and thermal stability. Additionally, dual substitution—simultaneously replacing both A- and B-sites—were explored, as this approach has the potential to combine the beneficial effects resulting from individual substitutional cations.

4.2 Materials and Methods

4.2.1 Cation Selection

The primary focus of this study was the effect of cation size on the strontium vanadate crystal structure. Therefore, both substitutional cations with a larger ionic radius and one with a smaller ionic radius than the solvent cations (i.e. Sr^{2+} and V^{4+}) were selected for the strontium and vanadium sites, respectively. The B-site in this structure can accommodate several charges depending on the degree of oxidation and this factored into selection for the atom and precursor to substitute at this site. To select suitable cationic substitutes, the trade-off between a sufficiently large difference in ionic radius (to induce perceptible change in the lattice structure) and the solubility limit (the threshold amount of solutes that can be added without causing phase change or forming a new second phase) must be considered. The latter point leans heavily on the Hume-Rothery rules and the Goldschmidt rules, particularly the size effect [21], [22]. This is the concept which generalizes atomic substitution into three regimes according to the difference in the ionic radius of the solvent atom and the substitutional atom. Less than 15% difference in the radii generally results in significant substitution. A difference ranged from 15% to 30% generally results in limited ability to substitute. Greater than 30% difference makes substitution difficult.

With all these considerations the cations selected for substitution are shown in Table 4.01 with the substitution site specified and the difference in ionic radius noted.

Table 4.01 Strontium Vanadate Cation Substitution Selection. Radii from Shannon Database of Ionic Radii used.

Solute Cation	**Solvent Cation**	**Difference in Ionic Radius**
Ca	Sr	-7%
Ba	Sr	11%
Ti	V	4%
Mn	V	-9%

4.2.2 Powder Processing and Sintering

The cation substituted strontium vanadate powder was processed via powder solid state reactions. For pure strontium vanadate powder the precursor powders strontium carbonate and vanadium pentoxide are mixed in a 2:1 ratio and reacted according to EQ(1-3). Vanadium pentoxide is chosen over vanadium sesquioxide as previous studies have shown that use of the latter powder results in greater amounts of impurities in the final product [14].

$$2SrCO_3 + V_2O_5 \rightarrow Sr_2V_2O_7 + 2CO_2 \quad \text{EQ(1)}$$

$$8Sr_2V_2O_7 \rightarrow 5Sr_3V_2O_8 + SrV_6O_{11} \quad \text{EQ(2)}$$

$$5Sr_3V_2O_8 + SrV_6O_{11} \rightarrow 8SrVO_{3-\delta} \quad \text{EQ(3)}$$

Cation substituted powders were produced in similar fashion but with the appropriate precursors substituted for strontium carbonate and vanadium pentoxide. Precursor powders were mixed to produce compounds $Sr_{1-x}Z_xVO_{3-\delta}$ or $SrV_{1-x}Z_xO_{3-\delta}$ where Z is the solute atom and x=(0.1, 0.2, 0.3, and 0.4). Dual substitution was done at two levels for two separate pairs of substitutional atoms. The first pair of atoms was a calcium (Ca) substitute for Sr and a manganese (Mn) substitute for V. The second pair was a barium (Ba) substitute for Sr and a titanium (Ti) substitute for (V). The

pairs were made such that lattice distortion from the increase in size on one atom could possibly be balanced by the decrease in size at another size. First a sample with equivalent low dose for each substitution was synthesized (x=0.1 for both substitutes). After this was examined, there was interest in looking specifically at prescribing a higher dose for the decreased substitute (x=0.1 for the large substitute and x=0.2 for the smaller substitute). This would allow for an overall contraction of the lattice to be observed while the structure still experienced some of the influence of the larger cation substitute on the electronic structure.

Starting powders are $SrCO_3$ (≥ 99.9%, Sigma Aldrich), V_2O_5 (≥99.9%, Sigma Aldrich), $CaCO_3$ (≥ 99.9%, Sigma Aldrich), $BaCO_3$ (≥99%, Oakwood Chemical), Ti_2O_3(≥99.98%, Sigma Aldrich), and MnO (≥99%, Sigma Aldrich). These are mixed in the proper stoichiometric ratio and milled in a planetary ball mill (Across International PQ-N4) with a ball to powder weight ratio of 10:1 at 400 RPM using a 5-minute-on and 10-minute-off duty cycle to minimize frictional heating in the nylon jars. Mixed precursors are placed in alumina crucibles for powder solid state reaction in a 5:95H_2:N_2 gas mixture at 1300°C for 16hrs. Formed strontium vanadate powders are reground in agate ball mill jars for an additional 2hrs and then loaded into a 20mm diameter graphite tooling set used in the SPS. Within the tooling set, the powder is surrounded on the circumference and on top and bottom with graphite foils to curb effects of contact resistance with the tooling. $SrVO_{3-\delta}$ powders are then heated to 1500°C in SPS vacuum chamber at a rate of 100 °C/min with a large uniaxial load (45MPa) and a 20-minute hold.

Table 4.02 Strontium Vanadate Sample IDs

Sample ID (Shorthand)	Notes
SVOP	Strontium Vanadate powder after furnace heating in reducing environment
SVOD	Strontium Vanadate solid sample after SPS consolidation
0.xZ-SVOP	Cation substituted Strontium Vanadate powder after furnace heating in reducing environment. Z is solute cation and x is substitution level.
0.xZ-SVOD	Cation substituted Strontium Vanadate solid sample after SPS consolidation. Z is solute cation and x is substitution level.
(0.xW+0.yZ)-SVOP	Dual substituted Strontium Vanadate powder after furnace heating in reducing environment. W,Z are solute cations and x,y are substitution levels.
(0.xW+0.yZ)-SVOD	Cation substituted Strontium Vanadate solid sample after SPS consolidation. W,Z are solute cations and x,y are substitution levels.

4.2.3 Phase Characterization and Rietveld Modeling

The crystal structures present in each sample were characterized via powder x-ray diffraction (XRD) using a Bruker D8 Discover DaVinci Powder X-ray Diffractometer. Scans were taken in a 2θ range of 20°-150° using kα radiation (k=1.5406Å) with a step size of 0.01°. Phase composition is analyzed matching patterns to those found on the International Center for Diffraction Data (ICDD) database. Particular attention is paid to the reduction reaction intermediary phases strontium pyrovanadate and strontium orthovanadate as well as secondary phases arising from the substitutional cations. Also considered are the precursor powders as well as some of the less common phases on the SrO-V_2O_5 phase diagram. Lattice parameter and structural data were calculated by Rietveld Refinement using TOPAS6 software. A small amount of silicon (≤5wt%) is added to the powder. The main peak from the silicon is fit first to give a better correction to the sample height and provide more confidence in lattice parameter

calculations. The strontium vanadium structure with refinement parameters is given below in Table 4.03

Table 4.03 Strontium Vanadate Structure and Refinement Parameters. Lattice parameters: a~3.840Å, space group $Pm\bar{3}m$

Site	**Wyckoff**	**x**	**y**	**z**	**Occ.**	**B_{iso}**
Sr1	1a	0.5	0.5	0.5	Sr/ASub_occ	SrB
V1	1b	0	0	0	V/BSub_occ	VB
O1	3d	0.5	0	0	1	OB

Any parameters given by a variable name rather than a number (SrB,V_occ , etc.) are variables refined in the model. As cation substitutes are introduced, they are placed on the same site as the solvent cation. As they occupy the same site, both the solvent cation's and the solute cation's occupancies are refined, but these occupancies are restricted to a sum of one. Refining the oxygen occupancy was attempted to calculate oxygen deficiency but the data resolution proved insufficient. Isotropic displacement parameters are employed as the resolution of the data does not provide enough reliability to use anisotropic parameters. First refined were the background, lattice parameters, and peak shape parameters. This was followed by the atomic parameters and then isotropic displacement parameters. After all of these were fit to an acceptable degree, occupancies were refined.

4.2.4 Thermal Analysis

Small samples (20-30mg) are cut and polished for thermal analysis. Thermogravimetric analysis (SEIKO) is performed using Pt pans in an ambient atmosphere (pO_2 ~ 0.21atm) using a heating rate of 10°C/min. Scans were performed between 50°C and 1050°C. Rapid oxidation points are calculated by examining the second derivative of polynomial fit to the mass change data.

Rate of oxidation is reported as percent mass change over time to correct for different sizes of samples. After samples are oxidized, they are examined under XRD to probe for decomposition.

4.2.5 Electrical Conductivity Testing

Sintered samples were cut into rectangular bars and polished for analysis. Copper leads are attached to the bar samples using a silver epoxy (EpoTek). Electrical resistance is measured as a function of temperature using a four-probe set-up in a Quantum Design Physical Property Measurement System (PPMS). Resistance is calculated from measured voltage to reach input current given to PPMS system. Several input currents (0.1-100mA) are tested to maximize current without throwing AC current out of phase. Three specimens from each sample are tested over a temperature range of 25°C-125°C. Temperature is increased in increments of ten degrees and at each temperature point three resistance measurements are taken and averaged.

4.3 Results

4.3.1 Baseline Material: Strontium Vanadate

The baseline material is obtained by the methods described in section 4.2. The reducing environment provided by the hydrogen gas allows for the conversion of the precursors to the secondary phase vanadates ($Sr_2V_2O_7$, $Sr_3V_2O_8$, SrV_6O_{11}) and then finally the cubic perovskite phase $SrVO_{3-\delta}$. Upon reduction the precursor powder turns color from a dull yellow to a blue as seen in Figure 4.01.

Figure 4.01 Strontium Vanadate Powder (SVOP) Post Furnace Heating in 5:95 H_2:N_2 Environment

The XRD pattern for the reduced powder (**SVOP**) is shown in Figure 4.02. The material is primarily cubic phase perovskite but there are some low intensity peaks corresponding to the strontium orthovanadate phase indicating the reaction is not entirely complete. Quantitative analysis indicates that the primary phase is the cubic perovskite with a 71.9 weight percent (wt%) composition.

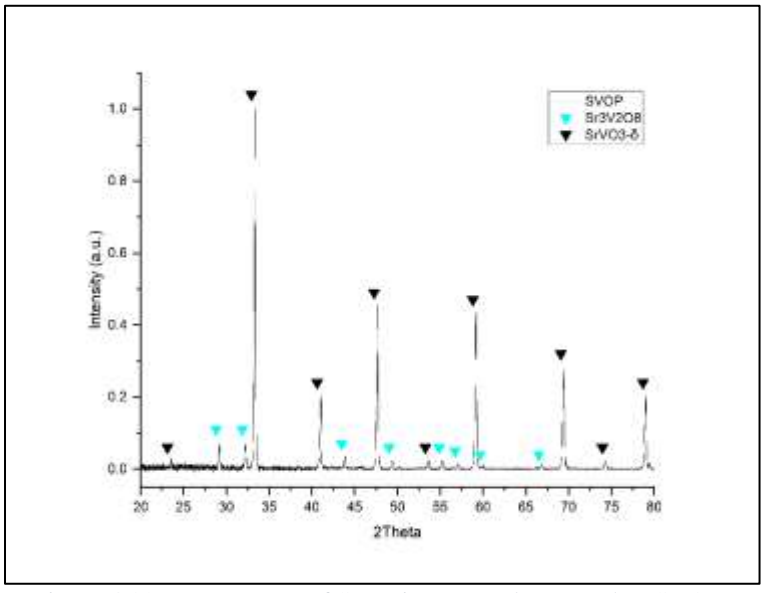

Figure 4.02 XRD Pattern of Strontium Vanadate Powder (SVOP)

After the powder is sintered at high temperature the disc sample is much darker, nearly black in color. The XRD pattern of the sample (**SVOD**) in Figure 4.03 shows that the additional time at

high temperature combined with the carbothermal environment provided by the SPS tooling allows the reduction reaction to progress to completion.

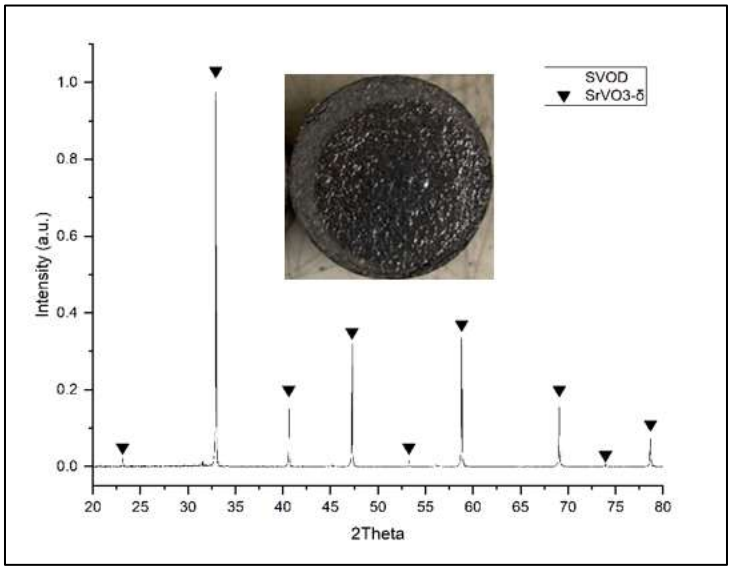

Figure 4.03 XRD Pattern of Strontium Vanadate Solid Sample (SVOD)

The results of the Rietveld refinement of the structure are shown in Table 4.04. The model has a good fit indicated by the R-value of 6.738%. The sample has an enlarged lattice parameter (3.843Å) which could be indicative of oxygen vacancies.

Table 4.04 Strontium Vanadate Solid Sample (SVOD) Structural Parameters. Lattice parameters: a=3.843Å, space group $Pm\bar{3}m$

Site	**Wyckoff**	**x**	**y**	**z**	**Occ.**	**B_{iso}**
Sr1	1a	0.5	0.5	0.5	1	0.767
V1	1b	0	0	0	1	0.892
O1	3d	0.5	0	0	1	1.058

The oxidation of the disc is shown in the TGA plot in Figure 4.04. The disc oxidizes in two distinct steps which is typical for the material. The first oxidation point at 290.5°C is activated by the oxygen vacancies being filled. At higher temperatures more oxygens are absorbed by the system as the trivalent and tetravalent vanadium atoms shift to a pentavalent state. The net mass gain of 3.5% is reasonable for the material, though the pattern would suggest

that the material is not fully oxidized as it is still gaining mass at a substantial rate at peak temperature.

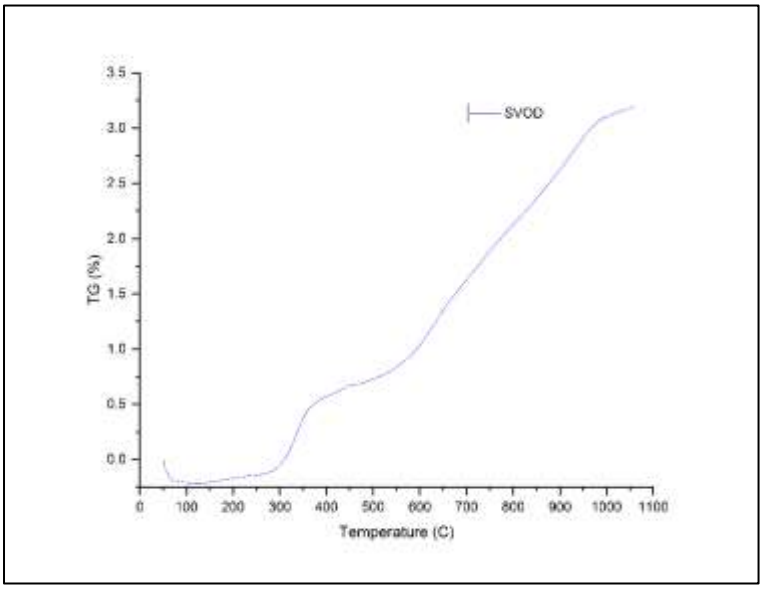

Figure 4.04 TGA Result of Strontium Vanadate Solid Sample (SVOD)

The conductivity of the sample has a maximum value of 113.1S/cm. As indicated by the plot in Figure 4.05 the material demonstrates a metallic conductivity with conductivity decreasing down to 88.0S/cm at maximum temperature 125°C.

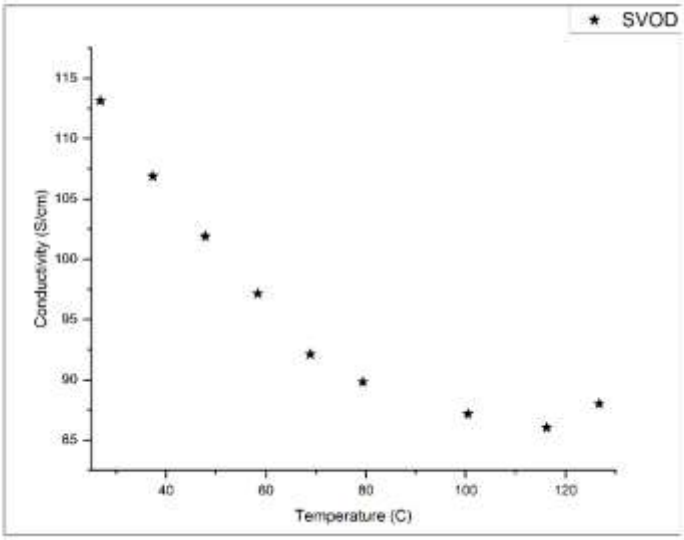

Figure 4.05 Electrical Conductivity of Strontium Vanadate Solid Sample (SVOD)

4.3.2 Strontium Site Substitution

4.3.2.1 Calcium

The XRD pattern for 0.2Ca-SVOD sample is shown in Figure 4.06. The powder does not show any remaining calcium carbonate unreacted with the rest of the precursor powders. There is no evidence of any secondary calcium-based phases in the powder. This powder has a moderate amount of remaining strontium orthovanadate (12.3wt%).

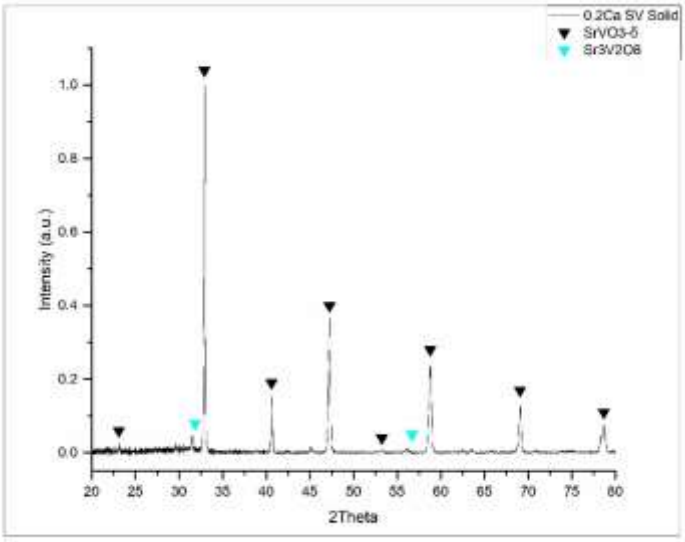

Figure 4.06 XRD Pattern of Ca Substituted Strontium Vanadate (0.2Ca-SVOD)

All of the substituted powders had varying amounts of orthovanadate remaining as shown in Table 4.05. There was no discernable pattern to the remaining orthovanadate phase, and, by relation, the progression of reaction. It was noted that the powder furthest upstream (closest to the reducing gas) did achieve the greatest progression of reaction, but no further pattern correlating position in the furnace with orthovanadate content was observed. Upon sintering in SPS all samples have <5wt% remaining orthovanadate phase. However, upon sintering, the sharper peaks of the disc sample for 0.4Ca-SVOD did show a distinct peak splitting wherein it became clear that a separate $CaVO_3$ phase had formed.

Table 4.05 Phase Composition (wt%) of Ca Substituted Strontium Vanadate Powders

Sample	$SrVO_3$ wt%	$Sr_3V_2O_8$ wt%
SVOP	73.6	26.4
0.1Ca-SVOP	61.1	38.9
0.2Ca-SVOP	87.7	12.3
0.3Ca-SVOP	73.8	26.2
0.4Ca-SVOP	96.4	3.6

The results of the Rietveld refinements for all of the substituted samples are shown in Table 4.06 and include the lattice parameter, calcium occupancy, and R-factors. The lattice parameter for all samples fall below that of pure strontium vanadate except for the 0.1Ca-SVOD. Furthermore, increasing substitution level is correlated with decreasing lattice parameter. All of the calcium occupancies which the refinements arrived at were very close to the nominal values prescribed for the powders except for the case of 0.4Ca-SVOD where the calcium formed a secondary phase. The R-factors are all below ten percent, indicating acceptable fit. The fit is further confirmed with graphical inspection.

Table 4.06 Structural Parameters of Ca Substituted Strontium Vanadate Solid Samples

Sample	Lattice Parameter (Å)	Ca-Occupancy	R_{wp} (%)
SVOP	3.84473(2)	N/A	7.015
0.1Ca-SVOD	3.847183(18)	0.08(3)	8.304
0.2Ca-SVOD	3.837236(14)	0.21(2)	7.000
0.3Ca-SVOD	3.82741(2)	0.33(6)	9.395
0.4Ca-SVOD	3.82940(10)	0.083(4)	8.609

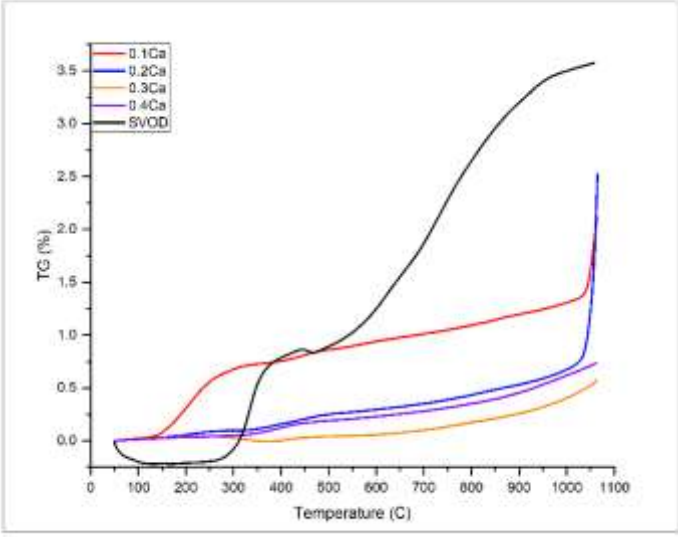

Figure 4.07 TGA Results of Ca Substituted Strontium Vanadate

The TGA results for the calcium samples are shown in Figure 4.07. The 0.1Ca-SVOD sample has a much different oxidation pattern compared to the other three samples as it shows the first stage of oxidation beginning at a much lower temperature (115.5°C) even compared to the pure strontium vanadate. Furthermore, the sample then has a radically reduced rate of oxidation compared to SVOD before ultimately spiking in oxidation rate near the maximum temperature similar to the 0.2Ca-SVOD sample.

Table 4.07 TGA Data-points of Ca Substituted Strontium Vanadate

Substitution Level	**Onset of 1st Stage Oxidation (°C)**	**Onset of 2nd Stage Oxidation (°C)**	**Peak Oxidation Rate (%/min)**
x = 0.00	290.5	421.4	0.0822
x = 0.10	115.5	1010.9	0.3702
x = 0.20	N/A	1011.9	0.9459
x = 0.30	N/A	N/A	0.0385
x = 0.40	N/A	N/A	0.0212

The 0.2Ca-0.4Ca-SVOD samples all lack a first stage of oxidation, instead showing a gentle increase in mass across the temperature profile. It should be noted that the 0.4Ca-SVOD sample has higher mass gain compared to the 0.3Ca-SVOD sample. This is important when considered

with the extraneous calcium vanadate phase seen in XRD. Conductivity results also indicate this extraneous phase led to decreased performance.

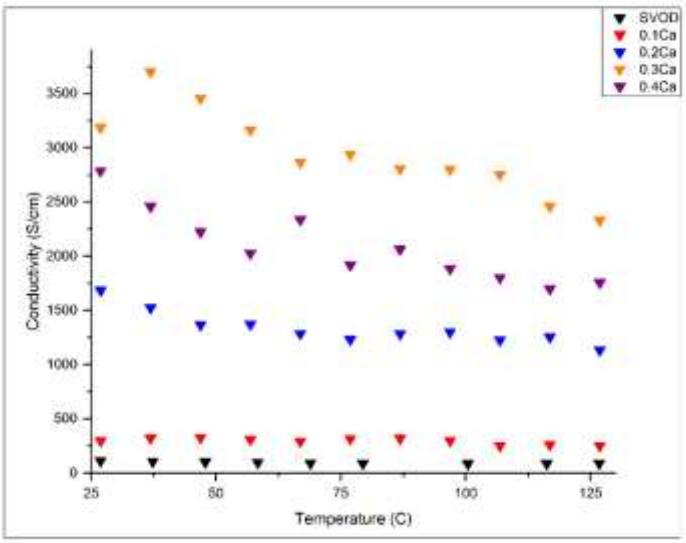

Figure 4.08 Electrical Conductivity of Ca Substituted Strontium Vanadate

All of the calcium substituted samples have a radically increased electrical conductivity compared to SVOD (113.1S/cm) and all have a decreasing conductivity with temperature, though the latter attribute is more distinct for the samples with higher Ca dosage. Room temperature conductivity increases with substitution level for the three lowest dosage samples 0.1Ca-SVOD (297.1S/cm), 0.2Ca-SVOD (1685.0S/cm), and 0.3Ca-SVOD (3186.7S/cm). The 0.4Ca-SVOD sample has a reduced conductivity (2787.5S/cm) compared to the 0.3Ca-SVOD sample.

4.3.2.2 Barium

The XRD pattern for 0.2Ba-SVOD sample is shown in Figure 4.09. The sample does not have any remaining strontium orthovanadate. However, there is a small amount of another orthovanadate phase, this one with a substitution of Ba for Sr in the structure on the nominal level of the prescribed substitution. Another vanadate phase with strontium and barium in equal

amount appears in the pattern, but again this phase is in very small quantity (<5wt%). The disc samples in general have much less secondary phase content than their powder counterparts demonstrating that the additional heating in the SPS chamber allows for further progression of the reduction reaction.

Table 4.08 Phase Composition (wt%) of Ba Substituted Strontium Vanadate Solid Samples

Sample	**$SrVO_3$ wt%**	**$Sr_3V_2O_8$ wt%**	**Ba Secondary Phases**
SVOD	>99.0	<1.0%	N/A
0.1Ba-SVOD	N/A	N/A	N/A
0.2Ba-SVOD	97.3	N/A	2.7
0.3Ba-SVOD	>99.0	N/A	<1.0
0.4Ba-SVOD	95.4	N/A	4.6

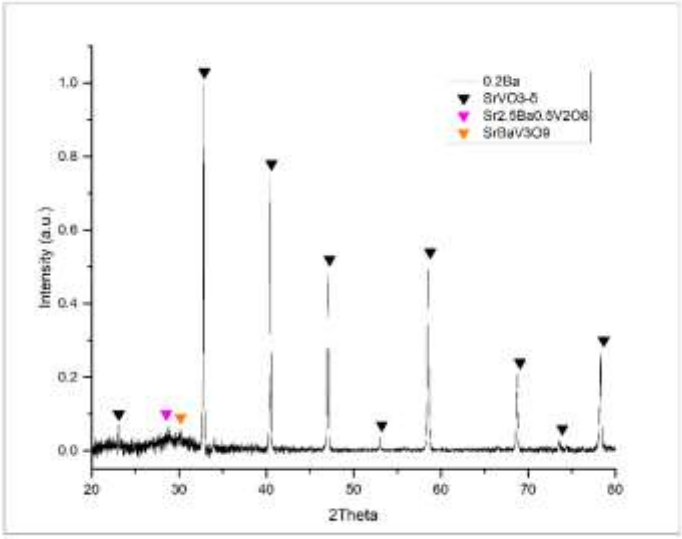

Figure 4.09 XRD Pattern of Ba Substituted Strontium Vanadate (0.2Ba-SVOD)

The results of the Rietveld refinements for all of the substituted samples are shown in Table 4.09 and include the lattice parameter, barium occupancy, and R-factors. The lattice parameter for all samples is greater than that of pure strontium vanadate. As the substitution level increases the lattice parameter increases as well. The barium occupancies which the refinements arrived at do have deviations from the nominal values prescribed for the samples. In particular,

the 0.2SVOD and 0.3SVOD samples have almost flipped occupancies (the 0.2SVOD sample has an occupancy near 0.3 and vice versa). The R-factors are all below ten percent except for the 0.1Ba-SVOD model. This sample has a distinct peak split for the primary peak which could not be fit. Attempts were made to fit separate perovskite structure with barium as the A-site cation, but this distinct peak was too far displaced from the overall pattern.

Table 4.09 Structural Parameters of Ba Substituted Strontium Vanadate Solid Samples

Sample	**Lattice Parameter (Å)**	**Ba-Occupancy**	**R_{wp} (%)**
SVOD	3.84643(2)	N/A	7.015
0.1Ba-SVOD	3.854247(9)	0.12(4)	15.507
0.2Ba-SVOD	3.85883(11)	0.29(8)	9.757
0.3Ba-SVOD	3.86410(5)	0.21(12)	7.267
0.4Ba-SVOD	3.86934(16)	0.35(2)	8.480

Thermogravimetric analysis results are shown in Figure 4.10. In all of the substituted discs, rapid oxidation onset occurs at higher temperature than the pure strontium vanadate. However, there is a trend of rapid oxidation onset temperature deceasing with higher Ba content. Decreasing rapid oxidation onset temperature is also associated with the oxidation stages being more visually apparent in the TGA curves. The 0.4Ba-SVOD sample exhibits oxidation in in two clear steps whereas for the 0.1Ba-SVOD sample there is almost no distinguishable first oxidation step.

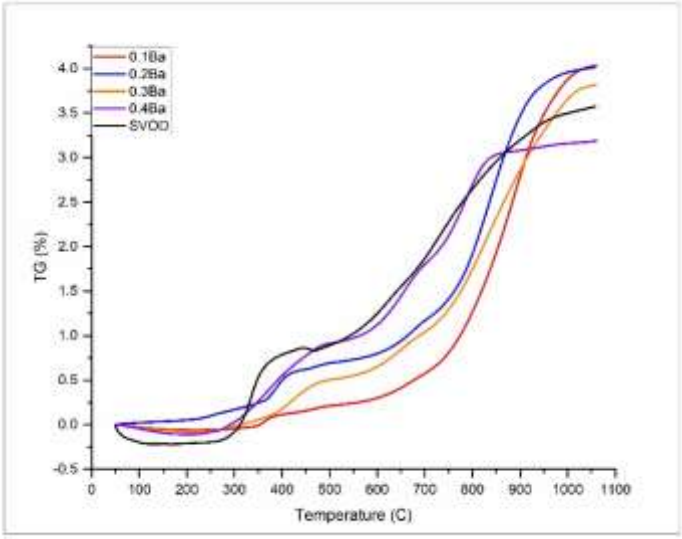

Figure 4.10 TGA Results of Ba Substituted Strontium Vanadate

Table 4.10 TGA Data-points for Ba Substituted Strontium Vanadate

Substitution Level	**Onset of 1st Stage Oxidation (°C)**	**Onset of 2nd Stage Oxidation (°C)**	**Peak Oxidation Rate (mg/sec)**
x = 0.00	290.5	421.4	0.0822
x = 0.10	322.4	742.7	0.1620
x = 0.20	344.6	705.6	0.1650
x = 0.30	322.7	662.2	0.1114
x = 0.40	219.9	547.3	0.1172

The conductivity results are shown in Figure 4.11. Two of the four substituted discs have an increased conductivity. The 0.1Ba-SVOD sample has a room temperature conductivity of 401.6S/cm and the 0.3Ba-SVOD sample has a room temperature conductivity of 706.7S/cm. The 0.2Ba-SVOD sample meanwhile has little change in conductivity compared to SVOD. The 0.4Ba-SVOD sample has a decrease in conductivity by an order of magnitude compared to SVOD.

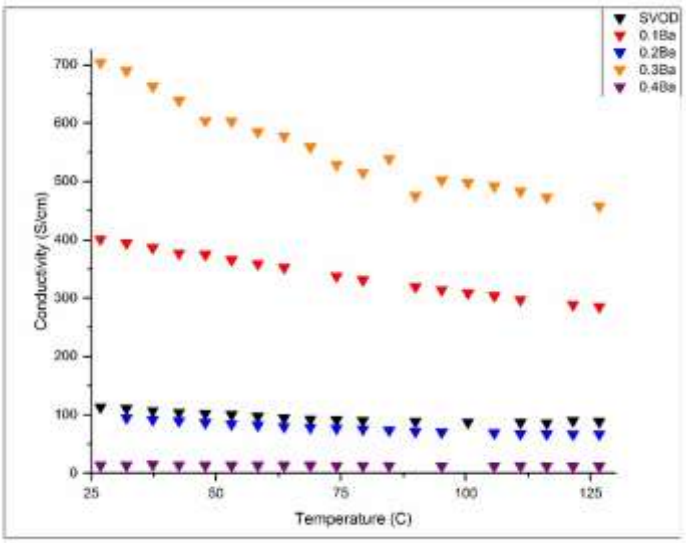

Figure 4.11 Electrical Conductivity of Ba Substituted Strontium Vanadate

4.3.3 Vanadium Site Substitution

4.3.3.1 Manganese

The diffraction patterns for the Mn substituted powders revealed secondary phases as more of an issue compared to the samples with both substitutions for Sr. While the 0.1Mn-SVOP and 0.2Mn-SVOP samples have a majority cubic perovskite oxide phase the 0.3Mn-SVOP and 0.4Mn-SVOP samples instead have massive amounts of unreduced secondary phases (Table 4.11) including strontium pyrovanadate which had not been observed in any of the previous powders. The large amount of these phases demonstrates that the Mn substitute hinders the reduction reaction. The 0.4Mn-SVOP sample has such a diverse collection of secondary phases that achieving anything close to an acceptable fit with a Rietveld refinement proved too difficult.

Table 4.11 Phase Composition (wt%) of Mn Substituted Strontium Vanadate Powders

Sample	$SrVO_3$ wt%	$Sr_3V_2O_8$ wt%	$Sr_2V_2O_7$ wt%
SVOP	73.6	26.4	N/A
0.1Mn-SVOP	76.9	23.1	N/A
0.2Mn-SVOP	64.5	35.5	N/A
0.3Mn-SVOP	34.5	61.0	3.5
0.4Mn-SVOP	N/A	N/A	N/A

Upon sintering in SPS, the 0.1Mn-SVOD and 0.2Mn-SVOD samples have the high level of cubic phase purity as observed in other samples (>99%) as shown by the clean XRD pattern for 0.2Mn-SVOD in Figure 4.12. The 0.3Mn-SVOD and 0.4Mn-SVOD samples, however, did not experience as significant improvement, though the 0.3Mn-SVOD sample did still have cubic perovskite as the primary phase (not majority). The lack of cubic perovskite phase in the 0.4Mn-SVOD sample led to the decision to not further test the sample in conjunction with the others. The Rietveld model for the 0.1Mn-SVOD sample showed no occupancy for the Mn substitute, but this contradicts the model for 0.1Mn-SVOP which showed the occupancy at a more acceptable value of 0.15 (nominally it should be 0.1). Considering the large amount of misfit in the 0.1Mn-SVOD model due to a significant underestimation of the peak from the (200) plane and the better fit achieved by the 0.1Mn-SVOP model it is fair to assume the Mn substitute was integrated into the lattice near the prescribed value. The 0.3Mn-SVOD sample was observed to have a variety of secondary phases both native to the Sr-V-O phase diagram as well as phases involving manganese. The 0.3Mn-SVOD XRD pattern also showed a substantial amount of vanadium metal (8.5wt%) in the sample.

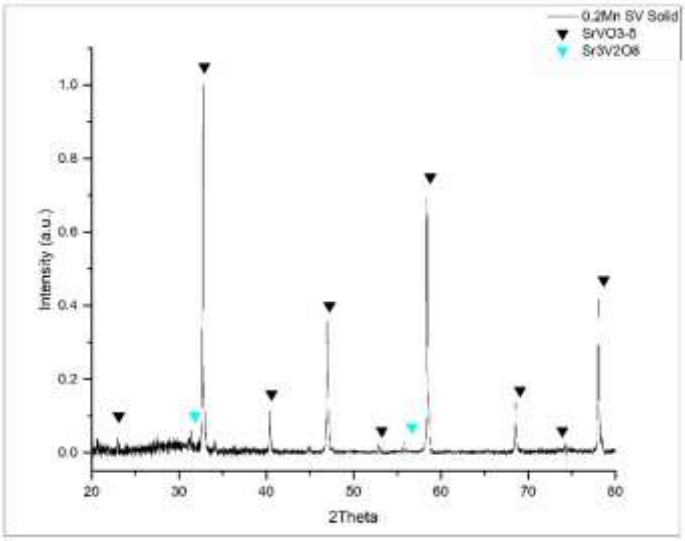

Figure 4.12 XRD Pattern of Mn Substituted Strontium Vanadate (0.2Mn-SVOD)

Table 4.12 Structural Parameters of Mn Substituted Strontium Vanadate Solid Samples

Sample	**Lattice Parameter (Å)**	**Mn-Occupancy**	**R_{wp} (%)**
SVOP	3.84473(2)	N/A	7.015
0.1Mn-SVOD	3.84736(4)	0.00(3)	16.400
0.2Mn-SVOD	3.86581(6)	0.24(2)	12.752
0.3Mn-SVOD	3.88787(9)	0.03(6)	12.344

The TGA curves for 0.1Mn-SVOD and 0.2Mn-SVOD have a very similar shape to those of the Ca substituted samples. Onset of rapid oxidation temperature is increased to near maximum temperature (982.3°C and 1004.9°C respectively) for 0.1Mn-SVOD and 0.2Mn-SVOD. The TGA curves also lack the distinct first stage of oxidation, similar to the Ca substituted samples. Neither sample exhibits oxidation tailing off at the end of the scan. The 0.3Mn-SVOD sample has much more resemblance to the pure SVOD though it lacks a distinct first stage of oxidation. The sample rapidly oxidizes at an even faster rate than the SVOD sample immediately after evaporating chemioabsorbed water. Mass gain also tails off near high temperature with a similar net mass gain (3.5%).

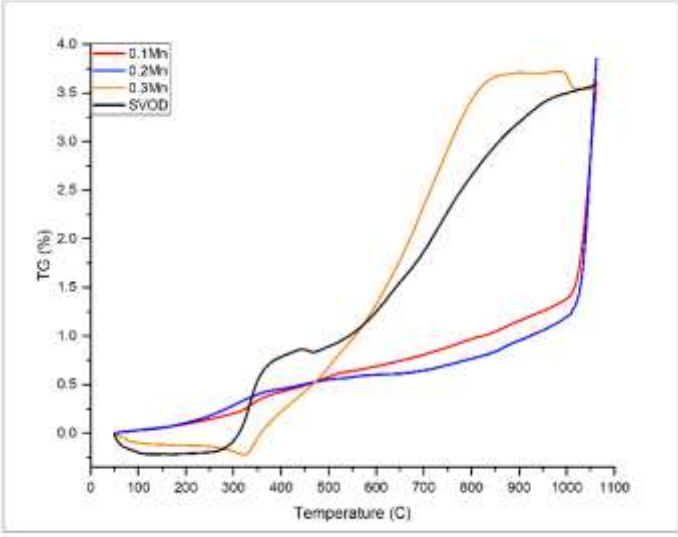

Figure 4.13 TGA Results of Mn Substituted Strontium Vanadate

Table 4.13 TGA Data-points for Mn Substituted Strontium Vanadate

Substitution Level	Onset of 1st Stage Oxidation (°C)	Onset of 2nd Stage Oxidation (°C)	Peak Oxidation Rate (%Change/min)
x = 0.00	290.5	421.4	0.0822
x = 0.10	N/A	982.3	0.5467
x = 0.20	N/A	1004.9	0.8093
x = 0.30	323.5	425.6	0.110

All of the Mn substituted samples have decreased electrical conductivity though they still displayed metallic conductivity behavior. In the case of the 0.1Mn-SVOD and 0.2Mn-SVOD samples, the decrease in conductivity was by multiple orders of magnitude dropping below 1S/cm. The 0.3Mn-SVOD sample's decrease was more modest only dropping to 26.7S/cm at room temperature.

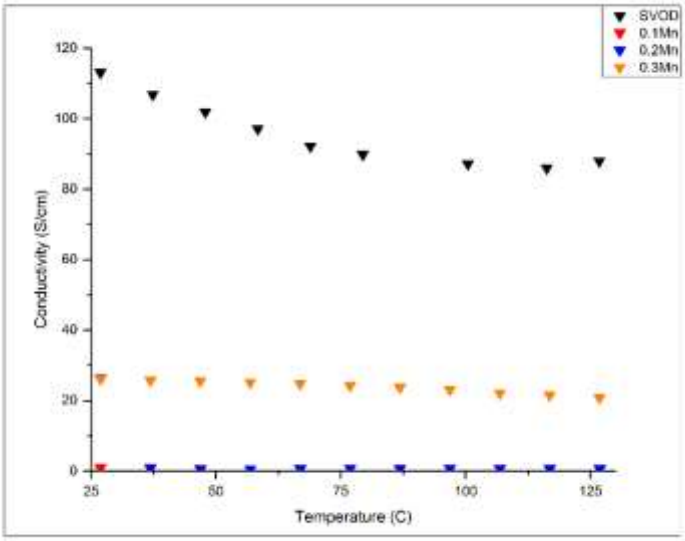

Figure 4.14 Electrical Conductivity of Mn Substituted Strontium Vanadate

4.3.3.2 Titanium

The titanium samples also have a distinct feature when it comes to phase composition. Strontium titanate ($SrTiO_3$) is one of the more common cubic perovskite oxides. In the case of Ti substitution for V in $SrVO_3$ the Ti often forms its own separate phase. In fact, for all but the 0.4Ti-SVOD sample, the XRD patterns showed three distinct peaks corresponding to $SrVO_3$, $SrTiO_3$, and a substitutional phase. The 0.4Ti-SVOD pattern showed a broader singular peak with the substitutional phase as a majority phase, but this sample still achieved the best fit when modeled with the three phases. As observed in Table 4.14, there is an increasing presence of $SrTiO_3$ as the Ti dosage is increased. However, the trend is broken for the 0.4 level sample. The 0.2Ti-SVOD sample XRD pattern shown in Figure 4.17 shows the three distinct peaks corresponding to the three phases. For all samples but the 0.4Ti-SVOD sample, there was also a substantial amount of pure strontium vanadate remaining, particularly in the 0.2Ti-SVOD sample. The amount of strontium consumed in the reaction by this pure phase means that the substitutional phase contains much higher amounts of titanium than prescribed. As observed in Table 4.14, all of the samples except for 0.1Ti-SVOD have B-site cation mixtures near 50:50 for

the vanadium and titanium. It should be noted that it is difficult to distinguish Ti from V in the perovskite structure using X-rays. This difficulty arises because Ti and V have similar atomic scattering factors for X-rays, leading to only subtle differences in their contribution to diffraction intensities. As a result, distinguishing between Ti and V occupancy in a Rietveld refinement of a perovskite structure can be challenging, especially when both elements occupy the same crystallographic site. For this reason, other methods must be used to confirm the inhomogeneity of Ti distributed in the sample. EDS of the samples showed that the Ti-content varied across the sample surface. For example, Figure 4.15 is a representative SEM image of 0.2Ti-SVOD, and Figure 4.16 shows the EDS results of the scan across line 4 and line 5 in Fig. 4.15. It is observed that the increase in Ti content across line 4 is accompanied with a decrease in V content and vice versa. In contrast, the Ti content across line 5 is relatively uniform despite slightly higher counts near grain boundaries, indicating Ti segregation to the grain boundaries. The EDS results support the inhomogeneous phase distribution suggested by the Rietveld modeling results.

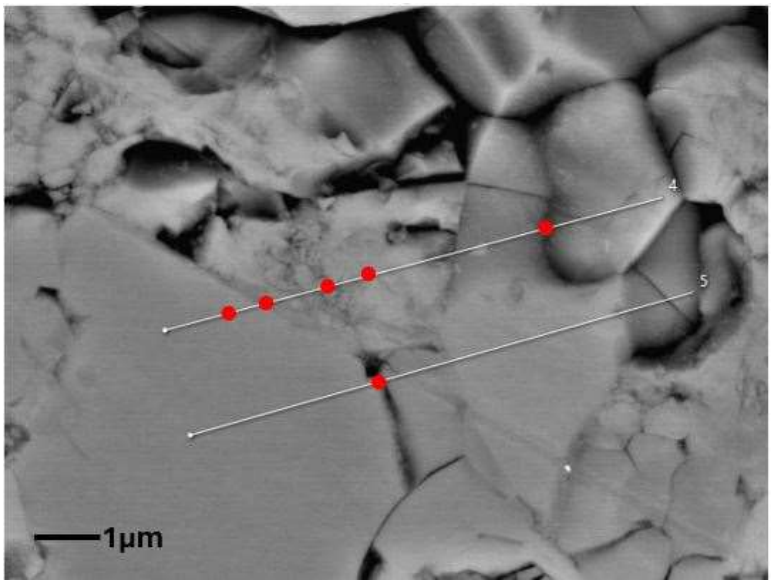

Figure 4.15 SEM Image of 0.2Ti-SVOD with EDS lines cans. Red dots mark inflection points in V:Ti ratio marked by dashed lines in Figure 4.16.

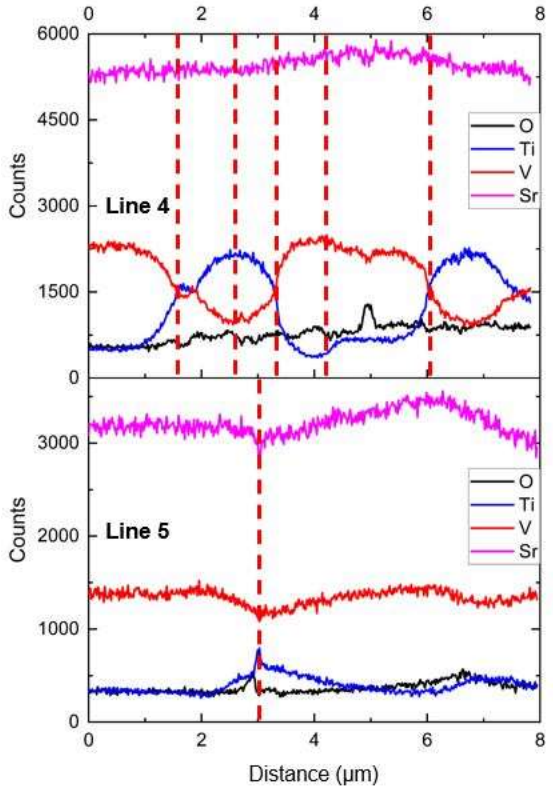

Figure 4.16 EDS line scans showing varying Ti content across the surface of 0.2Ti-SVOD. Red dashed lines are marked in relation to V:Ti ratio (5:1, 1:1, 1:5)

Table 4.14 Phase Composition (wt%) of Ti Substituted Strontium Vanadate Solid Samples

Sample	Pure $SrVO_3$ wt%	$Sr_3V_2O_8$ wt%	Ti-Substituted $SrVO_3$ wt%	$SrTiO_3$ wt%
SVOP	73.6	26.4	N/A	N/A
0.1Ti-SVOD	53.1	N/A	42.5	4.4
0.2Ti-SVOD	67.8	N/A	23.1	9.1
0.3Ti-SVOD	57.2	N/A	30.9	11.9
0.4Ti-SVOD	29.9	N/A	62.5	7.6

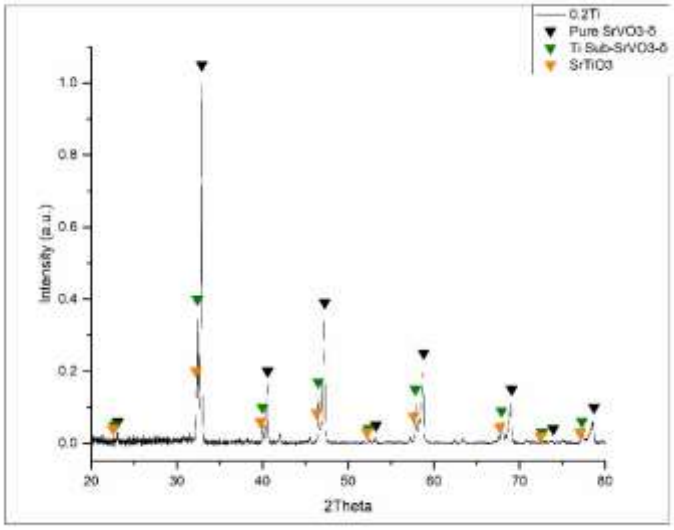

Figure 4.17 XRD Pattern of Ti Substituted Strontium Vanadate (0.2Ti-SVOD)

Table 4.15 Structural Parameters of Ti Substituted Strontium Vanadate Solid Samples

Sample	**Lattice Parameter (Å)**	**Ti-Occupancy**	**R_{wp} (%)**
SVOP	3.84473(2)	N/A	7.015
0.1Ti-SVOD	3.85352(16)	0.1(2)	10.522
0.2Ti-SVOD	3.89506(13)	0.450(6)	9.750
0.3Ti-SVOD	3.8804(3)	0.50(4)	9.070
0.4Ti-SVOD	3.87357(9)	0.54(9)	6.564

The only sample which has the distinct two step oxidation behavior similar to SVOD is the 0.4Ti-SVOD sample which shows the initial oxygen deficiency filling starting at 113.2°C, which is lower temperature than the pure sample. The 0.2Ti-SVOD sample experiences mass loss up to 350°C which is attributed to evaporation of chemioabsorbed water. However, after 350°C , 0.2Ti-SVOD has rapid mass gain similar to the 0.4Ti-SVOD sample. The 0.4Ti-SVOD sample still gains more mass even accounting for the mass loss by the 0.2Ti-SVOD sample (-0.59% mass loss). The TGA curves for the 0.1Ti-SVOD and 0.3Ti-SVOD samples instead show a very gentle slope with minimal mass gain (1.69% and 1.94% respectively).

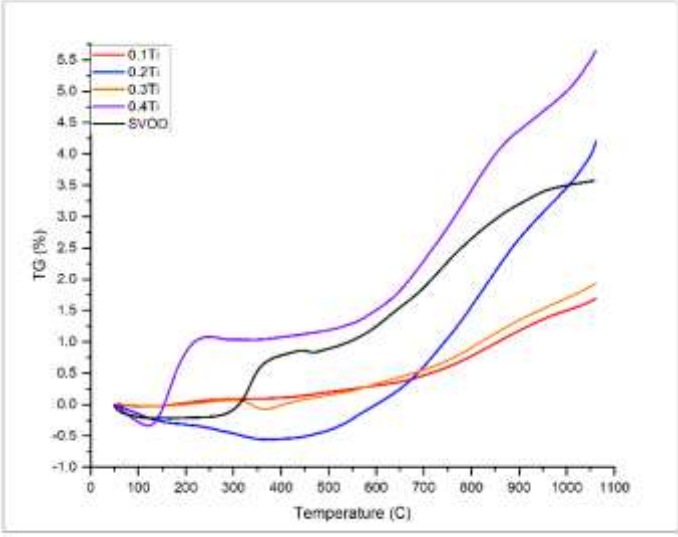

Figure 4.18 TGA Results of Ti Substituted Strontium Vanadate

Table 4.16 TGA Data-points for Ti Substituted Strontium Vanadate

Substitution Level	Onset of 1st Stage Oxidation (°C)	Onset of 2nd Stage Oxidation (°C)	Peak Oxidation Rate (%Change/min)
x = 0.00	290.5	421.4	0.0822
x = 0.10	N/A	N/A	0.0383
x = 0.20	N/A	417.4	0.1070
x = 0.30	N/A	N/A	0.0442
x = 0.40	113.2	561.7	0.1199

All samples except for the 0.2Ti-SVOD sample have decreased electrical conductivity. The 0.1Ti-SVOD sample has conductivity very similar to the pure sample with RT value of 95.9S/cm. The 0.4Ti-SVOD level sample has conductivity of 45.7S/cm. The 0.3Ti-SVOD sample exhibits conductivity decreased by two orders of magnitude. Conductivity drops all the way to 2.6S/cm for this sample. The large decrease in conductivity supports the Rietveld model for 0.3Ti-SVOD showing it as having the highest content of strontium titanate which is an insulative material. There is a large increase in conductivity for the 0.2Ti-SVOD sample (1263.4S/cm).

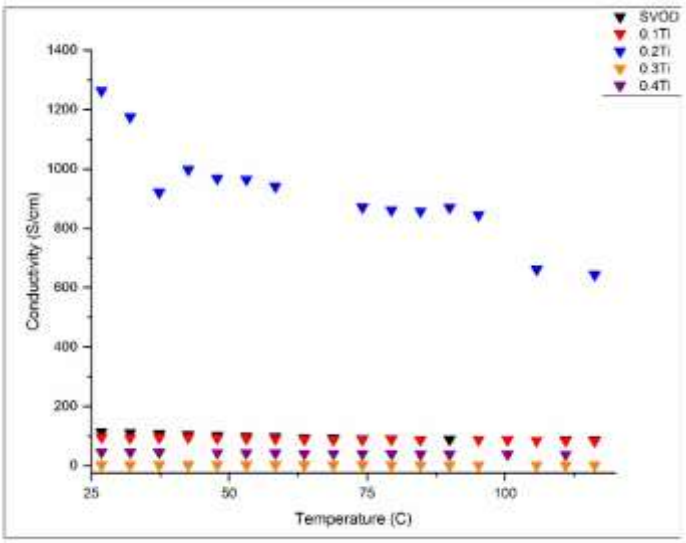

Figure 4.19 Electrical Conductivity of Ti Substituted Strontium Vanadate

4.3.4 Dual Site Substitution

4.3.4.1 Calcium and Titanium

The dual substitution samples with calcium replacing strontium and titanium replacing vanadium had features distinct from the individually substituted samples. In the (0.1Ca+0.1Ti)-SVOD sample, the integration of the calcium atom is less successful than the individual Ca substitution cases as evidenced by the low occupancy (0.03), 30% of the prescribed value. This contrasts with the (0.2Ca+0.1Ti)-SVOD model which showed Ca occupancy (0.22) within range of the prescribed value. On the other hand, the titanium substitute integrates well in the (0.1Ca+0.1Ti)-SVOD sample, but in the (0.2Ca+0.1Ti)-SVOD sample there was no integration of Ti. In fact, it appears most of, if not all, the titanium instead formed a secondary strontium titanate phase (18.7wt%). The substitutional occupancies are reflected in the lattice parameter as the (0.1Ca+0.1Ti)-SVOD sample has an expanded lattice (3.88064Å) but the increased occupancy of Ca and the lack of integration of Ti in (0.2Ca+0.1Ti) works to decrease this value (3.85814Å).

Table 4.17 Phase Composition (wt%) of (Ca+Ti) Dual Substituted Strontium Vanadate Solid Samples Compared to Individually Substituted Samples

Sample	**$SrVO_3$ wt%**	**$Sr_3V_2O_8$ wt%**	**$SrTiO_3$ wt%**
0.1Ca-SVOD	96.4	3.6	N/A
0.1Ti-SVOD	92.3	N/A	7.7
0.2Ca-SVOD	97.1	2.9	N/A
(0.1Ca+0.1Ti)-SVOD	100	N/A	N/A
0.2Ca+0.1Ti)-SVOD	81.3	N/A	18.7

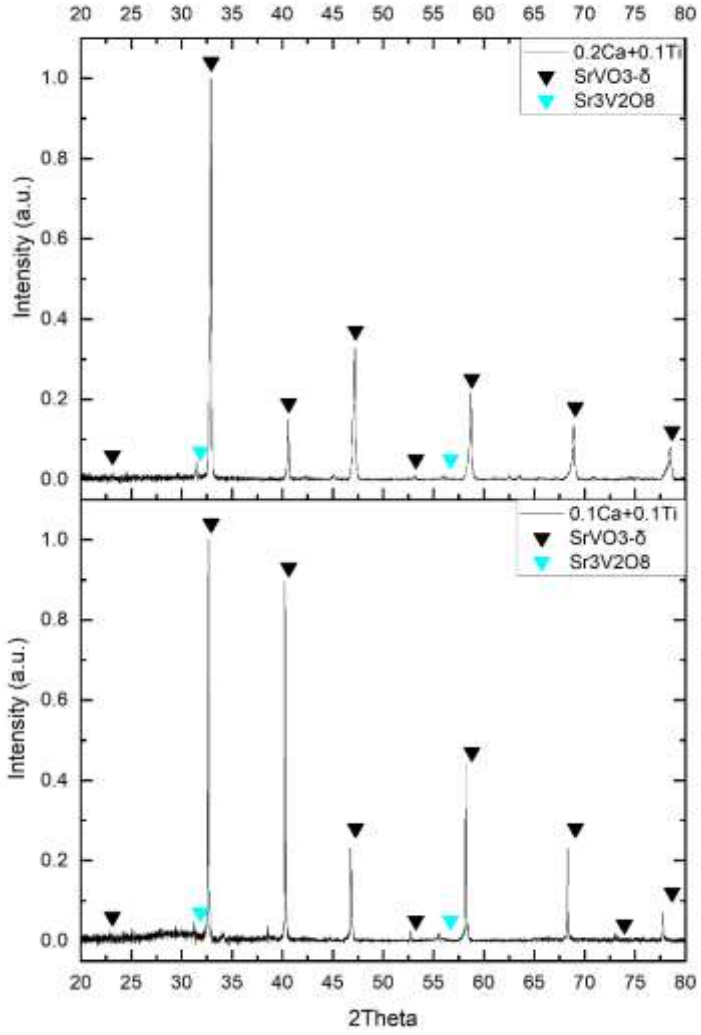

Figure 4.20 XRD Patterns of (Ca+Ti) Dual Substituted Strontium Vanadate Solid Samples. (0.1Ca+0.1Ti)-SVOD (lower) and (0.2Ca+0.1Ti)-SVOD (upper).

Table 4.18 Structural Parameters of (Ca+Ti) Dual Substituted Strontium Vanadate Solid Samples Compared to Individually Substituted Samples

Sample	Lattice Parameter (Å)	Ca-Occupancy	Ti-Occupancy	R_{wp} (%)
SVOP	3.84473(2)	N/A	N/A	7.015
0.1Ca-SVOD	3.847183(18)	0.08(3)	N/A	8.304
0.1Ti-SVOD	3.85352(16)	N/A	0.1(2)	10.522
0.2Ca-SVOD	3.837236(14)	0.21(2)	N/A	7.000
(0.1Ca+0.1Ti)-SVOD	3.88064(5)	0.03(4)	0.1(5)	13.080
(0.2Ca+0.1Ti)-SVOD	3.85814(14)	0.220(16)	0.00(12)	12.385

The (0.2Ca+0.1Ti)-SVOD sample has a distinct first stage of oxidation similar to SVOD as seen in the inset of Figure 4.21. The (0.1Ca+0.1Ti)-SVOD sample on the other hand has no distinct first stage and instead gently increases mass until rapidly gaining mass near the maximum temperature. Both samples display the latter behavior, and it is quite different from the individually Ti substituted samples. This quality is the influence of the Ca substitute. Neither of the dual substituted samples' TGA curves show onset of rapid oxidation temperature (961.4°C and 952.3°C respectively) as high as the curves of the individual Ca substituted samples.

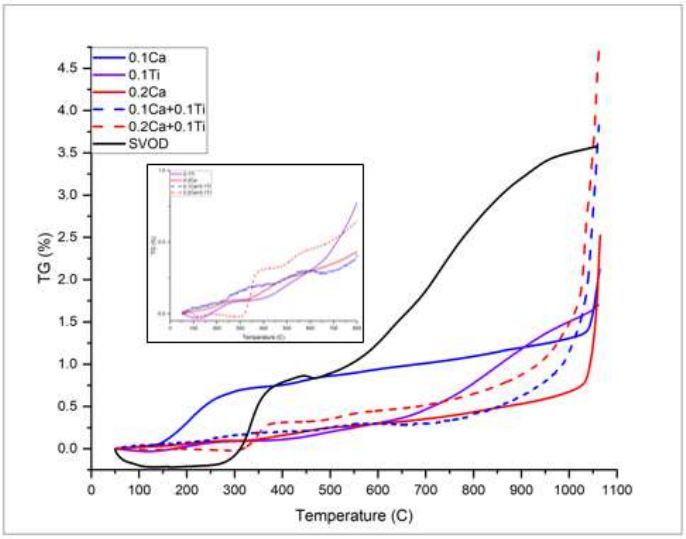

Figure 4.21 TGA Results of (Ca+Ti) Dual Substituted Strontium Vanadate Compared to Individually Substituted Samples. Zoomed in on First Stage Oxidation (inset).

Table 4.19 TGA Data-points of (Ca+Ti) Dual Substituted Strontium Vanadate Compared to Individually Substituted Samples

Substitution Level x is Ca and y is Ti	Onset of 1st Stage Oxidation (°C)	Onset of 2nd Stage Oxidation (°C)	Peak Oxidation Rate (%/min)
x = 0.0 y = 0.0	290.5	421.4	0.0822
x = 0.1 y = 0.0	115.5	1010.9	0.3702
x = 0.0 y = 0.1	N/A	N/A	0.0383
x = 0.2 y = 0.0	N/A	1011.9	0.9459
x = 0.1 y = 0.1	N/A	961.4	0.8026
x = 0.1 y = 0.2	308.4	952.3	0.8127

The samples have conductivities very similar to both the pure SVOD and 0.1Ti-SVOD samples with RT conductivities of 150.3S/cm and 128.9S/cm respectively for (0.1Ca+0.1Ti)-SVOD and (0.2Ca+0.1Ti)-SVOD. The decrease observed in the (0.2Ca+0.1Ti)-SVOD sample is likely due to the strontium titanate formation as seen in Table 4.17.

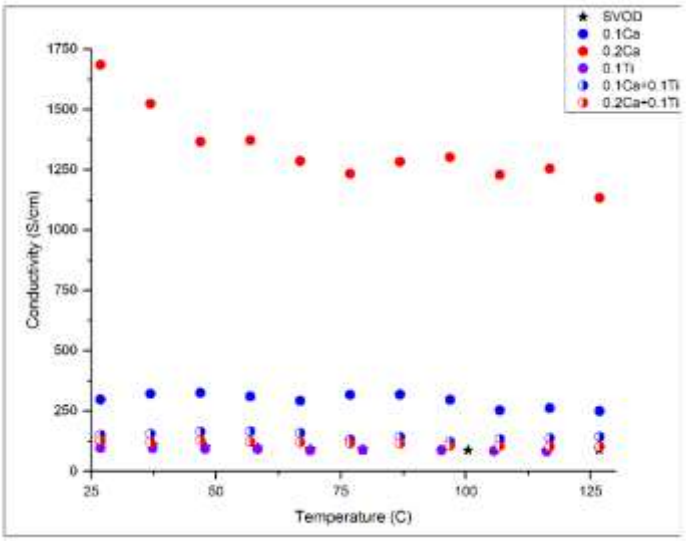

Figure 4.22 Electrical Conductivity of (Ca+Ti) Dual Substituted Strontium Vanadate Solid Samples Compared to Individually Substituted Samples

4.3.4.2 Barium and Manganese

The dual substituted samples with barium substituted for strontium and manganese substituted for vanadium show similar results to the samples individually substituted with manganese. The (0.1Ba+0.1Mn)-SVOD model shows good integration of the cation

replacements with minimal (11wt%) secondary phase observed upon sintering. The occupancies of the barium and manganese atoms are very close to the 0.1 level prescribed (0.12 and 0.09 respectively). The lattice parameter (11.87782Å) is larger than either of the individual substitutions. The additional Mn in the (0.1Ba+0.2Mn)-SVOD sample results in a multitude of secondary phases. The most abundant secondary phase was closely matched to a Mn based phase ($Sr_7Mn_4O_{15}$) which had been observed in the 0.3Mn-SVOD sample as well. The extensive decomposition of the phase purity leaves a small amount of cubic perovskite oxide phase (36.2wt%) though it does remain the primary phase of the mixture. Issues in fitting all of the secondary peaks led to the increase to the R-factor of the Rietveld model.

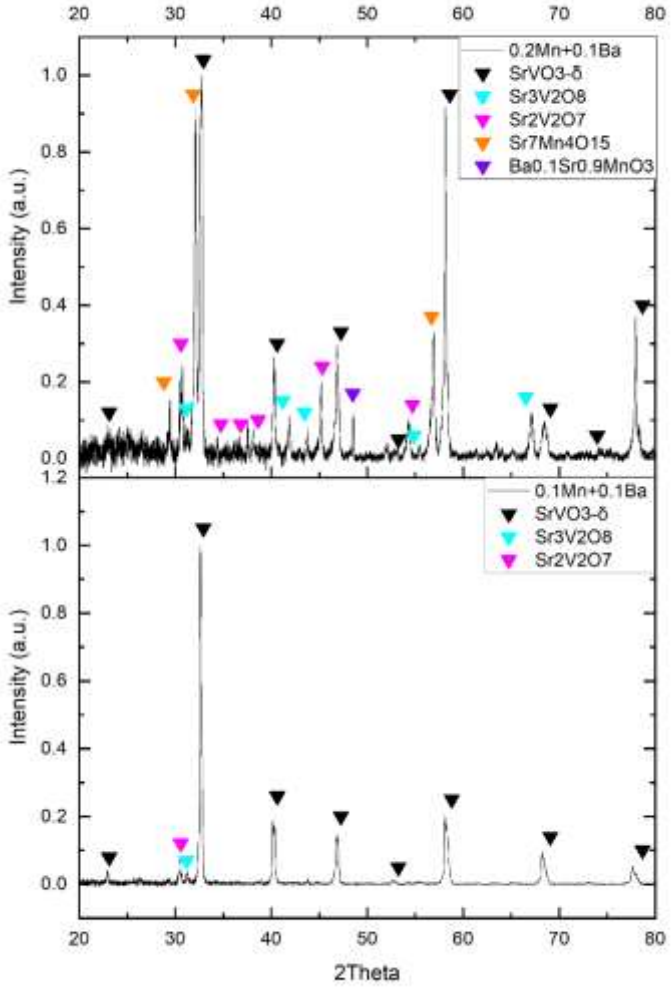

Figure 4.23 XRD Patterns of (Ba+Mn) Dual Substituted Strontium Vanadate Solid Samples. (0.1Ba+0.1Mn)-SVOD (lower) and (0.1Ba+0.2Mn)-SVOD (upper).

Table 4.20 Structural Parameters of (Ba+Mn) Dual Substituted Strontium Vanadate Solid Samples Compared to Individually Substituted Samples

Sample	**Lattice Parameter (Å)**	**Ba-Occupancy**	**Mn-Occupancy**	**R_{wp} (%)**
SVOP	3.84473(2)	N/A	N/A	7.015
0.1Ba-SVOD	3.854247(9)	0.12(4)	N/A	15.507
0.1Mn-SVOD	3.84736(4)	N/A	0.00(3)	16.400
0.2Mn-SVOD	3.86581(6)	N/A	0.24(2)	12.752
(0.1Ba+0.1Mn)-SVOD	3.87782(4)	0.121(5)	0.094(11)	11.379
(0.1Ba+0.2Mn)-SVOD	3.87557(15)	0.13(5)	0.01(16)	15.935

The two samples have extremely different oxidation patterns. The (0.1Ba+0.1Mn)-SVOD sample has a distinct first step in oxidation at a slightly decreased temperature (269.3°C) compared to SVOD and similarly starts rapidly oxidizing at slightly elevated temperature (544.6°C) eventually tailing off in mass gain before max temperature. The (0.1Ba+0.2Mn)-SVOD sample, on the other hand, does not have a first oxidation step. The sample begins to rapidly oxidize at slightly higher temperature (520.9°C) than SVOD before tailing off in mass gain at even lower temperature (857.3°C) than SVOD. (0.1Ba+0.2Mn)-SVOD has a net mass gain below 3%. The lack of first oxidation step combined with the low overall mass gain is indicative of the multitude of secondary phases and the poor reduction to the cubic perovskite oxide phase.

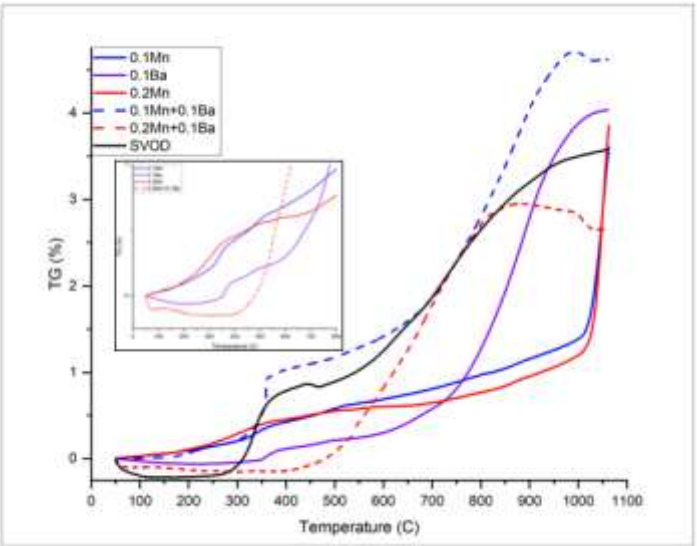

Figure 4.24 TGA Results of (Ba+Mn) Dual Substituted Strontium Vanadate Compared to Individually Substituted Samples. Zoomed in on First Stage Oxidation (inset).

Table 4.21 TGA Data-points of (Ba+Mn) Dual Substituted Strontium Vanadate Compared to Individually Substituted Samples

Substitution Level x is Ba and y is Mn	Onset of 1st Stage Oxidation (°C)	Onset of 2nd Stage Oxidation (°C)	Peak Oxidation Rate (%/min)
x = 0.0 y = 0.0	290.5	421.4	0.0822
x = 0.1 y = 0.0	322.4	742.7	0.1620
x = 0.0 y = 0.1	N/A	982.3	0.5467
x = 0.0 y = 0.2	N/A	1004.9	0.8093
x = 0.1 y = 0.1	269.3	544.6	0.1224
x = 0.1 y = 0.2	N/A	520.9	0.0932

The (0.1Ba+0.1Mn)-SVOD sample has a slight increase to electrical conductivity (RT 136.4°C) while the (0.1Ba+0.2Mn)-SVOD sample has an immense decrease by orders of magnitude. The conductivity of (0.1Ba+0.2Mn)-SVOD is very similar to the 0.1Mn-SVOD and 0.2Mn-SVOD samples.

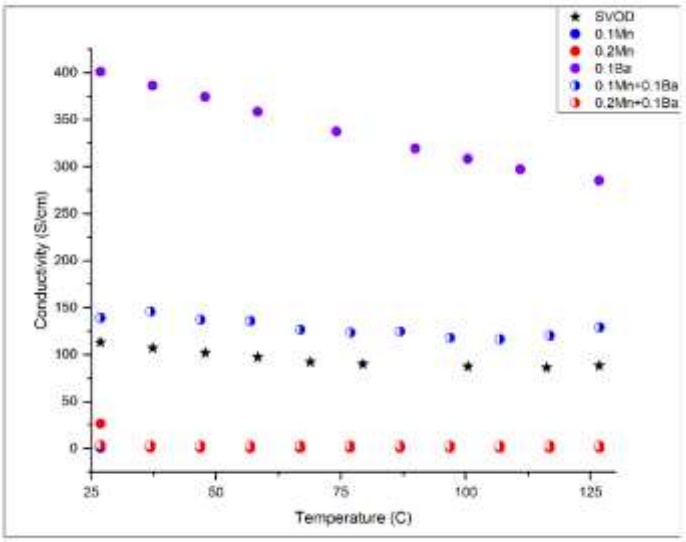

Figure 4.25 Electrical Conductivity of (Ba+Mn) Dual Substituted Strontium Vanadate Solid Samples Compared to Individually Substituted Samples

4.4 Discussion

4.4.1 Substitution at Sr Site

As previously discussed, substitutions at the cation sites in the cubic perovskite structure can be viewed through the lens of its tolerance factor, which describes the fit between A- and B-site cations of different sizes. The pure strontium vanadate has a tolerance factor near unity (1.011), indicating a great fit, but the introduction of the calcium and barium substitutions distort the fit. A full calcium for strontium substitution would drop the value down to 0.975, representing a 3.5% drop, while the barium substitute would increase the value to 1.07, representing a 5.9% increase. Both of these are in the acceptable range, though barium is approaching the limit. Within the context of this study, the shift is not as large as the substitutions presented are only partial. The changes to the tolerance factor are reflected by the calcium and barium substitute samples in which the calcium substitute shows more consistent integration into the lattice. Powder processing for both substitutions left large amounts (>40wt%) of strontium orthovanadate as is expected due to the slow kinetics of the reduction reaction. The remaining amount of orthovanadate was not found to be a result of increased substitutional dosage, and proximity to the hydrogen gas source in the high temperature furnace was also not correlated with powder phase purity. After sintering in SPS, both the calcium and barium samples experienced further progression of the reduction reaction due to the high heating temperature and the carbothermal reduction environment provided by SPS tooling. For the Ca substitute samples, this progression resulted in the formation of samples comprised of >95% cubic perovskite oxide phase. The effect of the calcium substitute, which has a reduced ionic radius compared to strontium (134<144pm), was immediately observed in the shifting of the (110) peak (primary) for the 0.2Ca-SVOD and 0.3Ca-SVOD samples (SVOD meaning strontium vanadate disc). This corresponded to a decrease in the lattice parameter by 0.007Å and 0.017Å, respectively. The 0.1Ca-SVOD sample has a slightly increased lattice parameter but this can be

explained by the fact that (1) not all of the prescribed Ca was integrated into the lattice (2) the 0.1Ca-SVOP (SVOP meaning strontium vanadate powder) had the most remaining unreacted orthovanadate and thus would likely have the most remaining secondary phases which could restrict the contraction of the lattice. The 0.4Ca-SVOD sample differed from the other three in that Ca occupancy did not increase and in fact there was a decrease down to 0.1Ca-SVOD levels. The diffraction pattern of this sample indicated that a distinct calcium vanadate phase ($CaVO_3$) had formed in the amount of 37.6wt%. This was in good agreement with the amount of Ca that was not integrated into the lattice. This demonstrates that for the calcium substitution there is a solubility limit near 30% substitution for the solid-state powder reaction technique used.

The 0.1Ca-SVOD sample experienced the first stage of oxidation at a lower temperature than pure SVOD but then proceeded to oxidize at a slower rate until hitting rapid oxidation at a higher temperature than SVOD. This suggests that the filling of oxygen vacancies is most directly controlled by the lattice size and not necessarily the framework cations, though second stage oxidation is more directly influenced by the framework cations. The latter point is reenforced by the 0.2Ca-SVOD and 0.3Ca-SVOD samples. Both samples TGA curves show extremely reduced rates of oxidation compared to pure SVOD, but 0.2Ca-SVOD does finally hit rapid oxidation before the max temperature. Also noteworthy is that the 0.4Ca-SVOD sample has greater mass gain than the 0.3Ca-SVOD sample which would suggest lattice size has some contribution to the delay in second stage as well though this cannot be detangled from the large amount of $CaVO_3$ present in the 0.4Ca-SVOD sample. The onset of rapid oxidation was well correlated with substitution level (Figure 4.26) with a Pearson coefficient of 0.750.

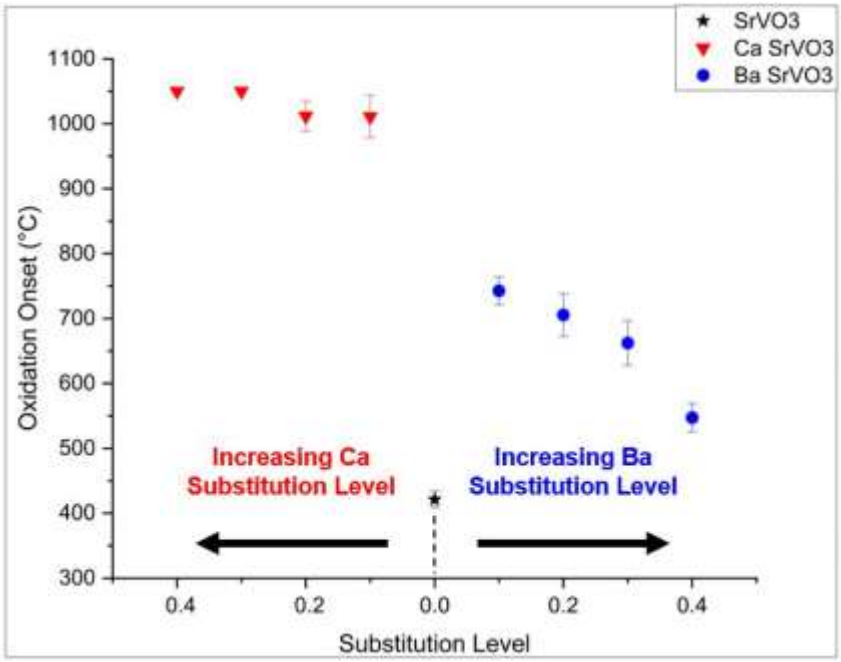

Figure 4.26: Effect of Substitution Level of Sr site Substitutes on Oxidation Onset Temperature.

The barium substitute results in an increase to lattice size as predicted, though the integration of the Ba substitute was not as prescribed for 0.2Ba-SVOD and 0.3Ba-SVOD in terms of the occupancies returned from the Rietveld model. The 0.2Ba-SVOD sample had occupancy higher than 0.2 and the 0.3Ba-SVOD sample had occupancy lower than 0.3. The changes to the oxidation behavior in conjunction with the changes to the lattice parameter for the Ca substituted samples suggested that the first stage of oxidation was controlled by the lattice size. However, this is contradicted by the analysis of the oxidation behavior and lattice parameters of the Ba substitute samples. The Ba substitute samples have larger lattice parameters than pure SVOD and yet only 0.4Ba-SVOD has its first oxidation stage onset before pure SVOD (219.9°C). There is a negative correlation between substitution level and oxidation onset for the Ba substituted samples (Pearson coefficient -0.951).

The PPMS data for the Ca substituted samples is shown in Figure 4.27. The 0.1Ca-SVOD sample has a slight increase in conductivity while the 0.2Ca-SVOD, 0.3Ca-SVOD, and 0.4Ca-

SVOD samples all have an increase to conductivity by greater than an order of magnitude. The decrease in conductivity from 0.3Ca-SVOD to 0.4Ca-SVOD is attributed to the $CaVO_3$ content, which is known to be insulative unless it exists with oxygen vacancies [16], [23], [24]. The data shows a strong positive correlation between substitution level and conductivity with a Pearson coefficient of 0.930. The increased stability and conductivity of the Ca substituted $SrVO_3$ runs contrary to the DFT findings of Ma et al. who only recommended La and Y as A-site replacements in the strontium vanadate system for the design of low work function materials. However, while their forecasts did show Ca substitution decreasing stability, it was the smallest decrease in stability they predicted (aside from their recommended replacements). Furthermore, their work did show that at a higher dose (0.5) they'd predict Ca substitution to help lower the work function [8]. The present work demonstrates that the contribution of calcium to the electronic state increases the electrical conductivity. This could be indicative the contribution also works to lower the work function.

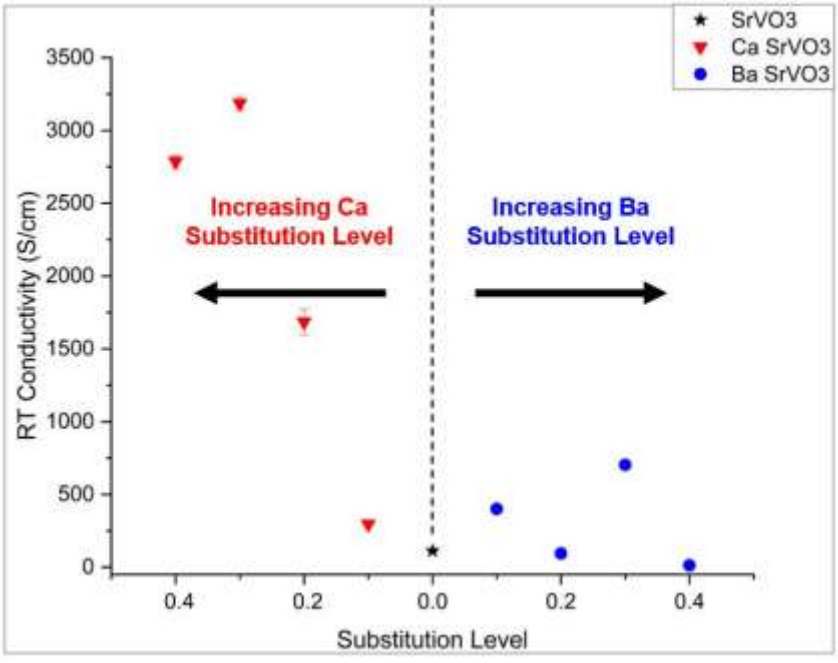

Figure 4.27: Effect of Substitution Level of Sr site Substitutes on Room Temperature Electrical Conductivity.

Conductivity is not well correlated with substitution level in the Ba substitute samples (Pearson coefficient 0.057). It has been reported that $BaVO_3$ has a metallic conductivity similar to that of $SrVO_3$ and thus it is expected that the Ba substitute could help enhance conductivity, but this structure is also typically formed under high pressure (15GPa) which is orders of magnitude higher than that which was used in this study [25]. The 0.1Ba-SVOD and 0.3Ba-SVOD samples, which had occupancies in the Rietveld models of 0.12 and 0.21 respectively, both have increased conductivity compared to the pure SVOD sample. However, the 0.2Ba-SVOD sample, with occupancy of 0.29, exhibited slightly decreased conductivity compared to pure SVOD. Sample 0.4Ba-SVOD, with occupancy of 0.33, has a dramatic decrease in conductivity by an order of magnitude. It is interesting to note the decrease in conductivity for the samples with higher Ba occupancy values in the Rietveld models, but no correlation between Ba content and conductivity can be concluded without further experimentation.

4.4.2 Substitution at V Site

Vanadium site substitution exhibited less predictable behavior, consistent with the varied nature of transition metals. This inconsistency in integration was reflected in the lack of correlation between the substitution levels and property changes for both the Ti and Mn substituted samples. Figure 4.28 shows the onset of rapid oxidation for these samples, and both sets of data have Pearson correlations near zero (0.136 and 0.013 for Ti and Mn, respectively). Figure 4.29 contains the room temperature electrical conductivity data. The Pearson coefficient for the Ti substitutes in this data set again is very low in magnitude (-0.067). The Mn conductivities have higher magnitude correlation with substitution level (-0.632) compared to the oxidation data.

Both of the substitutions for the B-site represented smaller deviations in ionic radius compared to the A-site replacements and thus the changes to the tolerance factor were also not as large. For titanium a decrease of 1.2% would be expected for the full substitution and for manganese a slightly larger increase of 2.6% would be expected; again, accounting for the partial substitutions here the changes would not even be this high. The difficulty in integrating both of these cation substitutions into the strontium vanadate structure is confounding, though less so for the titanium substitute. The manganese substitute could not be integrated past the 0.2 level (20% of vanadium atoms replaced). Additionally, the 0.1Mn-SVOD Rietveld model could not resolve manganese occupancy. This was a result of radical underestimation of peak intensity from the (200) plane. This is despite the Rietveld model of the 0.1Mn-SVOP which showed an acceptable fit (R-factor 8.634%) and showed Mn occupancy (0.15) near the nominally prescribed amount. The 0.2Mn-SVOD model shows a reasonable occupancy (0.24). The 0.3Mn-SVOD and 0.4Mn-SVOD samples, however, demonstrate severe phase breakdown. In these manganese substituted samples the Mn_2O_3 precursor not only fails to substitute for the V_2O_5 precursor, but also works to strip away both strontium and vanadium from their own precursors to form other secondary phases. This was evident from the XRD scans taken after hydrogen reduction and there was little to no improvement upon sintering in SPS. The main source of this instability is likely the manganese having more volatile mixed valence states as it was introduced into the system in a 3+ state and could be further influenced by the creation of oxygen vacancies during sintering. Lattice growth observed in the Mn substitute samples is consistent with the size differences between Mn in its 3+ and 4+ oxidation states (Mn is larger than V in a 3+ state but smaller in a 4+ state). The instability is further reflected by the stark difference in both oxidation behavior and electrical conductivity when comparing 0.2Mn-SVOD to 0.3Mn-SVOD. The TGA curves of

0.1Mn-SVOD and 0.2Mn-SVOD show the manganese substitute inducing lag to the oxidation reaction. The 0.2Mn-SVOD sample delays rapid oxidation to a higher temperature compared to SVOD. It is important to note with these samples, however, that they are still oxidizing much faster than either the Ca substitute samples or low dosage Ba substitute samples. With additional Mn dosage, the 0.3Mn-SVOD sample suddenly returns to oxidation behavior much closer to pure $SrVO_3$.

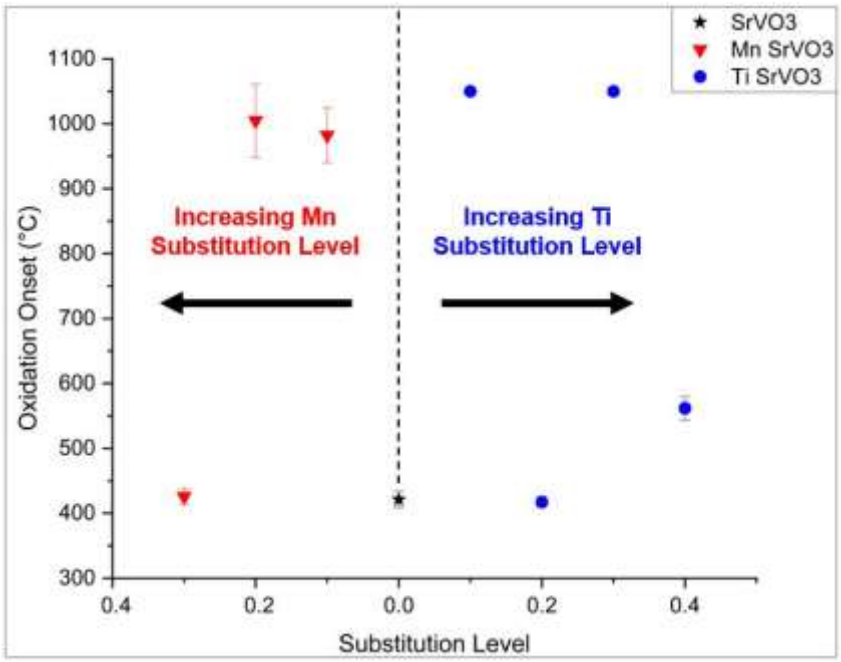

Figure 4.28: Effect of Substitution Level of V site Substitutes on Oxidation Onset Temperature.

The effects of titanium integration differ from those of manganese substitution. While there was some difficulty in achieving the desired substitutions of Ti, the XRD patterns of the resultant materials provided some clarity on the effects of Ti substitution. All but the 0.4Ti-SVOD sample showed three distinct peaks clustered together at the cubic perovskite planes with the smallest peak being the one further left (largest lattice). This was a clear indication there was formation of strontium titanate. Titanium is more stable in the perovskite structure compared to vanadium for a variety of reasons. It is more stable in its 4+ state as it loses its 4s and 3d

electrons leaving a full 3p subshell [12], [26]. The size of Ti also results in a tolerance factor closer to one for the perovskite structure. It is for these reasons Ti is viewed as an excellent substitutional candidate. The greater stability of Ti in the 4+ state influences the substitutional occupancy observed in these samples. The Rietveld refinement results indicate that the titanium dioxide precursor forms clusters during processing which create inhomogeneous $SrVO_3$ samples with higher Ti substitutional dosages than prescribed. The inhomogeneity also results in a large amount of vanadium pentoxide remaining to form pure $SrVO_3$. The effects of these formations were observed in both TGA and PPMS. Changes to the onset in rapid oxidation are shown in Figure 4.28. The 0.2Ti-SVOD sample has mass gain on par with the pure SVOD sample (though no first step oxidation is observed) and it has significantly higher conductivity than the rest of the Ti substituted samples. Though the magnitude of the conductivity is quite high, this should be attributed to the significant amount of pure $SrVO_3$ contained within the composite sample (10wt% more than any of the other samples). The 0.3Ti-SVOD sample has the highest amount of $SrTiO_3$ which explains both the lag in the mass gain profile as well as the extreme decrease in electrical conductivity ($SrTiO_3$ being an insulator) [27]. The inhomogeneity in phase constitution for these samples coupled with the weak correlations observed between property changes and substitution level serve as evidence that Ti is an unreliable cation substitute for V.

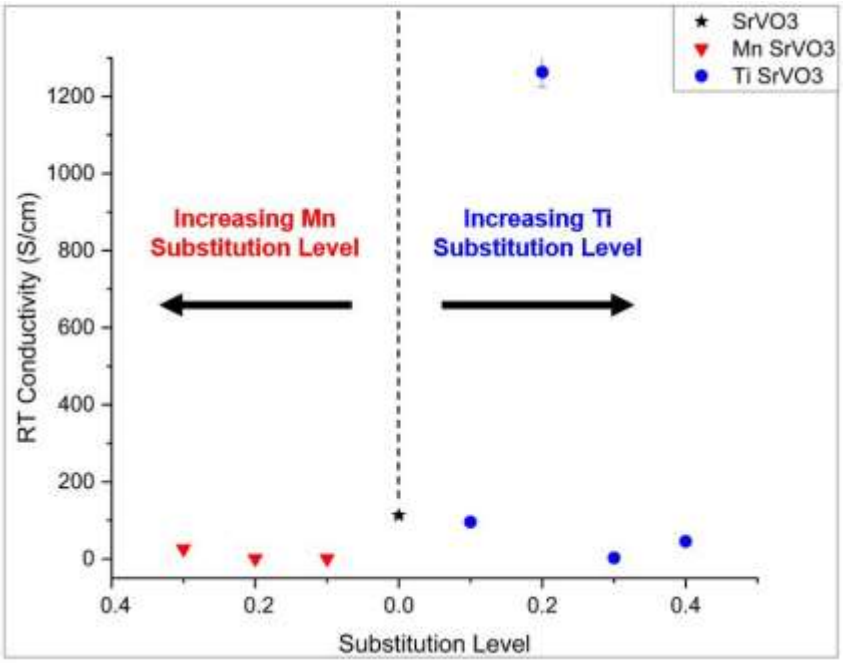

Figure 4.29: Effect of Substitution Level of V site Substitutes on Room Temperature Electrical Conductivity.

In the case of electrical conductivity for the Mn substituted samples, there is a clear difference between the lower-level substitution samples (0.1Mn-SVOD and 0.2Mn-SVOD) and the higher-level substitution 0.3Mn-SVOD sample. Qualitatively, this is similar to the difference observed in the XRD and TGA data. The 0.1Mn-SVOD and 0.2Mn-SVOD samples' conductivities dropped by orders of magnitude whereas the 0.3Mn-SVOD sample still possesses modest conductivity (26.7S/cm). The refinement results show little to no integration of Mn into the structure in the 0.3Mn-SVOD sample. Therefore, the decrease in conductivity for 0.3Mn-SVOD is attributed to the large amount of secondary phase formation (>60wt%). Without more substantial evidence of integration into the structure (only the 0.2Mn-SVOD model showed Mn occupancy) conclusions about the effect of Mn substitution on strontium vanadate cannot be made.

4.4.3 Dual Substitution

The samples with dual substitutions exhibited some changes in properties which were consistent with qualitative predictions based on the results of the individual substitutions. However, the property changes were not cumulative as none of the dual substitution samples outperformed the best individually substituted samples, as shown in Tables 4.22 and 4.23. For the (0.1Ca+0.1Ti)-SVOD samples the added rigidity from the Ti substitution resulted in lack of integration for the Ca atom. With an additional dose of calcium, integration is successful, but this structure is then rejected by the titanium substitute in favor of its own phase. Both samples TGA curves showed a delay to the onset of rapid oxidation compared to SVOD, but neither achieved as much delay as the individually Ca substituted samples. The fact that the (0.2Ca+0.1Ti)-SVOD sample did not outperform the (0.1Ca+0.1Ti)-SVOD sample in this regard is unexpected. It is likely that the Rietveld model underestimated the Ca content in (0.1Ca+0.1Ti)-SVOD as evidenced by the increased conductivity of this sample. Still, because the (0.1Ca+0.1Ti)-SVOD cannot match the performance of the 0.1Ca-SVOD in terms of oxidation delay, it seems fair to say that the Ti is inhibiting the positive effects of Ca on the oxidation behavior. The samples show little improvement to the electrical conductivity and overall they demonstrate the Ca substitution overcoming whatever barriers the Ti substitution puts up (be it impeding the conduction path in the native material or acting as an insulative composite). This is in fact showing combined effects just not in a way conducive to thermionic emission.

Table 4.22 Qualitative Changes to Properties for Individually Cation Substituted Strontium Vanadate

Individual Substitute	Thermal Stability Change	Electrical Conductivity Change
Ca	↑	↑
Ba	↑	↑
Mn	↑	↓
Ti	↑	↓

Table 4.23 Predicted and Observed Qualitative Changes to Properties for Dual Substituted Strontium Vanadate

Dual Substitute	Predicted Thermal Stability Change	Observed Thermal Stability Change	Predicted Electrical Conductivity Change	Observed Electrical Conductivity Change
0.1Ca+0.1Ti	↑	↑	↑	↑
0.2Ca+0.1Ti	↑	↑	↑	↑
0.1Ba+0.1Mn	↑	--	↑	↑
0.1Ba+0.2Mn	↑	↑	↓	↓

The (Ba+Mn) samples showed little in terms of combined effects on properties. The (0.1Ba+0.1Mn)-SVOD sample has a resistance to oxidation on par with SVOD but was far exceeded by both the 0.1Ba-SVOD and 0.1Mn-SVOD samples. The dual sample did outperform SVOD and the 0.1Mn-SVOD sample with respect to electrical conductivity, but again this seems to be one substitute (Ba) making up ground for the negatives of another (the negative being the reduction in conductivity observed in the individually Mn substituted samples). The (0.1Ba+0.2Mn)-SVOD sample seems to be evidence of pushing substitutions too far. Given a full substitution the $BaMnO_3$ phase would be pushing the boundaries of the tolerance factor at 1.099. This is of course an overestimation given the partial substitutions but still this remains the largest deviation from one explored in the study and this is borne out by the phase breakdown in the (0.1Ba+0.2Mn)-SVOD sample. This of course led to degraded properties in terms of stability and conductivity.

4.5 Summary

Overall, the A-site replacement is very effective in improving material properties particularly in the case of the Ca substitution. There is very limited room to increase the size of

Sr site, given that Sr already puts the tolerance factor above the value of unity. However, transitional metallic elements with an ionic size smaller than Ba could avoid the increasing degradation with increasing dosage. In terms of electrical conductivity, the results from the Ca substitutions are evidence that the A-site can also significantly alter the electronic structure (while the B-site is often thought of as the main contributor). These samples showed an exciting jump forward for strontium vanadate in terms of thermal stability (>1000C) and conductivity (>3000S/cm at RT).

Study on both substitutions at the vanadium sites reveal that the valence state of the substitutional atoms plays an important role in the accommodation of the substitutes at the B site in the perovskite lattice structure. In the case of manganese, its possibility in both the 3+ and 4+ states was considered as a possible boon as they could offer d band electrons to further enhance electrical properties. However, it turned out the multiple valence states of Mn restrict its fitting into the V site. On the other hand, addition of Ti led to the formation of second phase $SrTiO_3$ or highly dosed mixed phases with nearly equal vanadium and titanium content. There was evidence that this could be beneficial to insulating the structure without completely sapping the material of its conductivity.

Dual substitution did not result in the hypothesized combination of beneficial effects. The (Ca+Ti) samples did perform better than the baseline material but could not outperform the individually Ca substituted samples. The (Ba+Mn) samples were unstable due the strain put on the lattice by the large change to cation sizes. The (0.1Ba+0.1Mn)-SVOD sample did have decent performance while the (0.1Ba+0.2Mn)-SVOD sample completely broke down. The latter result suggests that at least for the current cubic perovskite oxide ($SrVO_3$), a hard boundary for tolerance factor near 1.05 is advised.

References

[1] R. M. Jacobs, D. Morgan, and J. H. Booske, "Strontium vanadate: An ultra-low work function electron emission material," in *2015 IEEE International Vacuum Electronics Conference (IVEC)*, Apr. 2015, pp. 1–2. doi: 10.1109/IVEC.2015.7223772.

[2] R. M. Jacobs, D. Morgan, and J. H. Booske, "Doped strontium vanadate: Computational design of a stable, low work function material," in *2016 IEEE International Vacuum Electronics Conference (IVEC)*, Apr. 2016, pp. 1–2. doi: 10.1109/IVEC.2016.7561807.

[3] L. Lin *et al.*, "Demonstration of Low Work Function Perovskite SrVO3 Using Thermionic Electron Emission," *Advanced Functional Materials*, vol. 32, no. 41, p. 2203703, 2022, doi: 10.1002/adfm.202203703.

[4] M. S. Sheikh, L. Lin, R. Jacobs, D. Morgan, and J. Booske, "\mathbfSrVO_3 electron emission cathodes with stable, >250 mA/cm2 current density," in *2023 24th International Vacuum Electronics Conference (IVEC)*, Apr. 2023, pp. 1–2. doi: 10.1109/IVEC56627.2023.10157940.

[5] M. S. Sheikh, R. Jacobs, D. Morgan, and J. Booske, "Time dependence of SrVO3 thermionic electron emission properties," *Journal of Applied Physics*, vol. 135, no. 5, p. 055104, Feb. 2024, doi: 10.1063/5.0186012.

[6] R. M. Jacobs, D. Morgan, and J. H. Booske, "Perovskite oxides: New candidate materials for low work function electron emitters," in *IEEE International Vacuum Electronics Conference*, Monterey, CA, USA: IEEE, Apr. 2014, pp. 133–134. doi: 10.1109/IVEC.2014.6857525.

[7] R. Jacobs, J. Booske, and D. Morgan, "Understanding and Controlling the Work Function of Perovskite Oxides Using Density Functional Theory," *Advanced Functional Materials*, vol. 26, no. 30, pp. 5471–5482, 2016, doi: 10.1002/adfm.201600243.

[8] T. Ma, R. Jacobs, J. Booske, and D. Morgan, "Discovery and engineering of low work function perovskite materials," *Journal of Materials Chemistry C*, vol. 9, no. 37, pp. 12778–12790, 2021, doi: 10.1039/D1TC01286J.

[9] L. Lin, R. Jacobs, T. Ma, D. Chen, J. Booske, and D. Morgan, "Work Function: Fundamentals, Measurement, Calculation, Engineering, and Applications," *Phys. Rev. Appl.*, vol. 19, no. 3, p. 037001, Mar. 2023, doi: 10.1103/PhysRevApplied.19.037001.

[10] J. Macías, A. A. Yaremchenko, and J. R. Frade, "Redox transitions in strontium vanadates: Electrical conductivity and dimensional changes," *Journal of Alloys and Compounds*, vol. 601, pp. 186–194, Jul. 2014, doi: 10.1016/j.jallcom.2014.02.148.

[11] J. Macías, A. A. Yaremchenko, and J. R. Frade, "Enhanced stability of perovskite-like SrVO3-based anode materials by donor-type substitutions," *J. Mater. Chem. A*, vol. 4, no. 26, pp. 10186–10194, Jun. 2016, doi: 10.1039/C6TA02672A.

[12] J. Macías, A. A. Yaremchenko, E. Rodríguez-Castellón, M. Starykevich, and J. R. Frade, "Compromising Between Phase Stability and Electrical Performance: SrVO3–SrTiO3 Solid Solutions as Solid Oxide Fuel Cell Anode Components," *ChemSusChem*, vol. 12, no. 1, pp. 240–251, 2019, doi: 10.1002/cssc.201801727.

[13] D. H. Jung, H. S. So, and H. Lee, "Structural and electrical properties of transparent conductor SrVO3 thin films grown using radio frequency sputtering deposition," *Journal of Vacuum Science & Technology A*, vol. 37, no. 2, p. 021507, Jan. 2019, doi: 10.1116/1.5054666.

[14] T. Maekawa, K. Kurosaki, and S. Yamanaka, “Physical properties of polycrystalline SrVO3−δ,” *Journal of Alloys and Compounds*, vol. 426, no. 1, pp. 46–50, Dec. 2006, doi: 10.1016/j.jallcom.2006.02.026.

[15] C. Bigi *et al.*, “Direct insight into the band structure of ${\mathrm{SrNbO}}_{3}$,” *Phys. Rev. Mater.*, vol. 4, no. 2, p. 025006, Feb. 2020, doi: 10.1103/PhysRevMaterials.4.025006.

[16] Y. Aiura, F. Iga, Y. Nishihara, H. Ohnuki, and H. Kato, “Effect of oxygen vacancies on electronic states of ${\mathrm{CaVO}}_{3\mathrm{\ensuremath{-}}\mathrm{\ensuremath{\delta}}}$ and ${\mathrm{SrVO}}_{3\mathrm{\ensuremath{-}}\mathrm{\ensuremath{\delta}}}$: A photoemission study,” *Phys. Rev. B*, vol. 47, no. 11, pp. 6732–6735, Mar. 1993, doi: 10.1103/PhysRevB.47.6732.

[17] T. Berry *et al.*, “The Role of Phonons and Oxygen Vacancies in Non-Cubic SrVO3,” *Inorg. Chem.*, vol. 61, no. 7, pp. 3007–3017, Feb. 2022, doi: 10.1021/acs.inorgchem.1c03201.

[18] T. Nakamura, G. Petzow, and L. J. Gauckler, “Stability of the perovskite phase LaBO3 (B = V, Cr, Mn, Fe, Co, Ni) in reducing atmosphere I. Experimental results,” *Materials Research Bulletin*, vol. 14, no. 5, pp. 649–659, May 1979, doi: 10.1016/0025-5408(79)90048-5.

[19] T. Miruszewski, B. Kamecki, M. Łapiński, and J. Karczewski, “Fabrication, structural and electrical properties of Sr(V,Nb)O3-δ perovskite materials,” *Materials Chemistry and Physics*, vol. 212, pp. 446–452, Jun. 2018, doi: 10.1016/j.matchemphys.2018.03.070.

[20] M. Mohammadi *et al.*, “Tailoring Optical Properties in Transparent Highly Conducting Perovskites by Cationic Substitution,” *Advanced Materials*, vol. 35, no. 7, p. 2206605, 2023, doi: 10.1002/adma.202206605.

[21] “Materials Science and Engineering: An Introduction, 10th Edition | Wiley,” Wiley.com. Accessed: Nov. 19, 2024. [Online]. Available: https://www.wiley.com/en-

us/Materials+Science+and+Engineering%3A+An+Introduction%2C+10th+Edition-p-9781119405498

[22] V. M. Goldschmidt, “Die Gesetze der Krystallochemie,” *Naturwissenschaften*, vol. 14, no. 21, pp. 477–485, May 1926, doi: 10.1007/BF01507527.

[23] M. Liberati, R. V. Chopdekar, V. Mehta, E. Arenholz, and Y. Suzuki, “Epitaxial growth and characterization of CaVO3 thin films,” *Journal of Magnetism and Magnetic Materials*, vol. 321, no. 18, pp. 2852–2854, Sep. 2009, doi: 10.1016/j.jmmm.2009.04.037.

[24] M. Takayanagi *et al.*, “Conductivity Modulation by CaVO3-based All-solid-state Redox Transistor with Ion Transport of Li+ or H+,” *Transactions of the Materials Research Society of Japan*, vol. 44, no. 2, pp. 57–60, 2019, doi: 10.14723/tmrsj.44.57.

[25] K. Nishimura, I. Yamada, K. Oka, Y. Shimakawa, and M. Azuma, “High-pressure synthesis of BaVO3: A new cubic perovskite,” *Journal of Physics and Chemistry of Solids*, vol. 75, no. 6, pp. 710–712, Jun. 2014, doi: 10.1016/j.jpcs.2014.02.001.

[26] J. Macías, J. R. Frade, and A. A. Yaremchenko, “SrTiO3-SrVO3 Ceramics for Solid Oxide Fuel Cell Anodes: A Route from Oxidized Precursors,” *Materials*, vol. 16, no. 24, Art. no. 24, Jan. 2023, doi: 10.3390/ma16247638.

[27] R. Merkle and J. Maier, “How Is Oxygen Incorporated into Oxides? A Comprehensive Kinetic Study of a Simple Solid-State Reaction with $SrTiO_3$ as a Model Material,” *Angew Chem Int Ed*, vol. 47, no. 21, pp. 3874–3894, May 2008, doi: 10.1002/anie.200700987.

Chapter 5 Conclusion and Future Work

The demand for low work function materials will only increase in the coming decades as thermionic emission technologies develop further, and the reach of these technologies expands. Aerospace ventures including deep space exploration and hypersonic vehicle development have already shown the increasing demand for these materials and the increasing need for high efficiency energy conversion will soon push thermionic emission to the forefront in energy engineering through emerging technologies like photon enhanced thermionic energy conversion [1], [2], [3], [4], [5]. Currently, thermionic emission technology relies on materials both volatile and expensive. BaO impregnated tungsten does not show low work function throughout the bulk and relies on a limited coating on the material surface which is prone to evaporation at high temperatures (>1000°C) [6]. Lanthanum hexaboride is already cost prohibitive for several industries interested in the use of thermionic emission technology and this will only worsen due to the small supply of lanthanum on the planet. It is imperative that more reliable, low-cost materials are developed in order to facilitate expansion and maturation of thermionic emission technology.

This work presents an investigation of two candidate materials, mayenite electride ($C12A7:e^-$) and strontium vanadate $SrVO_3$ which have demonstrated low work function and are made from abundant, low cost constituent powders. The materials were subjected to small amounts of cation substitution at both of their primary cation sites in order to elucidate the connection between the cation characteristics and the structure and properties of the materials. Particular attention was paid to the thermal stability and electrical conductivity of the materials

as these properties are critical to their successful adoption in the field of thermionic emission. Substitution of Mg at the Ca site and B at the Al site in C12A7:e^- was found to have profound effects on the thermal stability in delaying the onset of rapid oxidation by several hundreds of degrees. However, this effect was not dependent on the contraction of the crystal lattice or the "cage windows" which had been previously proposed. It was strongly influenced by the ability of solute cations to create a stronger bond to the encaged anions in the electride cages. The substitution of a larger cation for the calcium atom resulted in an increase in electrical conductivity. This was similar to results of a study of a strontium substitute for calcium, though there was no significant decrease of the thermal stability of the material which was expected to accompany the expanded cage [7]. Calcium substitution in strontium vanadate produced samples with extremely encouraging properties. The samples showed significant increase in resistance to oxidation, delaying rapid oxidation past 1050°C in the higher dosed samples. Simultaneously, the samples were observed to have huge increases in electrical conductivity (>3000S/cm) which supports the idea that the contribution to the conduction band from the Ca substitute was equal to or greater than the Sr solvent cation. These improvements make Ca-substituted $SrVO_3$ a robust candidate for thermionic emission applications. Both substitutions for the Sr site appeared to have substitutional solubility limits between 30-40% replacement. The perovskite structure is known to accommodate replacements as high as 50%. However, replacements at this level have only been observed up to 20% for the $SrVO_3$ system. Substitution at the V site showed little to no correlation with property changes and XRD data demonstrated the unreliability of these substitutions. Ti substitution on the vanadium site led to inhomogeneous samples comprised of pure strontium vanadate, Ti-substituted strontium vanadate, and pure strontium titanate. Mn

substitution was not achieved above a level of 0.2 and was shown to produce a variety of secondary phases above this level.

Dual substitution had varying degrees of effectiveness between the different material systems and the different combinations of substitutions. For three of the four equal dosed, dual substitution samples, (0.1Mg+0.1Mn)-C12A7e$^-$, (0.1Ba+0.1B)-C12A7e$^-$, and (0.1Ca+0.1Ti)-SVOD, it was noted that dominant effects came from the solute atom with the largest ionic radius size change from the solvent atom. However, in the unequally dosed samples - (0.2Mg+0.1Mn)-C12A7e$^-$, (0.1Ba+0.2B)-C12A7e$^-$, and (0.2Ca+0.1Ti)-SVOD), the dominant effects switched to the solute atom with higher dose regardless of cation size. Both equal dosed samples in the mayenite system demonstrated combined effects to key properties from the individual substitutions, though these property changes were not as large in magnitude as they were for the individual substitutions. The dual substitutions in the strontium vanadate were not successful due to restrictions in incorporating the substitutional solute atoms into the V site. The (Ba+Mn) dual substitution led to phase breakdown due to the large differences in cation size. The (Ca+Ti) dual substitution led to improvement in both thermal stability and electrical conductivity. But the extent of the improvement was miniscule compared to those observed in the individual Ca substituted $SrVO_3$ samples.

5.1 Specific Cation Substitution Recommendations

The following goes over several specific cation substitution recommendations. These suggestions specifically aim to address the remaining gaps after the completion of the work covered in the dissertation. Some of these substitutions have already been experimentally investigated in other studies, but the current literature does not provide an insight into the effects

of the substitutes on the thermal stability of the materials, which is critical for the application in thermionic emission.

5.1.1 C12A7 Ca-Site

Substitutions for calcium have mostly been restricted to the alkali earth metals in both the literature and this work. There has been some work in substitution of copper which has demonstrated increased conductivity at low substitution levels, but beyond that no transition metal transitions have been applied to the Ca site [8]. It is of particular interest to gain more insight into the contribution of Ca substitutions to the cage conduction band as this is one of the governing forces behind the low work function of mayenite electride. For that reason, cobalt (Co) would be excellent future candidate for study. The change in ionic radius for Co would be comparable to that for the Mg substitute studied here, and the greater electronegativity of Co compared to Mg could further encourage binding of the encaged anions to improve thermal stability. Furthermore, the distinction between a Co substitute and the Cu substitute previously studied would help to better understand the contribution of s-band vs d-band electrons to C12A7:e- electronic configuration. Additionally, this substitution has been applied to the Al site so this would also serve as an opportunity to compare different effects of substituting between the two sites.

5.1.2 C12A7 Al-Site

Previous works by Khan and Bertoni have demonstrated the capability of C12A7:e- to accommodate cations with increased oxidation number by housing extra anions [9], [10]. In both of these works the authors examined a silicon (Si) substitute which led to enhanced electrical conductivity. However, neither author presented structural analysis data nor thermal analysis

data and these gaps remain unfilled. The current work showed that a B substitute at the Al site resulted in an increase in thermal stability while substantially decreasing the electrical conductivity. A substitution of Si would represent a smaller change to the ionic radius of the Al site (similar in magnitude with the Mg substitute for Ca shown in this work). Theoretically this substitution could lead to increased thermal stability (to a lesser extent than that achieved with the B substitute) while also leading to increased electrical conductivity. A more comprehensive study of Si would confirm or disconfirm this hypothesis and would prove useful in further understanding the effects of increased encaged anions in the mayenite electride structure as it would be possible to observe interplay between solute cation size and increased electron anion concentration.

5.1.3 $SrVO_3$ A-Site

Most work looking at substitutions in the strontium vanadate system are focused on the vanadium site (B-site). The most recent study examining A-site substitution was focused on substituting higher charged cations as a means to increase the influence of d-band electrons from the B-site[11]. As discussed previously, the Ca substitute was the most successful substitution for the strontium vanadate system, but how might the presence of a d-band in the A-site effect the electrical properties of the compound? Silver (Ag) would represent a near identical change as far as cation size compared to the Ca substitute, but an additional understanding of the electronic configuration and its contribution to the properties could be extracted from this study.

5.1.4 $SrVO_3$ B-Site

As previously discussed, there is widespread thought that the d-band electrons of the V cation are what cause its excellent electrical properties. This correlation can be further explored

in studying a replacement which offers one additional d-band electron compared to vanadium. Chromium (Cr) substitution represents a similar substitution to the Mn substitution presented in this work. However, with a smaller change to the ionic radius which should keep the tolerance factor of the system closer to one, the integration of the substitute should be more successful. Moreover, theoretical calculations by Ma et al. predict that increasing the number of d-band electrons above three would lead to a significant decrease in electrical properties [12]. The results from the Mn study presented here cannot confirm or disconfirm this prediction so further study is needed to possibly eliminate the heavier transition metals from substitute consideration.

5.2 Material Processing

Both of the materials studied in this work have remaining limitations when it comes to processing and machinability. While the cation substituted mayenite electride and strontium vanadate presented here exhibit promising electronic and thermal properties, their application in practical devices necessitates improved mechanical robustness. Additionally, achieving good ohmic contact on machined surfaces of mayenite electride remains a challenge as evidenced by the relatively low electrical conductivity numbers presented here. One potential avenue for addressing these issues is the fabrication of composite materials that integrate these oxide ceramics with more conductive and mechanically stable phases. By incorporating secondary phases such as refractory metals, transition metal carbides, or nitrides, it may be possible to improve electrical conductivity at the contact interface while simultaneously increasing mechanical integrity.

For mayenite electride, previous research has demonstrated that its low work function and high electron mobility can be preserved when integrated with metallic (Ti) or ceramic (TiB_2)

reinforcements. To this author's knowledge, there is no work examining the effects of compositing on strontium vanadate and its low work function. Additional studies are needed to optimize processing techniques that ensure uniform dispersion of the secondary phase without compromising beneficial effects achieved with cation substitution. Spark plasma sintering (SPS) provides a promising route for achieving this goal, as its rapid heating rates and applied pressure can facilitate densification while minimizing grain growth. Investigating different composite formulations, such as TiC- or Mo-based composites, could yield a material system that retains the beneficial electronic characteristics of the materials while exhibiting greater resistance to thermal and mechanical degradation.

The long processing time of strontium vanadate remains a critical bottleneck in its practical implementation. Traditional synthesis methods require extended reduction treatments in high-temperature hydrogen environments, significantly limiting scalability and increasing processing costs. An alternative approach that warrants exploration is reaction sintering within an SPS system, where the initial oxide precursors—such as $SrCO_3$ and V_2O_5 —can be directly converted to $SrVO_3$. In separate work from this dissertation, it has been demonstrated that highly conductive, cubic strontium vanadate can be formed from precursors in SPS without external reduction agents. This approach would not only bypass the lengthy pre-sintering reduction step but also enable finer control over the resulting microstructure, which could be critical for enhancing both electronic and thermal stability. Beyond the direct synthesis of $SrVO_3$, reaction sintering within SPS may also facilitate doping strategies that were previously constrained by the need for multiple high-temperature processing steps. Dual-site substitution, in particular, could be directly incorporated into the sintering process, allowing for controlled defect engineering and improved oxidation resistance. The rapid heating and cooling cycles in SPS may also suppress

secondary phase formation, ensuring a more homogeneous solid solution while avoiding decomposition pathways commonly observed in prolonged furnace treatments.

Future work should prioritize systematic investigations into these alternative processing methods, focusing on optimizing sintering conditions, secondary phase selection for composites, and in situ reduction strategies for $SrVO_3$. By refining these approaches, it will be possible to develop thermionic emission materials that not only exhibit superior electronic properties but also possess the necessary mechanical and thermal stability for long-term operation in demanding environments.

5.3 Mayenite Modeling

Future work should focus on refining the Rietveld modeling of mayenite and mayenite electride to enhance the accuracy of structural characterization. One major limitation in current models is the incomplete understanding of the occluded oxygen anions within the framework cages. Neutron powder diffraction offers a promising pathway for overcoming this issue, as neutrons are highly sensitive to light elements like oxygen. By incorporating neutron diffraction data, it will be possible to develop a more precise model of oxygen site occupancy and distribution, leading to a better understanding of how these anions contribute to the altered cage structure of cation substituted mayenite.

Additionally, improvements in Rietveld refinement should include a more detailed treatment of displaced atomic sites, particularly shifted cation positions such as Ca3 and Al3, which may shift in response to cation substitutions. The structural models presented here and in other works simplify these displacements, limiting our ability to accurately capture local

distortions and their impact on thermal stability and conductivity. Expanding the model to include these additional atomic positions will provide deeper insights into the lattice dynamics and substitutional effects, ultimately allowing for more targeted material optimizations.

Another crucial step in refining the structural analysis of mayenite and its electride form is the collection of higher-resolution synchrotron x-ray diffraction data. While conventional laboratory-based XRD studies provide valuable insights, synchrotron radiation offers significantly enhanced resolution, allowing for the modeling of atomic thermal vibrations using anisotropic displacement parameters. This level of detail is particularly important for understanding the dynamic behavior of cage electrons and their interaction with the lattice. By integrating high-resolution synchrotron data with neutron diffraction and expanded atomic displacement models, future studies can achieve a more comprehensive characterization of mayenite electride, paving the way for more effective material design strategies.

5.4 New Technologies

In a big picture perspective, the findings of my dissertation work also led me to think about what other technologies can be enabled or enhanced based on the development of $SrVO_3$ and improvement of the properties of the mayenite electride materials. The first example is waste heat recovery through thermionic energy converters (TECs). TECs are devices that convert high-temperature heat into electricity through electron emission across a vacuum gap. TECs offer the possibility of high efficiency due to minimization of mechanical losses which makes them promising for applications in extreme environments like space and concentrated solar power systems. Despite their potential, most TEC prototypes have struggled to reach efficiency targets due to low power densities, space charge effects, and challenges in maintaining micron-scale

gaps between cathode and anode. However, a novel TEC configuration combining thermionic and photovoltaic effects has begun to gain traction in the last decade. Photon-enhanced thermionic emission (PETE) has been presented as a possible improvement upon traditional solar cells helping to overcome heating effects experienced by these cells by leveraging both photon energy and heat to stimulate electron emission. In traditional photovoltaic cells, excess photon energy (above the bandgap) is lost as heat, which can reduce cell efficiency and longevity. PETE devices, however, use this heat to enhance thermionic emission, creating an additional pathway for energy conversion. This combined effect increases efficiency by converting the thermalized photon energy into electricity rather than letting it degrade the cell's performance. The bandgap structure for a basic PETE device is shown in Figure 5.1 [13].

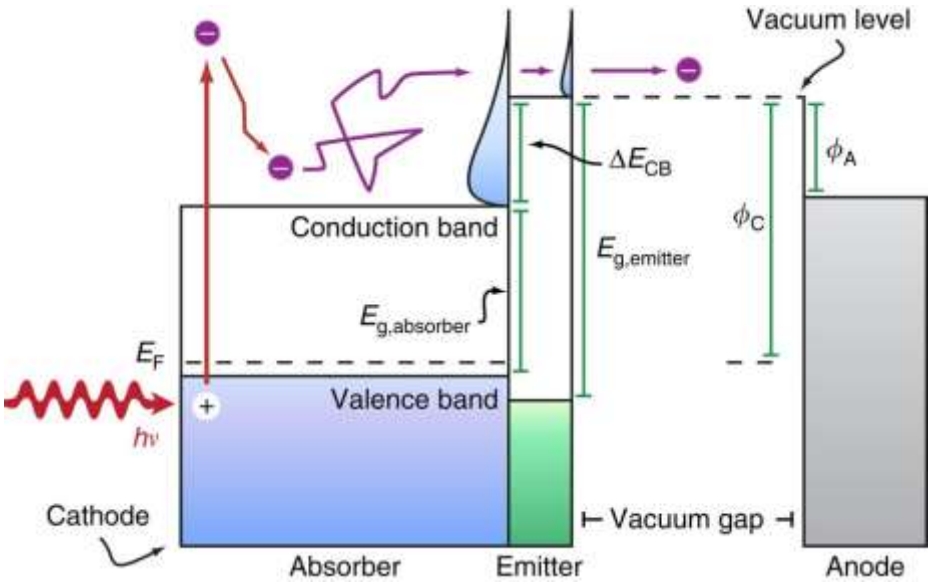

Figure 5.1 Band Structure of proposed PETE Device

A more recent proposal by scientists at NASA's Langley Research Center attempts to leverage thermionic emission more directly for power generation. The proposed Nuclear Thermionic Avalanche Cell (NTAC) would utilize multiple layers of emitter and collector

materials in order to generate power from nuclear gamma ray photon energy as shown in the schematic in Figure 5.2 [14].

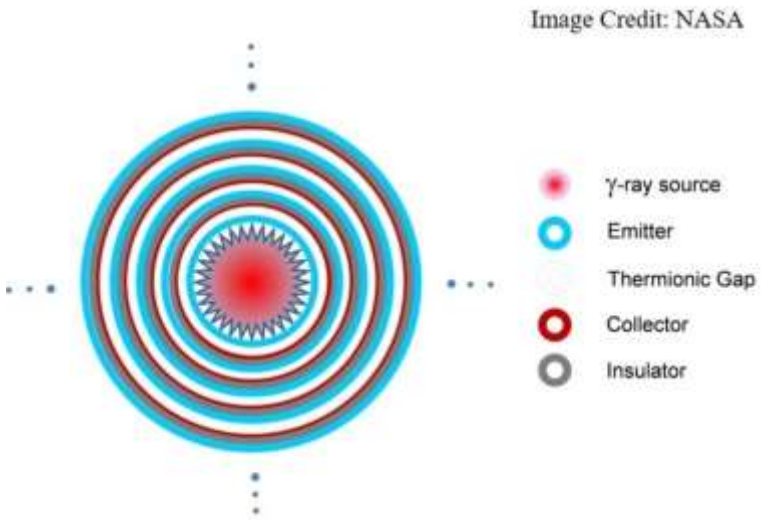

Figure 5.2 Basic schematic of Nuclear Thermionic Avalanche Cell

Realization of the NTAC device would yield large improvements (two to three fold increase to efficiency) compared to thermoelectric devices which utilize radioisotope decay. Additionally, as this device relies on radioactive decay, it could be used to generate power for decades. Technologies such as these can only be realized through the improvement of thermionic emission materials. This work demonstrates several avenues for this improvement while also highlighting other avenues not yet fully explored in the field of study.

References

[1] M. Coutinho *et al.*, "A review on the recent developments in thermal management systems for hybrid-electric aircraft," *Applied Thermal Engineering*, vol. 227, p. 120427, Jun. 2023, doi: 10.1016/j.applthermaleng.2023.120427.

[2] E. Elnagar, S. Pezzutto, B. Duplessis, T. Fontenaille, and V. Lemort, "A comprehensive scouting of space cooling technologies in Europe: Key characteristics and development trends," *Renewable and Sustainable Energy Reviews*, vol. 186, p. 113636, Oct. 2023, doi: 10.1016/j.rser.2023.113636.

[3] Y. Qi, X. Ma, P. Jiang, and Y. Zhu, "Review on heat-to-power conversion technologies for hypersonic vehicles," *Chinese Journal of Aeronautics*, vol. 37, no. 5, pp. 148–179, May 2024, doi: 10.1016/j.cja.2023.11.002.

[4] M. F. Campbell, T. J. Celenza, F. Schmitt, J. W. Schwede, and I. Bargatin, "Progress Toward High Power Output in Thermionic Energy Converters," *Advanced Science*, vol. 8, no. 9, p. 2003812, 2021, doi: 10.1002/advs.202003812.

[5] K. A. Abdul Khalid, T. J. Leong, and K. Mohamed, "Review on Thermionic Energy Converters," *IEEE Transactions on Electron Devices*, vol. 63, no. 6, pp. 2231–2241, Jun. 2016, doi: 10.1109/TED.2016.2556751.

[6] D. R. Lev, I. G. Mikellides, D. Pedrini, D. M. Goebel, B. A. Jorns, and M. S. McDonald, "Recent progress in research and development of hollow cathodes for electric propulsion," *Rev. Mod. Plasma Phys.*, vol. 3, no. 1, p. 6, Dec. 2019, doi: 10.1007/s41614-019-0026-0.

[7] J. Zhao, X. Zhang, H. Liu, Y. Xiao, H. Jiang, and J. Zhang, "Synthesis and Characterization of (Ca1−xSrx)12Al14O33 Electrides," *Crystal Research and Technology*, vol. 53, no. 1, p. 1700201, 2018, doi: 10.1002/crat.201700201.

[8] F. Liu *et al.*, “High electrical transport performance of C12A7: e– ceramics electrides on Cu-doping,” *Journal of the American Ceramic Society*, vol. 105, no. 6, pp. 4135–4142, 2022, doi: 10.1111/jace.18379.

[9] K. Khan *et al.*, “Facile synthesis of a cationic-doped [Ca24Al28O64]4+(4e−) composite via a rapid citrate sol–gel method,” *Dalton Trans.*, vol. 47, no. 11, pp. 3819–3830, Mar. 2018, doi: 10.1039/C7DT04543C.

[10] M. I. Bertoni, T. O. Mason, J. E. Medvedeva, Y. Wang, A. J. Freeman, and K. R. Poeppelmeier, “Enhanced electronic conductivity in Si-substituted calcium aluminate,” *Journal of Applied Physics*, vol. 102, no. 11, p. 113704, Dec. 2007, doi: 10.1063/1.2817605.

[11] J. Macías, “Enhanced stability of perovskite-like SrVO3-based anode materials by donor-type substitutions,” *Journal of Materials Chemistry A*, p. 9, 2016.

[12] T. Ma, R. Jacobs, J. Booske, and D. Morgan, “Discovery and engineering of low work function perovskite materials,” Journal of Materials Chemistry C, vol. 9, no. 37, pp. 12778–12790, 2021, doi: 10.1039/D1TC01286J.

[13] J. W. Schwede *et al.*, “Photon-enhanced thermionic emission from heterostructures with low interface recombination,” *Nat Commun*, vol. 4, no. 1, p. 1576, Mar. 2013, doi: 10.1038/ncomms2577.

[14] “Multi-Layer Nuclear Thermionic Avalanche Cell | T2 Portal.” Available: https://technology.nasa.gov/patent/LAR-TOPS-335